The Journal of Neuroscience

October 3, 2007 • Volume 27 Number 40 • www.jneurosci.org

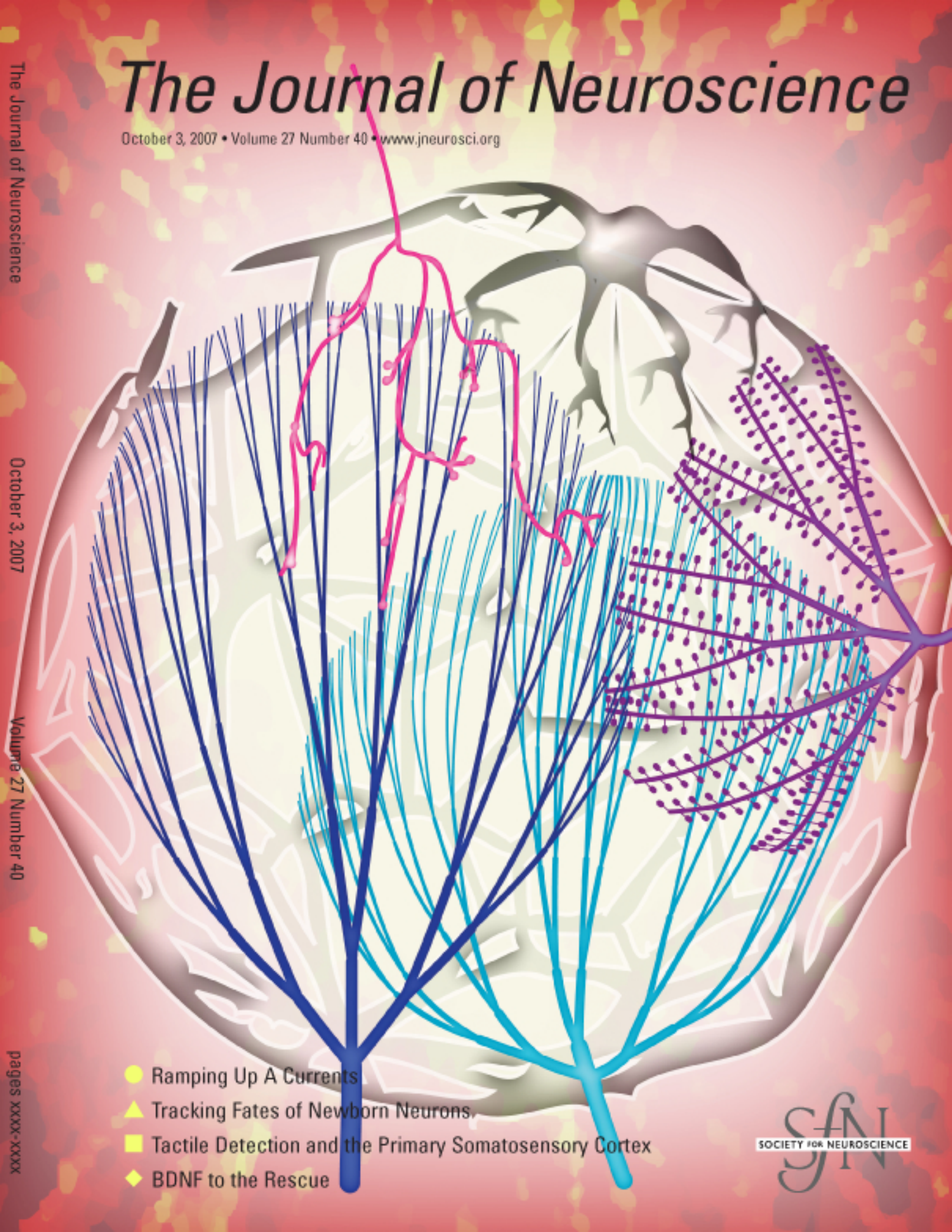

- Ramping Up A Currents
- Tracking Fates of Newborn Neurons.
- Tactile Detection and the Primary Somatosensory Cortex
- BDNF to the Rescue

SOCIETY FOR NEUROSCIENCE

The Journal of Neuroscience

October 3, 2007

Volume 27 Number 40

pages xxxx-xxxx

Behavioral/Systems/Cognitive

Neural Correlates of Tactile Detection: A Combined Magnetoencephalography and Biophysically Based Computational Modeling Study

Stephanie R. Jones,[1] Dominique L. Pritchett,[2] Steven M. Stufflebeam,[1] Matti Hämäläinen,[1] and Christopher I. Moore[1,2]

[1]Athinoula A. Martinos Center for Biomedical Imaging, Massachusetts General Hospital, Charlestown, Massachusetts 02129, and [2]McGovern Institute for Brain Research, Massachusetts Institute of Technology, Cambridge, Massachusetts 02139

Previous reports conflict as to the role of primary somatosensory neocortex (SI) in tactile detection. We addressed this question in normal human subjects using whole-head magnetoencephalography (MEG) recording. We found that the evoked signal (0–175 ms) showed a prominent equivalent current dipole that localized to the anterior bank of the postcentral gyrus, area 3b of SI. The magnitude and timing of peaks in the SI waveform were stimulus amplitude dependent and predicted perception beginning at ~70 ms after stimulus. To make a direct and principled connection between the SI waveform and underlying neural dynamics, we developed a biophysically realistic computational SI model that contained excitatory and inhibitory neurons in supragranular and infragranular layers. The SI evoked response was successfully reproduced from the intracellular currents in pyramidal neurons driven by a sequence of lamina-specific excitatory input, consisting of output from the granular layer (~25 ms), exogenous input to the supragranular layers (~70 ms), and a second wave of granular output (~135 ms). The model also predicted that SI correlates of perception reflect stronger and shorter-latency supragranular and late granular drive during perceived trials. These findings strongly support the view that signatures of tactile detection are present in human SI and are mediated by local neural dynamics induced by lamina-specific synaptic drive. Furthermore, our model provides a biophysically realistic solution to the MEG signal and can predict the electrophysiological correlates of human perception.

Key words: **computational model; magnetoencephalography; dendritic processes; conscious perception; network dynamics; somatosensory cortex**

Introduction

The role of primary sensory cortex in conscious perception is debated (Danckert and Goodale, 2000; Ress et al., 2000; Crick and Koch, 2003; Ergenoglu et al., 2004; Stoerig, 2006), and previous reports conflict as to the presence of neural correlates of tactile detection in primate primary somatosensory cortex (SI). In recent single-unit recording studies in monkeys, de Lafuente and Romo (2005, 2006) found that action potential firing rate in areas 3b and 1 did not predict "hit" and "miss" trials at threshold. Furthermore, monkeys can relearn a tactile detection task after comprehensive SI lesions (LaMotte and Mountcastle, 1975, 1979). In contrast, when somatosensory evoked potentials are recorded from the postcentral gyrus (PoCG) in macaques, the N1 and P2 peak magnitudes, at 50–65 and 105–130 ms, respectively, predict detection (Kulics, 1982; Kulics and Cauller, 1986; Cauller and Kulics, 1991). In human studies, response magnitude and coherence across electrodes above rolandic cortex have been reported to predict detection (Meador et al., 2002; Palva et al., 2005). Tactile spatial attention in humans also recruits what appear to be SI-specific effects (Drevets et al., 1995; Bauer et al., 2006). Furthermore, studies of the impact of ongoing activity at the time of stimulus presentation in humans show that functional magnetic resonance imaging (fMRI) blood–oxygen level-dependent signals localized to the anterior PoCG are greater on hit than miss trials (Moore et al., 2007), and intermediate amplitudes of prestimulus power (10, 20, and 40 Hz) in magnetoencephalography (MEG) signals measured above the sensorimotor cortex predict detection (Linkenkaer-Hansen et al., 2004).

These discrepancies may be attributable to differences in recording approach. Single-unit recordings are advantageous for reporting individual neuron activity but are difficult to obtain in humans, limiting observations to highly trained monkeys. Furthermore, action potential recordings do not provide information about subthreshold cellular and field potential activity or the activity of smaller neurons that may be coincident with sensory information processing. Surface recordings using MEG or EEG provide access to neurophysiological signals in human subjects,

Received Feb. 2, 2007; revised Aug. 16, 2007; accepted Aug. 19, 2007.

This work was supported by National Institutes of Health Grants P41RR14075, K25MH072941, 1R01-NS045130-01, and T32 GM007484; National Science Foundation Grant 0316933; the Athinoula A. Martinos Center for Biomedical Imaging; the McGovern Institute for Brain Research; and the MIND (Mental Illness and Neurodiagnostic Discovery) Institute. We thank Michael Sikora and Michael Hines for excellent technical support in implementation of network structure in NEURON software code. We also thank Charles Schroeder and Michael Lipton for valuable discussions of preliminary data from laminar recordings in awake monkeys, Seppo Ahlfors for insightful comments on MEG equivalent current dipole sources, and Dahlia Sharon and Talia Konkle for thorough remarks on this manuscript.

Correspondence should be addressed to Stephanie R. Jones, Massachusetts General Hospital, Athinoula A. Martinos Center for Biomedical Imaging, 149 13th Street, Suite 2301, Charlestown, MA 02129. E-mail: srjones@nmr.mgh.harvard.edu.

DOI:10.1523/JNEUROSCI.0482-07.2007

 0270-6474/07/2710751-14$15.00/0

but the cortical population dynamics inducing the recorded signal have not been conclusively defined. Furthermore, these studies often do not localize activity to specific cortical areas.

We examined cortical correlates of somatosensory perception in human SI by combining MEG and computational neural modeling. By calculating the equivalent current dipole (ECD) at SI, we were able to localize an early and robust source to the anterior PoCG, putative area 3b. The timing and magnitude of this SI waveform predicted perception of the tactile stimulus beginning at 70 ms after stimulus.

To provide a framework for understanding the MEG signal and SI neural correlates of perception, we developed a realistic laminar network model. Longitudinal intracellular currents were sampled from detailed compartmentalized pyramidal neurons (PNs) in the supragranular and infragranular layers to calculate the net ECD produced by the population. We found that the timing, magnitude, and direction of the peaks in the observed SI evoked response could be accurately reproduced in the model when a sequence of lamina-specific exogenous drive to the SI network was simulated. The model also predicted that the observed differences in SI between detected and nondetected stimuli resulted from subtle changes in the timing and amplitude of an ~70 ms input to the supragranular layers and a later ~135 ms output from the granular layers. These findings provide evidence that SI activity predicts tactile detection and that these predictive signals in SI depend on the pattern of exogenous, lamina-specific input.

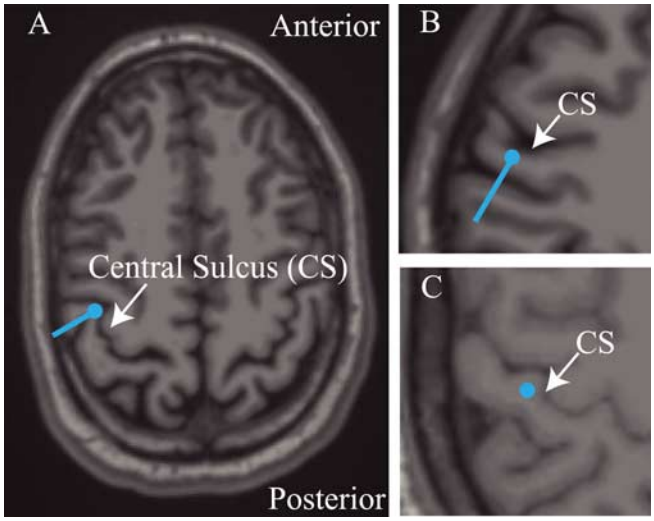

Figure 1. Localization of SI activity. Estimated SI ECD localizations (blue dots) and orientations (blue lines) overlaid on the subjects' structural MRI brain images. The response evoked by stimulus to the third digit of the right hand was localized in the anterior bank of the contralateral postcentral gyrus, the position of area 3b. ***A***, ***B***, Example localizations and orientations from two subjects using the inverse solution technique described in Materials and Methods. ***C***, Example localization for one of two subjects for which the SI ECD was placed (see Materials and Methods).

Materials and Methods

MEG experiment

Subjects. Seven neurologically healthy, right-handed, 18- to 45-year-old adults were studied.

Stimulus paradigm. Brief taps were delivered to the subject's right hand in the form of a single cycle of 100 Hz sine wave (10 ms duration) via a custom piezoelectric device. Subjects rested their hand on a Delrin frame that held a piezoelectric parallel to the finger (Noliac ceramic multilayer bender plate 32 × 7.8 × 1.88 mm). A deflection stroke drove a Delrin contactor into the fingertip (7 mm diameter contractor presented within a 1 cm circular rigid surround).

Individual subjects' thresholds were obtained before imaging using a parameter estimation by sequential testing (PEST) convergence procedure (Dai, 1995; Leek, 2001). This algorithm obtained the threshold by first using a strong stimulus (100% amplitude, 350 μm deflection), followed by a weak stimulus (50% amplitude) and a blank stimulus. If the subject reported detection of the strong and the weak stimulus, then the next set of stimuli was given the 50% value set for the strong stimulus and a new value at one-half the distance between the weak and blank stimulus for the middle stimulus. If the subject did not detect the middle stimulus, then the maximum stimulus remained the same, the middle stimulus became the new minimum stimulus, and the new value for the middle stimulus was obtained by averaging the maximum and new minimum. This procedure was repeated until the change in the amplitude of movement for the piezoelectric between trials was <5 μm. Before MEG recording, the stimulus strength was set to the threshold value obtained during the PEST.

During MEG imaging, for 70% of presented trials, stimulus strength was maintained at a perceptual threshold (T) level (50% detection) using a dynamic algorithm. If two correct responses were made, the threshold-level voltage sent to the piezoelectric was decreased by 0.005 V (a change of ~4.5 μm in piezoelectric movement), and the correct response counts were reset to zero. In contrast, if three incorrect responses were made, the voltage was increased by 0.005 V. The deflection amplitudes for all threshold stimuli across all subjects were between 200 and 230 μm. Suprathreshold (ST) stimuli (10% of all trials; 350 μm deflection; 100% detection) and null trials (20%) were randomly interleaved with the threshold stimuli and were excluded from the correct response counts used in the dynamic algorithm. Trial duration was 3 s. Each subject underwent eight runs with 120 trials. Trial onset was indicated by a 60 dB, 2 kHz auditory cue delivered to both ears for a duration of 2 s. During the auditory cue, the 10 ms finger tap stimulus was delivered between 500 and 1500 ms, in 100 ms intervals, from trial onset. The number of trials of a given latency to tap was randomly distributed during each run. After the cessation of the auditory cue, subjects reported detection or nondetection of the stimulus with button presses using the second and third digits of the left hand, respectively. The auditory cue ended ≥500 ms after tactile stimulus and 1000 ms before the next trial began.

MEG data acquisition. Using a 306-channel magnetoencephalograph (VectorView; Elekta NeuroMag, Helsinki, Finland), neuromagnetic responses were recorded with 306 sensors arranged in triplets of two planar gradiometers and a magnetometer at 102 sites. In addition to MEG, the vertical and horizontal electrooculogram (EOG) was recorded with electrodes placed close to the left eye. Four head-position indicator coils were placed on the subject's head to coregister the subject's anatomical MRI and the MEG sensors. The data were sampled at 600 Hz with the bandpass set to 0.01–200 Hz. The responses were averaged on-line for quality control. In the off-line analysis, the data were reaveraged using a bandpass of 0.03–200 Hz. Epochs with EOG peak-to-peak amplitude exceeding 150 μV were excluded from the analysis.

MEG source analysis. The aim of our source analysis was to locate a primary current-dipole source at the contralateral SI area and to find the time course of this source, taking into account the presence of other active areas. Previous studies have shown that somatosensory evoked fields (SEFs) can be well approximated with a small number (typically three, for median nerve stimulation) of serially and simultaneously active ECD sources (Brenner et al., 1978; Hari and Forss, 1999). For tactile stimulation, a primary current source is typically initially observed in SI with later activation having additional contributions from a second source, likely representing SII (Forss et al., 1994b; Hari and Forss, 1999; Hoechstetter et al., 2000, 2001; Kakigi et al., 2000). To isolate the contribution from SI to the SEF, we used the following approach.

Initial inspection of the early field patterns of the suprathreshold trials demonstrated activity consistent with SI activation contralateral to the stimulus, and later field patterns indicated a source in the contralateral parietal operculum, presumably SII. The activation of this second source was weak and inconsistent across subjects. No consistent activity over the ipsilateral SII or in other brain areas was observed. Therefore, we mod-

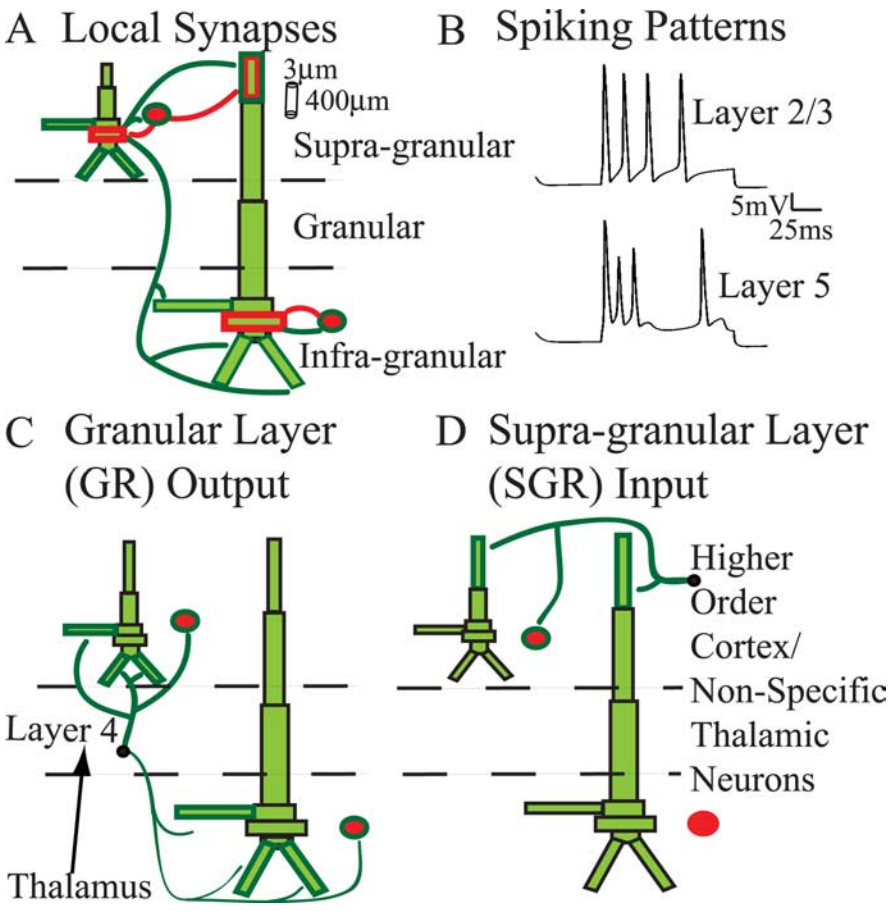

Figure 2. Model SI network architecture. Ten PNs and 3 INs were included per layer. Excitatory (dark green) and inhibitory (red) synaptic connections were set as depicted. Bold outlined dendrites were contacted. ***A***, Local synapses. Within-layer PN-to-PN synapses (not shown) were also present on dark green outlined dendrites. Each set of synaptic weights had a Gaussian spatial profile (Table 2). ***B***, Spiking patterns evoked by somatic injected current (1 nA, 100 ms; no synaptic input). ***C***, Connection pattern of output from the GR. The black arrow is only schematic, because lemniscal thalamic input was not explicitly modeled. ***D***, Connection pattern of exogenous input to the SGR, presumably from a higher-order cortical and/or nonspecific thalamic neurons. The output from GR and input to SGR were modeled as spike train generators with a predetermined temporal profile and synaptic strength (Table 3).

Table 1. Dimensions of pyramidal neuron compartments in micrometers

	Layer 5		Layer 2/3	
	Length	Diameter	Length	Diameter
Soma	39	28.9	22.1	23.4
Apical trunk	109	10.2	59.5	4.25
Oblique	255	5.1	340	3.91
Apical no. 1	680	7.48	306	4.08
Apical no. 2	680	4.93	—	—
Apical tuft	425	3.4	238	3.4
Basal trunk	85	6.8	85	4.25
Basals (2)	255	8.5	255	2.72

no., Number.

eled the data with two dipoles and optimized this fit with help of the signal-space projection (SSP) method (Tesche et al., 1995; Uusitalo and Ilmoniemi, 1997) as follows. First, using a least-squares fit with the dipole forward solution calculated using the spherically symmetric conductor model (Sarvas, 1987; Hämäläinen and Sarvas, 1989), we found an initial ECD at the peak activity in the suprathreshold stimulus signals from one data run (average of 12 trials; mean, 68 ms; SD, 8 ms). With help of the anatomical MRI, coregistered with the MEG, we were able to confirm that this source localized to SI in four of seven subjects (Fig. 1*A*,*B*). In the second step, the contribution of the SI ECD was removed from the data using the SSP method, and a second ECD was fitted to the residual data (Tesche et al., 1995; Uusitalo and Ilmoniemi, 1997; Nishitani and Hari, 2000). Importantly, the same projection operator that was applied to the data to remove the effect of the SI source was also taken into account in the forward solution when the second dipole was fitted (Uusitalo and Ilmoniemi, 1997). The goodness of fit of the two-dipole model was larger than 70% in all fit data during peak responses. In the final step, the effect of the second ECD, which was not the focus of the present study, was removed from the data using SSP, the SI ECD was refitted to the residual, and its waveform was recalculated. The ECD localizations fitted to the suprathreshold data were used to model all responses. To account for adaptation and learning effects with training, only the last 100 trials for a given response were considered for analysis.

For two of seven subjects, large baseline rhythmic activity interfered with the localization of peak responses. For these subjects, the initial source was placed in the anterior bank of the postcentral gyrus in an area consistent with the localization of the finger representation of area 3b (Fig. 1*C*) (Penfield and Rasmusson, 1950; Uematsu et al., 1992; White et al., 1997; Yousry et al., 1997; Sastre-Janer et al., 1998; Moore et al., 2000), and the second dipole source was placed in the parietal operculum. For one subject, we were unable to obtain anatomical MRI data. Dipole localization was determined by field contours on the spherical head model and showed an initial source above the predicted position of contralateral SI and a second source over the predicted position of the parietal operculum. The source localizations used for each of the three subjects discussed above produced evoked dipole waveforms consistent with those of the other subjects (see Results).

Computational neural model

Several lines of evidence predict that postsynaptic intracellular longitudinal currents within the long apical dendrites of synchronized cortical pyramidal cells are the main contributors to MEG primary current sources (Hämäläinen et al., 1993; Okada et al., 1997; Murakami et al., 2002, 2003; Ikeda et al., 2005; Murakami and Okada, 2006). As such, we incorporated realistic pyramidal neuron morphology and physiology into our SI model and calculated the net ECD from the longitudinal intracellular currents within these pyramidal neurons. The complete SI network contained pyramidal neurons and inhibitory interneurons in the supragranular and infragranular layers, as depicted in Figure 2*A*. This laminar construction enabled us to study the influence of a specific physiologically based sequence of exogenous synaptic inputs, defined by the laminar location of their postsynaptic effects (Figs. 2*C*,*D*), on the ECD produced by the SI population.

The individual neurons and network architecture were implemented as follows.

Pyramidal neuron morphology and physiology. The model contained PNs with somata in layers 2/3 (L2/3) and layer 5 (L5) (Fig. 2). Simulations of L2/3 and L5 PN morphology and physiology were adapted from Bush and Sejnowski (1993), whose code is available in NEURON software format at http://senselab.med.yale.edu/senselab/modeldb/. Individual L2/3 and L5 PNs were constructed with a small number of compartments (eight and nine, respectively) and maintain the morphology of the real PNs on which they are based [digitized HRP-filled L2 and L5 PNs from the cat visual cortex (Koch et al., 1990)]. The accurate morphological construction of the dendrites allowed for a spatially accurate network

model. The compartmentalization of each of the PNs is shown in Fig. 2*A* and described in Table 1. In our model, a scaling factor of 1.3 was applied to the length and diameters of the dendritic compartments used by Bush and Sejnowski (1993) to account for increases in dendritic length and volume in human somatosensory neurons, as predicted by larger cortical thickness (Geyer et al., 1997; Fischl and Dale, 2000) and an increase in the number of dendritic spines and arborization (Elston et al., 2001). The membrane resistance was increased and membrane capacitance was decreased by the same scaling factor ($R_m = 23{,}474\ \Omega \cdot cm^2$ for L5 and L2/3; $C_m = 0.85$ and $C_m = 0.6195\ \mu F/cm^2$ for L5 and L2/3, respectively) to maintain the input resistances in the cells of 45 MΩ for the L5 and 110 MΩ for L2/3 (Douglas et al., 1991). The axial resistance for each cell was $R_a = 200\ \Omega \cdot cm$ (Segev et al., 1992).

Active currents in L2/3 PNs included a fast sodium current (I_{Na}), a delayed rectifier potassium (I_{Kdr}) current, an adapting potassium current (I_M), and a leak current (I_L). The L5 PNs contained the same currents with the addition of a calcium current (I_{Ca}) and a potassium-activated calcium current (I_{KCa}). The kinetic equations and NEURON code used for each of these currents were as used by Mainen and Sejnowski (1996) and downloaded from http://senselab.med.yale.edu/senselab/modeldb/. The maximal conductances of each current were constant throughout the soma and dendrite (Stuart and Sakmann, 1994; Bekkers, 2000; Korngreen and Sakmann, 2000; Migliore and Shepherd, 2002) and were chosen to produce adapting spikes in the L2/3 PNs and bursting in the L5 PNs to current injected in the soma (1 nA for 100 ms) (Fig. 2*B*) representative of neurons classified as regular spiking and intrinsically bursting, respectively (Silva et al., 1991; Moore and Nelson, 1998; Zhu and Connors, 1999). The maximal conductance parameters (in S/cm^2) were as follows: L2/3 parameters, $g_{Na} = 0.15$; $g_K = 0.01$; $g_M = 0.00025$; $g_L = 0.0000426$; L5 parameters, $g_{Na} = 0.14$; $g_K = 0.01$; $g_M = 0.0002$; $g_{Ca} = 0.00006$; calcium decay time constant = 20 ms; $g_{KCa} = 0.2 \times 10^{-9}$. The ionic reversal potentials (in mV) were as follows: $E_{Na} = -50$; $E_K = E_M = 77$; $E_L = -65$.

Inhibitory interneurons. Inhibitory interneurons (INs) were included to simulate their postsynaptic effect on the network. They were modeled with single compartments and contained only fast sodium (I_{Na}) and potassium currents (I_{Kdr}) to create spiking activity, as in other network models (Jones et al., 2000; Garabedian et al., 2003; Pinto et al., 2003). Parameters regulating the IN dynamics were length = 39 μm; diameter = 20 μm; $R_a = 200\ \Omega \cdot cm$; $C_m = 85\ \mu F/cm^2$; $g_{Na} = 0.12\ S/cm^2$; $g_K = 0.036\ S/cm^2$; $g_L = 0.003\ S/cm^2$; $E_{Na} = -50$ mV; $E_K = 77$ mV; $E_L = -54.3$ mV.

Local synaptic architecture. Each modeled cortical layer contained 10 PNs and three INs (Thomson et al., 2002). Local excitatory and inhibitory synapses within the SI cortical column model were constructed as shown in Figure 2*A*. Connection lines are schematic representations of axonal-to-dendritic input. Axons were not explicitly modeled. The local synaptic architecture was based on an abundance of animal studies and, in particular, studies of the mouse/rat somatosensory cortex (Bernardo et al., 1990a,b) [for review, see Thomson et al. (2002), Thomson and Bannister (2003), and Bannister (2005)]. Inhibitory synaptic connections onto PNs were located on the soma (Somogyi et al., 1983; Kisvarday et al., 1985; Freund et al., 1986), and excitatory synapses contacted the basal and apical oblique dendrites (Deuchars et al., 1994; Lubke et al., 1996; Thomson and Bannister, 1998; Feldmeyer et al., 2002). Fast and slow excitatory (AMPA/NMDA) and inhibitory ($GABA_A/GABA_B$) synapses were simulated using an α function that was "turned on" by the soma of the presynaptic cell crossing a voltage threshold (0 mV). The synaptic dynamics were defined by the following rise/decay time constants and reversal potentials, respectively: AMPA, 0.5/5 ms, 0 mV; NMDA, 1/20 ms, 0 mV; $GABA_A$, 0.5/5 ms, −80 mV; $GABA_B$, 1/20 ms, −80 mV. The strengths of the synaptic connections within the local network were defined with a Gaussian spatial profile, with a delay incorporated into the synaptic connection between two cells defined by an inverse Gaussian (Jones, 1986; Kaas and Garraghty, 1991). The maximum synaptic conductances and Gaussian weight space constants (number of cells from center) are listed in Table 2 along with the minimum synaptic delay and corresponding Gaussian delay space constant. The three INs in each layer were regularly distributed in space among the 10 PNs.

Exogenous drive. Exogenous drive to the local network was excitatory only (Cauller and Connors, 1994; Cauller et al., 1998; Guillery and Sherman, 2002) and was defined by the laminar location in SI of its synaptic effects based on general principles of cortical circuitry (Rockland and Pandya, 1979; Friedman and Jones, 1980; Felleman and Van Essen, 1991; Jones, 2001; Douglas and Martin, 2004). One source of drive emerged from the granular layer, layer 4 (L4), and contacted the L2/3 neurons, with a delayed and weaker connection to the infragranular L5 neurons (for specific poststimulus

Table 2. Local network synaptic connection parameters

	Maximal conductance (μS) AMPA/NMDA or $GABA_A/GABA_B$	Weight space constant	Min. delay (ms)	Delay space constant
L2/3e to L2/3e	0.001/0.0005	3	1	3
L2/3e to L2/3i	0.01	3	1	3
L2/3e to L5e	0.00025	3	3	3
L2/3e to L5i	0.00025	3	3	3
L2/3i to L2e	0.05/0.05	5	1	5
L2/3i to L5e	0.001	5	1	5
L2/3i to L2/3i	0.002	2	1	2
L5e to L5e	0.005/0.0005	3	1	3
L5e to L5i	0.001	3	1	3
L5i to L5e	0.025/0.025	7	1	7
L5i to 5i	0.002	2	1	2

Targeted dendritic compartments are outlined in Figure 1*A*. e, excitatory; i, inhibitory; min., minimum.

Table 3. Exogenous synaptic input parameters

	Input times across trials: Gaussian dist. mean/SD (ms)	Maximal conductance (μS) suprathreshold AMPA/NMDA	Maximal conductance (μS) threshold: nonperceived	Maximal conductance (μS) threshold: perceived
iGR to L2/3e		0.002	0.001	0.001
iGR to L2/3i		0.004	0.002	0.002
iGR to L5e		0.001	0.0005	0.0005
iGR to L5i	25/2.5	0.002	0.001	0.001
SGR to L2/3e		0.004/0.004	0.001/0.001	0.00105/0.00105
SGR to L2/3i		0.002/0.002	0.0005/0.0005	0.000502/0.0005025
SGR to L5e	70/6	0.004/0.004	0.001/0.001	0.00105/0.00105
IGR to L2/3e		0.08	0.0053	0.00689
IGR to L2/3i		0.08	0.0053	0.00689
IGR to L5e		0.04	0.0027	0.003471
IGR to L5i	135/7	0.04	0.0027	0.003471

Targeted dendritic compartments are shown in Figure 2, *C* and *D*. dist., Distribution; iGR, initial GR; SGR, SGR input; IGR, late GR.

dendritic compartments, see Fig. 2*C*). Activity in L4 is modeled to reflect drive from the thalamus and was based on several studies of intracranial laminar electrophysiological recordings of evoked responses in SI, including responses to vibrissa and thalamic stimuli in rodents (Di et al., 1990; Barth and Di, 1991; Castro-Alamancos and Connors, 1996; Kandel and Buzsáki, 1997; Douglas and Martin, 2004), trigeminal stimulation in piglets (Ikeda et al., 2005), and tactile (Kulics and Cauller, 1986; Cauller and Kulics, 1991) and median nerve stimuli in awake monkeys (Peterson et al., 1995; Lipton et al., 2006). A second source of drive to the SI network contacted the distal apical dendrites in the supragranular layers of each neuronal population (Fig. 2*D*). This connection could be representative of input from higher-order cortical areas or nonspecific thalamic sources (Rockland and Pandya, 1979; Friedman et al., 1980; Felleman and Van Essen, 1991; Jackson and Cauller, 1998; Jones, 2001; Douglas and Martin, 2004).

The sources of SI drive were modeled as spike generators with a predefined temporal profile, such that on a trial-by-trial ($n = 100$ trials) basis the presynaptic spike times were chosen from a Gaussian distribution to reproduce a physiologically realistic sequence of input to SI as follows: initial granular layer (GR) output, mean, 25 ms; SD, 2.5 ms; subsequent exogenous input to the supragranular layer (SGR), mean, 70 ms; SD, 6 ms; second later wave of GR output, mean, 135 ms; SD, 7 ms (Table 3) (all GR to L5 inputs had an additional fixed 5 ms conduction delay). The mean input timings in this sequence were chosen to be consistent with laminar recordings of electrical activity in SI during tactile (Kulics and Cauller, 1986; Cauller and Kulics, 1991; M. L. Lipton and C. E. Schroeder, personal communication), thalamic (Kandel and Buzsáki, 1997), and trigeminal (Ikeda et al., 2005) stimulation. The spatial distribution of the synaptic weights were uniform, as in Table 3. A baseline noise level was incorporated into the model by injecting a random amount of current into each neuronal compartment at each time step taken from a uniform distribution between −0.3 and 0.3 nA. This random noise was included to create heterogeneity in spike timing across the population and trials.

Parameter fitting. In each simulation presented, the biophysical properties of the cortical neurons, the intrinsic and exogenous synaptic connectivity, and the sequence in which exogenous drive arrived to the model (GR-SRG-GR) were fixed, based on previous physiological and anatomical findings. Our initial simulations with the model gave close to accurate matching with the MEG data, and parameter fitting was done empirically on only the relative strength and/or relative timing of the exogenous drives (given the fixed overall sequence) to best fit the MEG data. Specifically, we manually adjusted these parameters until our quantitative estimate of the current dipole moment (given in nA · m) matched those observed experimentally when multiplied by a constant network scaling factor of 3000. This scaling factor was fixed for each simulation.

Calculation of net current dipole. The SI ECD was calculated as the net sum across the population of the intracellular currents flowing within the PN dendrites in a direction perpendicular to the longitudinal axis of the apical dendrite multiplied by the corresponding length of the dendrite.

More simplified models, often referred to as "neural mass models," have been used to investigate signals underlying event-related MEG/EEG responses in the human brain (David et al., 2005, 2006a,b; Lee et al., 2006; Riera et al., 2006, 2007). These models generally assume that the MEG signal is proportional to some superposition of the model neurons' membrane potentials, which contribute to the mean state, and have succeeded in capturing basic features of MEG evoked responses. Consistencies between such simplified models and those that rely on details of the PN dendritic morphology and physiology remain to be investigated. However, our results and those from more reduced preparations (Murakami et al., 2002, 2003; Murakami and Okada, 2006) suggest that these nonspecific models will obscure predictions about primary ECD sources that depend crucially on intracellular dendritic currents.

Simulations. All simulations were performed using the shareware software program NEURON available at http://www.neuron.yale.edu/neuron/. A fixed-time-step implicit Euler integration method was used with a time increment $dt = 0.025$ ms. Results shown were smoothed with a 333 ms Hamming window. After publication, the code that produced all simulated data in this paper will be available on the ModelDB website, http://senselab.med.yale.edu/senselab/modeldb/, and we refer the reader here for equations regulating active current kinetics.

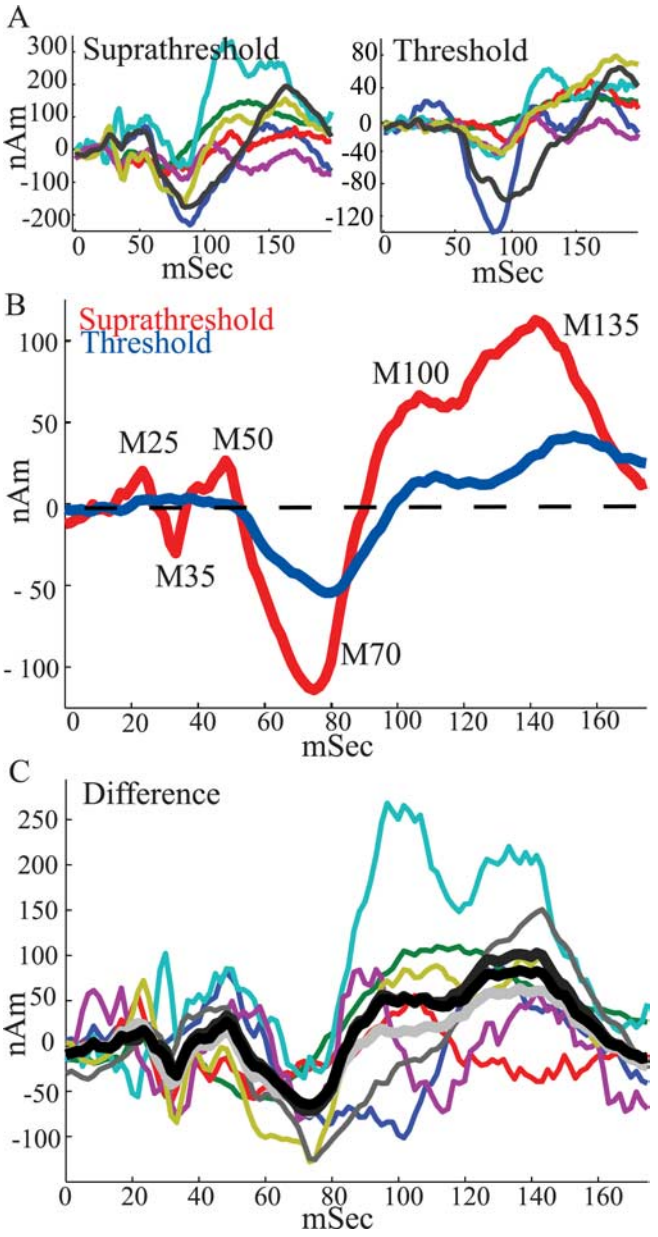

Figure 3. SI evoked responses. ***A***, SI ECD responses from individual subjects ($n = 7$; baseline, mean 0–20 ms subtracted for display purposes) for suprathreshold-level (left) and threshold-level (right) stimuli. ***B***, Average of suprathreshold-level (red curve) and threshold-level (blue curve) stimuli over all subjects. Consistent peaks emerged in the grand averages from 0 to 175 ms as labeled. Early peaks were not observed in the threshold response. ***C***, Colored curves, Difference between suprathreshold- and threshold-level responses from individual subjects. Black curve, Mean difference over all subjects. Dark gray curve, Mean difference over subjects excluding subject with smallest difference (red curve). Light gray curve, Mean difference over subjects excluding subject with largest difference (cyan curve). The mean differences show that the stimulus amplitude differences were not driven by the response of an outlier subject.

Results

MEG experiments

Features of SI evoked responses

A brief suprathreshold stimulus applied to the D3 digit tip evoked a robust and consistent response above the contralateral somatosensory cortex. The peak activity (~70 ms) of the estimated SI ECD reliably localized to the postcentral gyrus in the hand area of

SI, consistent with other studies of tactile stimulation to the fingers (Forss et al., 1994b; Hoechstetter et al., 2000, 2001; Kakigi et al., 2000; Braun et al., 2002; Druschky et al., 2003; Iguchi et al., 2005). Figure 1 shows representative examples of the location and orientation of the ECD on T1-weighted MRI images. Figure 1, *A* and *B*, is derived from the inverse solution technique described in Materials and Methods, and Figure 1*C* shows an example of one of two subjects for which the ECD was placed in area 3b. In each subject, the dipole was localized in the lateral edge of the hand area defined by the "Ω"-shaped passage of the central sulcus. Previous studies have shown that this position is consistent with the location of the finger representation in humans (Penfield and Rasmusson, 1950; Uematsu et al., 1992; White et al., 1997; Yousry et al., 1997; Sastre-Janer et al., 1998; Moore et al., 2000).

The SI ECD responses evoked by suprathreshold- and threshold-level stimuli showed reliable peaks with consistent polarity in all subjects. Figure 3 displays the SI response in each individual subject for suprathreshold- (Fig. 3*A*, left) and threshold (Fig. 3*A*, right)-level stimuli, averages across all subjects (Fig. 3*B*), and individual and mean differences between suprathreshold- and threshold-level responses (Fig. 3*C*). The average response to the suprathreshold stimulus (Fig. 3*B*, red curve) had an initial peak with positive polarity at ~25 ms (labeled M25), followed by a peak with negative polarity at ~35 ms (M35) and another smaller but consistent positive peak at ~50 ms (M50). The largest peak occurred at ~70 ms (M70) with a negative polarity, followed by two peaks with positive polarity at ~100 ms (M100) and ~135 ms (M135) (Forss et al., 1994b; Hoechstetter et al., 2001; Druschky et al., 2003).

When comparing suprathreshold- and threshold-level responses, several features of the evoked response were stimulus amplitude dependent. The amplitude of the dynamic threshold-level stimulus was always at least 120 μm smaller than the fixed stimulus amplitude of the suprathreshold stimulus (see Materials and Methods). The earliest peak evident in the threshold-level response (Fig. 3*B*, blue curve) was the M70. The M25-M35-M50 peaks in the threshold-level response are likely a result of the lack of sufficient signal-to-noise to detect the subtle early signal from the weak tactile stimulus. Although the observed M70 peak in the threshold-level response had the same negative polarity of the M70 peak of the suprathreshold-level response, the magnitude was smaller (M70 = minimum in 50–100 ms, paired *t* test, $p < 0.001$; ST, -130 ± 46 nA · m; T, -58 ± 27 nA · m) and the latency was longer ($p = 0.0661$; ST, 72 ± 9 ms; T, 80 ± 6 ms), resulting in a smaller onset slope to peak (slope from response at 50 ms to M70, $p < 0.0002$; ST, -6 ± 3 nA · m/ms; T, -2 ± 2 nA · m/ms). Two subsequent peaks with positive polarity, M100 and M135, were also evident in the threshold response. The magnitudes of these peaks and the area under the curve between them were smaller for the threshold-level response (M100 = maximum in 75–125 ms, $p < 0.02$; ST, 110 ± 80 nA · m; T, 26 ± 23 nA · m; M135 = maximum 125–175 ms, $p < 0.02$; ST, 127 ± 71 nA · m; T, 47 ± 30 nA · m; average magnitude, 100–150 ms, $p < 0.04$; ST, 82 ± 68 nA · m; T, 18 ± 19 nA · m). Furthermore, the latency of the M135 was longer ($p < 0.02$; ST, 140 ± 9 ms; T, 155 ± 8 ms) for the threshold-level response. The latency of the M100 peak was not significantly different for the threshold-level response ($p = 0.44$; ST, 113 ± 9 ms; T, 116 ± 7 ms). However, the onset slope to the M100 peak was smaller (slope from M70 to response at 100 ms, $p < 0.02$; ST, 7 ± 4 nA · m/ms; T, 3 ± 2 nA · m/ms).

Figure 3*C* shows that the stimulus amplitude-dependent differences were not driven by the response of an "outlier" subject. Displayed are the differences between the suprathreshold- and

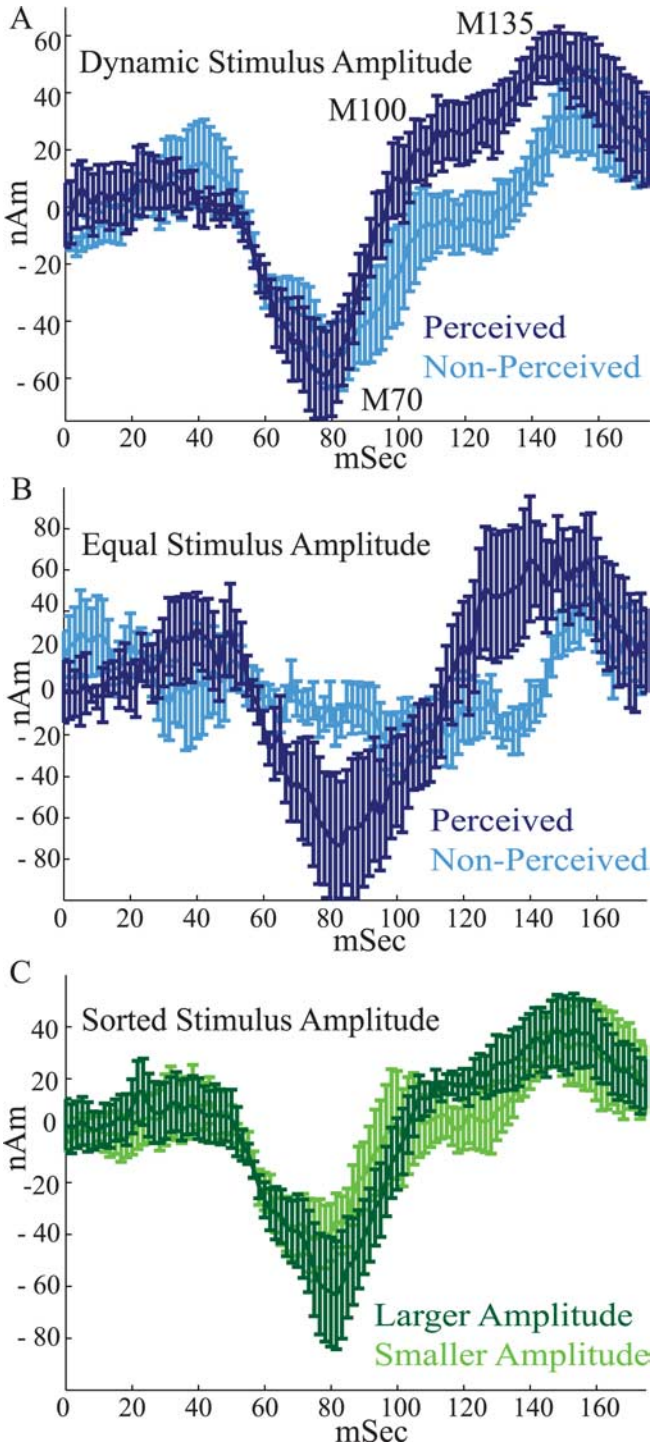

Figure 4. The magnitude and timing of the SI evoked response predict perception. ***A***, Threshold-level stimulus SI evoked responses averaged over perceived (dark blue) and nonperceived (light blue) trials for varying stimulus amplitudes that were dynamically maintained at 50% perceptual threshold (trials = 100; $n = 7$). On perceived trials, the onset slope from the M70 to the M100 peak was larger, and the magnitudes of the M100 and M135 peaks and area under the curve between them were larger. ***B***, Average threshold-level responses comparing perceived and nonperceived trials that had equal stimulus amplitudes (trials = 19 ± 9; $n = 6$; for details, see Results). On perceived trials, the magnitude of the M70 peak and onset slope from M70 to M100 were larger in this comparison. ***C***, Average threshold-level responses sorted by stimulus amplitude. Dark green, Larger stimulus amplitudes; light green, smaller stimulus amplitudes (trials = 100 trials; $n = 6$). There were no statistically significant differences in this comparison. Error bars represent SEM.

threshold-level responses for each subject (thin colored curves), along with the mean difference across all subjects (thick black curve), the mean excluding the subject with the smallest difference (thick dark gray curve; excludes red curve), and the mean excluding the subject with the largest mean differences (thick light gray curve; excludes cyan curve). The excluded subjects were based on the mean absolute difference from 0 to 175 ms (smallest = 23.71 nA · m; median = 49.65 nA · m; largest = 96.2 nA · m).

The SI evoked response predicts perception

We used an adaptive stimulus algorithm, such that the threshold-level stimulus amplitude was maintained dynamically at ~50% detection rate (Dai, 1995; Leek, 2001). Because misses [i.e., nonperceived (NP) trials] in this design will, on average, occur for lower-amplitude stimuli, differences observed in stimulus response for perceived (P) and nonperceived trials could simply reflect peripheral input amplitude. Therefore, we analyzed the correlation between the SI evoked response and perception in two ways, each of which showed statistically significant differences between perceived and nonperceived trials (Fig. 4*A*,*B*).

In the first analysis, we averaged the last 100 trials of perceived and nonperceived stimuli to minimize within-session training effects (Fig. 4*A*) ($n = 7$). This dataset provided a strong statistical sample and showed that the onset slope from the M70 to the M100 peak was larger for perceived (dark blue) than for nonperceived (light blue) trials (slope from 70 to 100 ms, $p < 0.002$; P, 2 ± 2 nA · m/ms; NP, 0.5 ± 2 nA · m/ms), and the magnitudes of the M100 and M135 peaks and area under the curve between them were larger (M100 = maximum in 95–110 ms, $p < 0.04$; P, 31 ± 27 nA · m; NP, 1 ± 38 nA · m; M135 = maximum 120–175 ms, $p < 0.02$; P, 68 ± 26 nA · m; NP, 43 ± 32 nA · m; average magnitude, 100–150 ms, $p < 0.02$; P, 32 ± 22 nA · m; NP, 1 ± 20 nA · m). Other trends that did not reach significance were present in SI. These included shorter latencies to the M70 and M135 peaks for the perceived stimuli (M70, $p = 0.0918$; P, 74 ± 11 ms; NP, 84 ± 10 ms; M135, $p = 0.1253$; P, 143 ± 16 ms; NP, 154 ± 12 ms).

In the second analysis, for each subject, we subsampled the dataset and analyzed an equal number of hit and miss trials from an equal stimulus amplitude (Fig. 4*B*). The amplitude selected for analysis was the level that was most commonly encountered by a given subject (mean number of trials, 19; SD, 9; $n = 6$ subjects; for one subject, the data file containing stimulus amplitudes was corrupted). The signals generated during perceived and nonperceived trials in this "equal" condition also showed significant differences between hit and miss trials. The mean response for perceived trials showed a well defined M70 peak (minimum, 70–145 ms; magnitude, −118 ± 89 nA · m; latency, 90 ± 5 ms), whereas nonperceived trials did not. When comparing the M70 peak for perceived trials with the temporally aligned 90 ms (mean latency for perceived trials) response for nonperceived trials, the magnitude was larger for perceived trials (M70 magnitude, $p < 0.05$; P, −118 ± 89 nA · m; NP, −6 ± 33 nA · m), as was the onset slope to the M100 (slope M70 to M100 = magnitude at 125 ms, $p < 0.05$; P, 5 ± 4 nA · m/ms; NP, 0.003 ± 2.101 nA · m/ms). The significant differences in the M100 and M135 magnitude, and area under the curve between them, that emerged in the larger dataset showed a trend, but did not reach statistical significance, in the equal condition analysis (M100 = maximum at 125 ms, $p = 0.1151$; P, 51 ± 80 nA · m; NP, −9 ± 42 nA · m; M135 = maximum 125–175 ms; magnitude, $p = 0.0787$; P, 123 ± 72 nA · m; NP, 70 ± 33 nA · m; average magnitude, 100–150 ms, $p = 0.146$; P, 27 ± 52 nA · m; NP, −9 ± 15 nA · m).

In a third analysis (Fig. 4*C*), we sorted the threshold-level responses by stimulus amplitude to test whether threshold-level stimulus amplitude was a better predictor of response magnitude. We found that the average responses to the largest (L) and smallest (S) threshold-level stimulus amplitudes (Fig. 4*C*, dark and light green curves, respectively) (100 trials each; $n = 6$ subjects) showed no statistically significant difference at any time in the 0–175 ms response (M70 magnitude = minimum 50–100 ms, $p = 0.08$; L, −81 ± 51 nA · m; S, −65 ± 39 nA · m; M70 latency, $p = 0.5$; L, 81 ± 13 ms; S, 76 ± 14 ms; slope M70 to M100 = maximum 95–110 ms, $p = 0.16$; L, 4 ± 3 nA · m/ms; S, 3 ± 3 nA · m/ms; M100 magnitude, $p = 0.9$; L, 21 ± 21 nA · m; S, 20 ± 46 nA · m; M135 magnitude = maximum 120–175 ms, $p = 0.5$; L, 62 ± 36 nA · m; S, 53 ± 31 nA · m; M135 latency, $p = 0.4$; L, 152 ± 9 ms; S, 147 ± 16 ms; average magnitude, 100–150 ms, $p = 0.11$; L, 25 ± 16 nA · m; S, 14 ± 21 nA · m). This analysis shows that detection probability is a better predictor of variance in the SI response than peripheral stimulus amplitude.

Computational neural modeling

The ECD inverse modeling technique that we used allowed us to infer the magnitude and direction of the net current flow from a dipole source within a local cortical region. In the observed SI ECD responses, positive polarity corresponds to net current flow anterior, which in the case of area 3b corresponds to flow toward the cortical surface, and negative polarity corresponds to net current flow toward the white matter. Confidence that the early ECD signal arises from somatosensory area 3b, without contribution from other neighboring somatosensory areas, comes from the fact that, unlike the surrounding somatosensory areas 1 and 3a, the orientation of area 3b in the postcentral gyrus is tangential to the nearby inner skull surface, which makes it particularly well situated for MEG imaging (Hämäläinen et al., 1993). The magnitude of the ECD is commonly believed to result from the net current flow in the dendrites of a synchronous population of PNs, with the polarity determined by the direction of this current flow (Hari et al., 1980; Hämäläinen et al., 1993; Okada et al., 1997; Ikeda et al., 2005). Thus, to understand the local cortical dynamics that induced the magnitude and polarity of the observed ECD responses, we developed a biophysically realistic laminar cortical model of a local SI network, representing area 3b. Simulations of net current flow within PNs in the model were used to make predictions on the underlying network dynamics that define the evoked responses and their relation to perception.

A schematic of the local SI network is shown in Figure 2*A*. The model consisted of excitatory PNs and INs in L2/3 and L5, shown in light green and red, respectively. To maintain accurate morphology, the PNs were modeled with multiple dendritic compartments, and they contained active conductances in their soma and dendrites to reproduce realistic spiking patterns to somatic injected current (1 nA) (Fig. 2*B*). The INs were represented as single compartment spiking neurons in each layer and were included to simulate their postsynaptic effects in the network. Synaptic connections in the model included local synapses (Fig. 2*A*), and exogenous drive simulated as (1) output from activity in the GR, representative of activity induced by the lemniscal thalamus (Fig. 2*C*), and (2) input to the SGR, representative of input from higher-order cortex or nonspecific thalamic sources (Fig. 2*D*). The GR output and input to the SGR were each modeled as a spike train generator that consisted of a single spike on each trial with a mean latency across trials ($n = 100$) taken from a Gaussian distribution, as described in Materials and Methods and Table 3.

All parameters, including intrinsic currents, connectivity, and

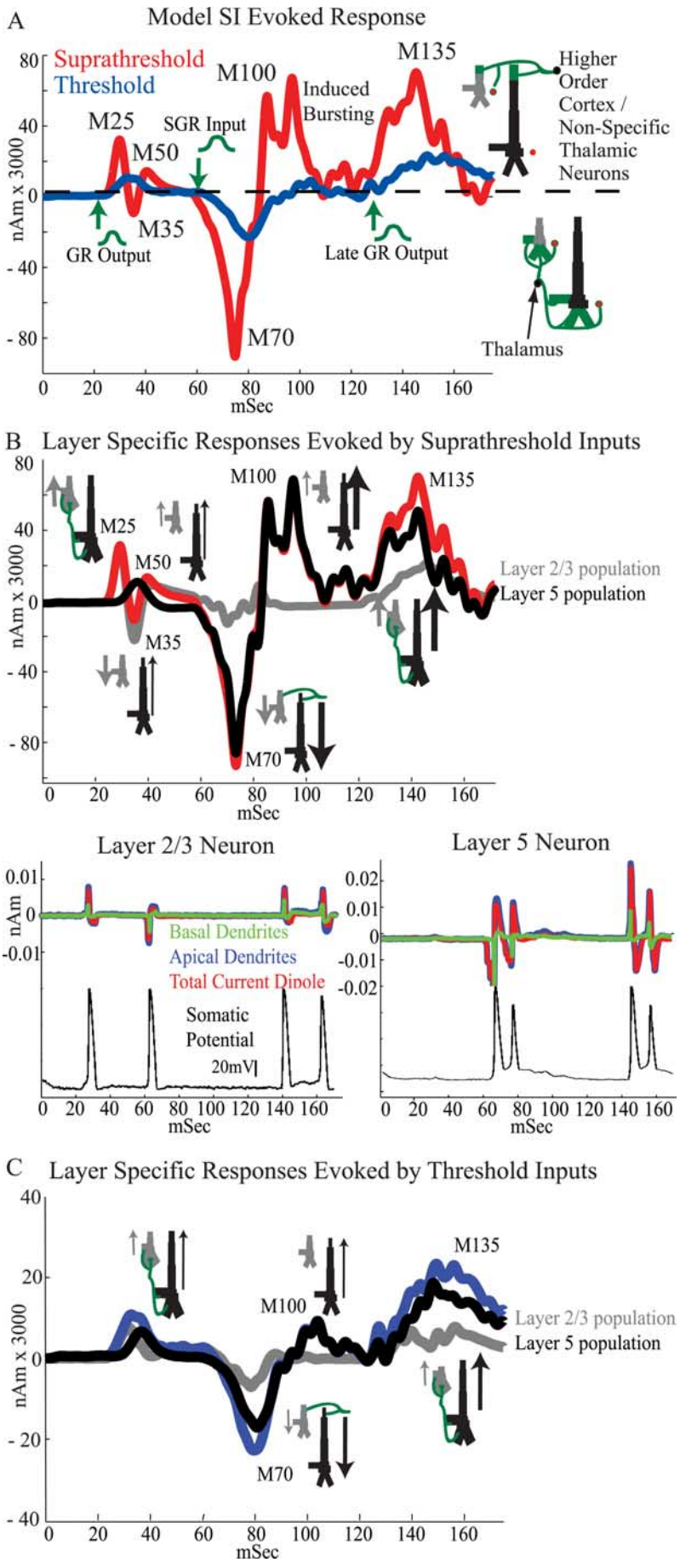

cell morphology, were derived from published experimental and modeling studies of mammalian neocortex, primarily from the somatosensory system (for relevant literature, see Materials and Methods and Discussion). The model construction enabled us to investigate the influence of a physiological sequence of exogenous drive on the ECD produced by the local SI network. The relative timing and strength of the exogenous drives were the only "free" parameters in the model that were adjusted to accurately simulate the MEG evoked signal.

Polarized current flow driven by a sequence of exogenous drive to SI predicts the temporal sequence of the evoked response

Having set the intrinsic network parameters and synaptic architecture in the model, we reproduced the evoked response by simulating a specific sequence of excitatory drive to the SI model (Fig. 5). The sequence consisted of output from activity in the GR emerging at ~25 ms, followed by input to the SGR at ~70 ms and a subsequent late wave of GR output at ~135 ms. Each input time was chosen from a Gaussian distribution across trials (Table 3), as shown schematically in green in Figure 5*A* with an arrow indicating the mean input times. This pattern of synaptic drive could be interpreted as initial feedforward input arriving from the lemniscal thalamus to the GR, followed by feedback input from a higher-order cortical area or nonspecific thalamic neurons to the SGR, followed by a late lemniscal thalamic input to the GR induced as part of a thalamocortical loop of activity (see Discussion). Figure 5*A* (red curve) shows the net current dipole from the PN population resulting from this pattern of synaptic drive averaged over 100 simulations, with suprathreshold-level synaptic conductances as in Table 3. The feedforward output from the GR at ~25 ms (Gaussian mean, 25 ms; SD, 2.5 ms) induced the entire initial dipole volley containing the

Figure 5. Simulated SI evoked responses for suprathreshold- and threshold-level stimuli. ***A***, The timing and location of synaptic inputs sets SI ECD polarity in the model. Red curve, Suprathreshold response. Output from activity in the GR at ~25 ms reproduces the initial M25-M35-M50 peaks, exogenous SGR input at ~70 ms created the subsequent M70 and M100 peaks, and second later GR output at ~135 ms induced the M135 peak. Input times were selected over trials from Gaussian distributions displayed schematically in green with arrows marking the earliest input times (Table 3) (average of 100 trials). Blue curve, Threshold response. Decreasing the synaptic strengths by 50% (GR), 25% (SGR), and 7% (late GR) reproduced the waveform for the threshold-level stimulus (compare with Fig. 3*B*). ***B***, Top, Contributions to the net current dipole during the suprathreshold response separated by layer. Bottom, Example of the activity from an individual L2/3 (left) and L5 (right) PN on a single trial; top traces, separate contributions from the basal (green) and apical (blue) dendritic compartments to the total current dipole (red) produced by the neuron; bottom traces, somatic membrane potential showing action potentials (black). ***C***, Contributions to the net current dipole during the threshold response separated by layer. ***B***, ***C***, Schematics of network architecture drawn at each peak and arrows describe the direction of the net intracellular current flow within the pyramidal neurons that determines the polarity of the peak.

M25-M35-M50 peaks. We describe the origin of each induced peak separately.

M25 origin

The separate contribution to the population average suprathreshold response from L2/3 (gray) and L5 (black) PN populations are shown in Figure 5*B* (top) along with representative contributions from a single L2/3 and L5 PN during a single trial (bottom). As shown in Figure 5*B* (top), the M25 peak was primarily induced by the activity of the L2/3 PNs because the GR output to L5 PNs was weaker and delayed (Bannister, 2005). The 25 ms input to the L2/3 PNs was strong enough to induce somatic spikes that back-propagated into the apical and basal dendrites, as shown in the example neuron in Figure 5*B* (bottom left) (Stuart and Sakmann, 1994; Murakami et al., 2002). The contributions from the apical (red) and basal (green) dendrites to the total dipole current (blue) produced by a single L2/3 PN are shown separately, as well as the somatic membrane potential (black). The back-propagation of current up the apical dendrites in the L2/3 PNs created a net current flow in the cell, and in the nearly synchronous population, that was directed upward, and hence the net dipole had positive polarity at the M25 peak (Fig. 5*A*, red curve). The timing and duration of the M25 peak were set by the kinetics of active currents in the L2/3 PN dendrites, the slight heterogeneity in spike timing across the population, and the Gaussian distribution of GR output times across trials.

M35 origin

A subsequent repolarization of the L2/3 dendrites created a net downward current flow and induced the negative M35 peak (Fig. 5*B*, top, gray curve; bottom left, red curve). The absolute magnitude of this peak was diminished by the initial current flow in the L5 PNs that was delayed and opposite in direction (Fig. 5*B*, top, black curve). Although the drive to the L5 neurons was not strong enough to create spiking, it did induce currents that back-propagated up the L5 dendrites creating a net positive current dipole in the population. The duration of this peak was again influenced by the kinetics of the L2/3 PN active dendritic currents, as well as the time course of inhibitory synaptic activity near the soma.

M50 origin

The subsequent positive M50 peak was induced by a combination of continued synaptic activity within the L2/3 network from the initial drive, via the local network connections, and the residual excitatory synaptic activity in the L5 PNs.

M70 origin

The large negative M70 peak (Fig. 5*A*, red curve) was reproduced by simulating excitatory drive to the SGR at ~70 ms (Gaussian mean, 70 ms; SD, 6 ms). This SGR input induced downward currents in the apical dendrites of each PN population (Fig. 5*B*, top). Although the strength of input was the same to each population, the activity induced in the L5 PNs dominated the resulting net dipole because of the larger length and diameter of their dendrites (Fig. 5*B*, top, black trace). The strength of the SGR input was sufficient to induce bursting activity in the somata of the L5 PNs. An initial downward current in the apical dendrites that lasted ~10 ms preceded each spike in the burst (Fig. 5*B*, bottom right). These downward currents created a net negative response across the population and hence the negative M70 peak. The duration of this peak was again set by a combination of active dendritic current dynamics, slight heterogeneity in burst timing across the population, and the Gaussian distribution of feedback input timing across trials.

M100 origin

After each spike in the burst, there was an active back-propagation of current up the apical dendrites of the L5 PNs (Fig. 5*B*, bottom right), and this upward current flow created the positive M100 peak in the average dipole. The duration of the bursting activity in the L5 PNs was an essential feature in defining the duration of the M100 peak activity (Fig. 5*A*, red curve).

After the M100 peak activity, the simulated dipole current returned to baseline, creating an apparent discrepancy between the simulated evoked dipole (Fig. 5*A*) and the observed average evoked dipole (Fig. 3*B*), which fell toward, but did not completely return to, baseline after the M100 peak. This inconsistency arose from the fact that in our model the bursting activity of the L5 PNs ended nearly synchronously across the population. We predict that simulations of a larger network model that incorporates more heterogeneity and perhaps subclusters of synchronous networks would rectify this discrepancy.

M135 origin

To reproduce the positive M135 peak, a late GR output at ~135 ms (Gaussian mean, 135 ms; SD, 7 ms) was simulated. This drive acted in conjunction with the low level of ongoing spiking network activity to create a more synchronous activity profile. Again this spiking created a dominant active back-propagation of current up the apical dendrites of the PNs, and hence a net current dipole with positive polarity (Fig. 5*A*, red curve).

The arrows located next to the PNs in the network schematics in Figure 5*B* (top; similarly in Fig. 5*C*) emphasize the fact that positive polarity in the SI response was created by a net intracellular current flow up the apical dendrites of the PNs induced by back-propagation of spiking activity (M25, M100, and M135) and excitatory synaptic inputs on the basal and oblique dendrites (M50), whereas negative polarity was created by a net intracellular current flow down the apical dendrites of the PNs induced by postspike repolarization of the apical dendrites (M35) and excitatory synaptic input to the most distal apical dendrites (M70). To accurately reproduce the magnitude of the observed MEG dipole peaks, which were on the order of 50–100 nA · m for the suprathreshold-level stimulus, the model results were multiplied by a scaling factor of 3000 (Fig. 5*A*,*B*). Thus, because there were 10 PNs in L2/3 and L5, the model predicts that ~60,000 PNs contribute to the net dipole created from the brief tactile stimulus used. This prediction is in agreement with previous predictions by Murakami and Okada (2006), who used simulations of single neocortical PNs to predict that ~50,000 synchronously firing neurons may be simultaneously active to produce an observable MEG response. Furthermore, Murakami et al. (2002, 2003) have shown in models of hippocampal neurons that back-propagation of PN action potentials can create measurable dipole currents directed away from the soma and that extracellular stimulation of apical dendrites can induce measurable currents in the opposite direction.

Weak exogenous drive reproduced the threshold-level response

By decreasing the strength of each of the synapses activated by the exogenous drive to the network, while keeping the same input sequence and timing (GR ~25 ms/SGR ~70 ms/late GR ~135 ms), and all other network parameters fixed as in the simulation of the suprathreshold-level stimuli, the waveform of the observed dipole evoked from threshold-level stimulation emerged (Fig. 5*A*, blue curve; for synaptic conductances, see Table 3, threshold

level, nonperceived). With this simple manipulation, the differences between the simulated threshold and suprathreshold-level responses were almost entirely consistent with those seen experimentally. First, the weaker (50% smaller than the suprathreshold simulation) initial GR output at ~25 ms was not strong enough to induce initial M25-M35-M50 peaks. This output did create a small positive peak before 50 ms because of back-propagation of current in the dendrites of both the L2/3 and L5 PN populations (Fig. 5*C*). The subsequent negative deflection from repolarization of the dendrites could be seen in the L2/3 population (Fig. 5*C*, gray curve); however, this effect was negligible in the total population response (Fig. 5*C*, blue curve). This early peak was not distinguishable from the prestimulus level of activity in the experimental data (Figs. 3, 4), likely because of a lack of signal-to-noise in the MEG measurement. We anticipated that the initial peak could be eliminated in the model by increasing the level of baseline noise and/or decreasing the initial GR output strength. However, based on the known physiology of input to the cortex from the periphery, we assumed that the initial thalamic input/GR output was present at threshold, albeit weakly. Second, the magnitude of the M70 peak was smaller and, although there was no manipulation in the timing of input, the longer latency and smaller onset slope of the induced M70 peak emerged naturally from the underlying network dynamics, which exhibited a slower and smaller recruitment of net activity from the weaker (25% smaller than the suprathreshold simulation) SGR input (M70 magnitude, $p < 0.001$; ST, -543 ± 7 nA · m; T, 70 ± 29 nA · m; latency, $p < 0.001$; ST, 76 ± 5 ms; T, 79 ± 7 ms; SD, 7; onset slope, $p < 0.001$; ST, -22 ± 6 nA · m/ms; T, -2 ± 1 nA · m/ms). As in the suprathreshold simulation, the activity in the L5 PN population dominated the M70 peak because of the larger length and diameter of the L5 PN dendrites (Fig. 5*C*, compare gray and black curves). The decrease in network activity also recreated the smaller magnitude and onset slope to the M100 peak (M100 magnitude, $p < 0.003$; ST, 453 ± 2 nA · m; T, 66 ± 67 nA · m; onset slope, $p < 0.001$; ST, 26 ± 9 nA · m/ms; T, 3 ± 2 nA · m/ms), which was again dominated by the L5 network (Fig. 5*C*, black curve). Last, the weaker (7% smaller than the suprathreshold simulation) late GR output at ~135 ms also induced a smaller and slower network response, recreating the smaller magnitude and increased latency of M135 peak (M135 magnitude, $p < 0.001$; ST, 860 ± 56 nA · m; T, 230 ± 68 nA · m; latency, $p < 0.001$; ST, 137 ± 7 ms; T, 142 ± 6 ms), and the mean difference in the area under the curve between the M100 and M135 peaks ($p < 0.001$; ST, 26 ± 8 nA · m; T, 8 ± 4 nA · m).

Timing and magnitude of SGR input and late GR output predict perception

Significant differences between the experimentally observed SI evoked responses from the perceived and nonperceived threshold-level stimuli emerged beginning with the M70 peak (Fig. 4). Our model results predict that the M70 peak and subsequent activity come from exogenous drive to the SGR of SI at ~70 ms, followed by a later output from the GR at ~135 ms (Fig. 5). As such, an additional prediction from the model was that observed differences in the SI evoked responses for perceived and nonperceived trials arose from differences in the timing and magnitude of these drives. Specifically, we predicted that on perceived trials the SGR input and late GR output arrive earlier and are stronger. By simulating these effects in our SI model, we reproduced the observed differences in the evoked response with perception.

Figure 6 shows the SI evoked responses for simulated perceived (dark blue) and nonperceived (light blue) trials averaged over 100 trials. The results in this figure are comparable with those in Figure 4*A*, where several statistically significant differences between perceived and nonperceived trials emerged. The parameters reproducing the response from nonperceived trials were the same as those producing the threshold-level response in Figure 5*A*. To reproduce the response from perceived trials, the mean latencies of the SGR input and late GR output were each decreased by 5 ms (to 65 and 130 ms, respectively), and the synaptic strengths were increased by 5 and 30% from the default values, respectively (see Table 3). These parameter changes reproduced the observed correlates of perception in SI, including an increase in M70 magnitude with perception (significant in the equal stimulus amplitude data in Fig. 4*B*) (model statistics, $p < 0.001$; P, -70 ± 29 nA · m; NP, -93 ± 44 nA · m), the larger onset slope to the M100 peak (slope from M70 to M100, $p < 0.003$; P, 27 ± 34 nA · m/ms; NP, 16 ± 17 nA · m/ms), and the larger magnitude of the M100 and M135 peaks and mean area under the curve between them (M100 magnitude, $p < 0.001$; P, 112 ± 84 nA · m; NP, 65 ± 67 nA · m; M135 magnitude, $p < 0.001$; P, 253 ± 64 nA · m; NP, 230 ± 23 nA · m; area between 100 and 150 ms, $p < 0.001$; P, 13 ± 4 nA · m; NP: 8 ± 4 nA · m). Surprisingly, although the mean latency of the SGR input and late GR output were each decreased by 5 ms to simulate perceived trials, consistent with the experimental data, on the average the latency difference of the M70 remained significant, whereas the latency difference of the M135 peak emerged only as a trend (M70 latency, $p < 0.001$; P, 76 ± 7 ms; NP, 79 ± 7 nA · m; M135 latency, $p = 0.1075$; P, 136 ± 7 ms; NP, 137 ± 6 ms).

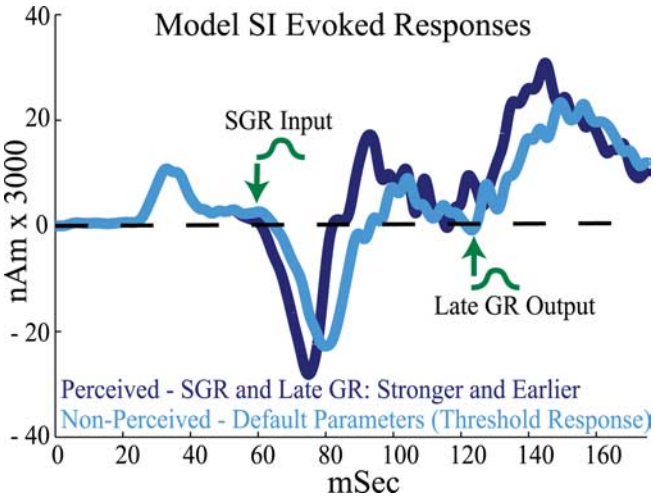

Figure 6. Simulated SI evoked responses for perceived and nonperceived trials (compare with Fig. 4*A*). The statistically significant differences in the SI evoked responses for perceived (dark blue) versus nonperceived (light blue) trials were reproduced in the model by decreasing the mean latency and increasing the synaptic input strength of the SGR input and late GR output. For perceived trials, the mean SGR input and late GR output latencies were each decreased by 5 ms (to 65 and 130 ms, respectively) and their strengths were increased by 5% and 30%, respectively (Table 3) (average of 100 trials). The initial GR output was fixed. The green arrows and schematic Gaussians mark the distributions and earliest input times for perceived trials. These manipulations reproduced the increase in M70 magnitude, the larger onset slope to the M100 peak, the larger magnitude of the M100 and M135 peaks, and the greater mean area under the curve between them. Nonperceived trials were simulated with default parameters that produced the threshold-level response in Figure 5*A*.

Discussion

We combined human MEG and computational modeling to investigate the cortical dynamics underlying tactile detection. This

combination of *in vivo* experimental data and biophysically constrained modeling led to four key results. First, brief tactile stimuli to a subject's fingertip evoked a consistent SI MEG signal that could be well localized to the position of area 3b. Second, the SI response predicted detection beginning ≥70 ms after stimulus. Third, simulation of an SI evoked response with a cortical model reproduced all major peaks recorded, providing a solution to the MEG signal based in cell-type- and lamina-specific activity patterns. This modeling led to the novel prediction that the polarity and magnitude of peaks in the SI response were induced by a sequence of exogenous excitatory drive consisting of GR output at ~25 ms, followed by SGR input at ~70 ms, followed by a late GR output at ~135 ms. This sequence may be interpreted as initial input from the periphery through the lemniscal thalamus to GR, followed by feedback input from higher-order cortex or nonspecific thalamus to SGR, followed by a second wave of lemniscal thalamic input to GR. Using this network, we were also able to simulate differences in the magnitude and onset timing of peaks in the SI evoked response for suprathreshold- and threshold-level stimuli by decreasing the strength of exogenous drive. Fourth, specific manipulations of the model reproduced differences in observed MEG response that correlated with perception. Specifically, perceived threshold-level stimuli were characterized by SGR inputs and late GR outputs with earlier latencies and stronger amplitudes.

Because the synaptic architecture in the model was based on general principles of anatomy and physiology in a laminated cortex, our results are likely to be applicable to the interpretation of evoked MEG signals from primary sensory areas during a range of cognitive tasks, specifically in the interpretation of studies that report changes in peak latency and/or magnitude as a marker for changes in perception, attention, and brain disease.

Origin of evoked response and modulation with detection

Our model provides a realistic network that predicts the electrophysiological origin of the evoked SI response and its correlates with human perception. These predictions are consistent with previous studies. Studies focused specifically on investigating the neural origin of primary somatosensory evoked surface potentials (SEPs) (Towe, 1966; Arezzo et al., 1979, 1981; Allison et al., 1980; Gardner et al., 1984; Desmedt, 1988; Peterson et al., 1995) and fields (SEFs) (Hari and Forss, 1999; Ikeda et al., 2005) have primarily analyzed peaks emerging <50 ms after stimulus. A consensus from studies in which electrophysiological activity was recorded from multiple cortical layers is that the net laminar current flow that produces these early evoked responses derives from the postsynaptic current flow in PNs in the supragranular and infragranular layers (Towe, 1966; Peterson et al., 1995; Ikeda et al., 2005). Our data are consistent with a recent study by Ikeda et al. (2005) that showed with simultaneous MEG and intracranial laminar recordings in piglet SI that the first recorded SEF peak (N20, analogous to M25) from trigeminal nerve stimulation is generated by intracellular currents in two populations of excitatory neurons that appear to fire initially in the soma and produce back-propagating spikes toward distal apical dendrites. The predicted origins of the M35 and M50 peaks have yet to be verified.

A key hypothesis from our study is that tactile detection correlates with the SI evoked response beginning at the M70 peak. The M70 and M100 were reproduced in the model by simulating excitatory synaptic input at ~70 ms to the SGR (layers I/II). The importance of this input is supported by the work of Kulics and Cauller, who recorded laminar profiles of local field potential and multiunit activity from the PoCG of awake monkeys during detection of cutaneous electrical stimulation (Kulics and Cauller, 1986; Cauller and Kulics, 1991; Jackson and Cauller, 1998). Their data showed an SEP between 50 and 65 ms, N1, corresponding to our M70 that was created by excitatory input to layers I/II that induced spiking in the deep layers. This result is consistent with our findings that excitatory input to the dendrites of the L2/3 and L5 neurons in the SGR induced spiking and bursting activity. Laminar profiles of SI activity that indicate excitatory input to the SGR at consistent latencies are also observed during tactile stimulation in anesthetized rats (Di et al., 1990; Barth and Di, 1991) and during brief tactile finger stimuli in awake monkeys (Lipton and Schroeder, personal communication).

There are two primary candidate sources of exogenous input to supragranular SI. One is "higher-order" cortical inputs, including possibly those from SII (Friedman et al., 1980; Cauller et al., 1998; Jackson and Cauller, 1998) or the frontal cortex (FC) and posterior parietal cortex (PPC) (Mauguiere et al., 1997a,b; Staines et al., 2002; Golmayo et al., 2003; Bauer et al., 2006). Human studies that show a peak in evoked activity in the parietal operculum at 70 ms during median nerve and tactile stimuli support SII as a source of M70 input (Karhu and Tesche, 1999; Hoechstetter et al., 2000, 2001). We investigated SII activation in the current dataset, but the signal-to-noise ratio from this second source modeled was too low to allow quantitative interpretation (data not shown), and no other sources could be estimated. Activations of the FC and PPC with somatosensory stimuli may require median nerve stimulation (Forss et al., 1994a,b, 1996; Mauguiere et al., 1997a,b). A second possible source of SGR input is a class of widespread calbindin-staining thalamic neurons that project diffusely to these layers (Jones, 2001).

To recreate the M135 activity in the SI model, a second output from the GR was necessary. This second wave of lemniscal thalamic input is consistent with the induction of a reverberatory thalamic-cortical-thalamic cycle (Kandel and Buzsáki, 1997; Jones, 2001; Guillery and Sherman, 2002; Nicolelis and Fanselow, 2002; Sherman and Guillery, 2002). Laminar profiles of activity that show patterns consistent with input to the GR at 100–140 ms latencies have been observed in SI of awake rats during thalamic stimulation (Kandel and Buzsáki, 1997) and in awake monkeys after tactile stimulation (Lipton and Schroeder, personal communication).

The correlates of detection in SI were reproduced in the model by decreasing the latency and increasing the strength of the later (~70 and ~135 ms) exogenous drives. The decrease in latency was modeled as a 5 ms decrease in the mean of the Gaussian distribution of presynaptic spike timing over trials. Thus, a prediction of our findings is a decrease in firing latency in the presynaptic areas that drive the M70/M100 and M135 responses. The increase in strength was modeled as an increase in the synaptic conductance of the targeted PN dendrites. Several mechanisms could underlie this increase, including an increase in the active conductance of the synapse, possibly via neuromodulators (McCormick, 1992; Hasselmo, 1995; Sarter et al., 2005; Yu and Dayan, 2005), or changes in the presynaptic source such as an increase in synchrony and/or firing rate. Support for such changes has been observed in SII during somatosensory detection and attention tasks (Garcia-Larrea et al., 1991; Hsiao et al., 1993; Hoechstetter et al., 2000; Steinmetz et al., 2000; Eimer and Forster, 2003; de Lafuente and Romo, 2006; Moore et al., 2007) and in FC during tactile detection (de Lafuente and Romo, 2005, 2006; Palva et al., 2005), and implicated in a class of thalamic neurons that project directly to SGR (Jones, 1998, 2001).

SI correlates of detection: comparison with previous studies

Other studies have investigated tactile detection in awake primates and have found correlations between SI activity and perception. A

MEG study by Palva et al. (2005) used a fixed-amplitude electrical current with an immediate motor report. Although the signal was not localized with ECD methods, the rectified response (30–150 ms) from sensors over sensorimotor cortex was larger in magnitude for perceived stimuli. Presuming that the activity they recorded was generated in part in SI, these results predict a subset of our findings. In the present study, the ECD SSP method allowed localization of activation to area 3b, and computational neural modeling demonstrated a specific sequence of cellular events through which the SI circuit can produce these changes.

Kulics and Cauller (Kulics, 1982; Kulics and Cauller, 1986; Cauller and Kulics, 1991) observed a correlation between the magnitude and latency of the N1 and detection in awake monkeys. Given the similarity in the origin and character of the N1 and M70, our findings are in good agreement. Our finding that the magnitude of the M135 correlates with tactile detection is also in agreement with the correlation they observed between the magnitude of the later P2 peak (105–130 ms) and behavioral response latency.

Our findings are in apparent disagreement, however, with recent studies from macaque monkeys trained to tactile detection (de Lafuente and Romo, 2005, 2006). Our MEG signal and the activity in the model that provided a robust fit to the data predict robust increases in action potential firing rate on detected trials in SI, whereas these previous studies reported no difference in SI for hits and misses. This discrepancy could have many explanations, including differences in stimuli, subject training, and/or species differences. However, the strong agreement between the present findings and other data from well trained monkeys (Kulics, 1982; Kulics and Cauller, 1986; Cauller and Kulics, 1991) and rats (Krupa et al., 2004) argues against the latter interpretations. Another possible difference is the mode of electrophysiological recording conducted, the measurement of single neuron action potential activity versus synchronous activity across populations of neurons. That said, our modeling strongly suggests that differences in action potential firing rate should be present in large L5 PNs, putatively a population that is frequently recorded using thresholded extracellular recording techniques. Additional studies targeted to reconciling these data are required.

State-dependent regulation of detection

Recent tactile detection studies reported an impact of ongoing rhythmic activity in rolandic cortex on perception (Linkenkaer-Hansen et al., 2004; Palva et al., 2005), such that detection was dependent on power and phase locking in multiple frequency bands, with a dominant dependence in the α range (8–14 Hz) (see also Worden et al., 2000). Gamma frequency activity (30–80 Hz) has also typically been associated with attention and perceptual success (Meador et al., 2002; Gonzalez Andino et al., 2005; Bauer et al., 2006), as have nonrhythmic baseline magnitudes (Martin et al., 2006). Analysis of state properties is an essential and extensive topic. As such, it was beyond the scope of the present report, which focused on poststimulus response dynamics, accurate biophysical modeling, and their relation to conscious perception.

References

Allison T, Goff WR, Williamson PD, VanGilder JC (1980) On the neural origin of early components of the human somatosensory evoked potential. In: Clinical uses of cerebral, brain-stem and spinal somatosensory evoked potentials. Progress in clinical neurophysiology (Desmedt JE, ed), pp 51–68. Basel: Karger.

Arezzo J, Legatt AD, Vaughan Jr HG (1979) Topography and intracranial sources of somatosensory evoked potentials in the monkey. I. Early components. Electroencephalogr Clin Neurophysiol 46:155–172.

Arezzo JC, Vaughan Jr HG, Legatt AD (1981) Topography and intracranial sources of somatosensory evoked potentials in the monkey. II. Cortical components. Electroencephalogr Clin Neurophysiol 51:1–18.

Bannister AP (2005) Inter- and intra-laminar connections of pyramidal cells in the neocortex. Neurosci Res 53:95–103.

Barth DS, Di S (1991) Laminar excitability cycles in neocortex. J Neurophysiol 65:891–898.

Bauer M, Oostenveld R, Peeters M, Fries P (2006) Tactile spatial attention enhances gamma-band activity in somatosensory cortex and reduces low-frequency activity in parieto-occipital areas. J Neurosci 26:490–501.

Bekkers JM (2000) Properties of voltage-gated potassium currents in nucleated patches from large layer 5 cortical pyramidal neurons of the rat. J Physiol (Lond) 525:593–609.

Bernardo KL, McCasland JS, Woolsey TA, Strominger RN (1990a) Local intra- and interlaminar connections in mouse barrel cortex. J Comp Neurol 291:231–255.

Bernardo KL, McCasland JS, Woolsey TA (1990b) Local axonal trajectories in mouse barrel cortex. Exp Brain Res 82:247–253.

Braun C, Haug M, Wiech K, Birbaumer N, Elbert T, Roberts LE (2002) Functional organization of primary somatosensory cortex depends on the focus of attention. NeuroImage 17:1451–1458.

Brenner D, Lipton J, Kaufman L, Williamson SJ (1978) Somatically evoked magnetic fields of the human brain. Science 199:81–83.

Bush PC, Sejnowski TJ (1993) Reduced compartmental models of neocortical pyramidal cells. J Neurosci Methods 46:159–166.

Castro-Alamancos MA, Connors BW (1996) Spatiotemporal properties of short-term plasticity sensorimotor thalamocortical pathways of the rat. J Neurosci 16:2767–2779.

Cauller LJ, Connors BW (1994) Synaptic physiology of horizontal afferents to layer I in slices of rat SI neocortex. J Neurosci 14:751–762.

Cauller LJ, Kulics AT (1991) The neural basis of the behaviorally relevant N1 component of the somatosensory-evoked potential in SI cortex of awake monkeys: evidence that backward cortical projections signal conscious touch sensation. Exp Brain Res 84:607–619.

Cauller LJ, Clancy B, Connors BW (1998) Backward cortical projections to primary somatosensory cortex in rats extend long horizontal axons in layer I. J Comp Neurol 390:297–310.

Crick F, Koch C (2003) A framework for consciousness. Nat Neurosci 6:119–126.

Dai H (1995) On measuring psychometric functions: a comparison of the constant-stimulus and adaptive up-down methods. J Acoust Soc Am 98:3135–3139.

Danckert J, Goodale MA (2000) A conscious route to unconscious vision. Curr Biol 10:R64–R67.

David O, Harrison L, Friston KJ (2005) Modelling event-related responses in the brain. NeuroImage 25:756–770.

David O, Kiebel SJ, Harrison LM, Mattout J, Kilner JM, Friston KJ (2006a) Dynamic causal modeling of evoked responses in EEG and MEG. NeuroImage 30:1255–1272.

David O, Kilner JM, Friston KJ (2006b) Mechanisms of evoked and induced responses in MEG/EEG. NeuroImage 31:1580–1591.

de Lafuente V, Romo R (2005) Neuronal correlates of subjective sensory experience. Nat Neurosci 8:1698–1703.

de Lafuente V, Romo R (2006) Neural correlate of subjective sensory experience gradually builds up across cortical areas. Proc Natl Acad Sci USA 103:14266–14271.

Desmedt JE (1988) Somatosensory evoked potentials. In: Human event-related potentials. EEG handbook (Picton TW, ed), pp 245–360. Amsterdam: Elsevier Science.

Deuchars J, West DC, Thomson AM (1994) Relationships between morphology and physiology of pyramid-pyramid single axon connections in rat neocortex in vitro. J Physiol (Lond) 478:423–435.

Di S, Baumgartner C, Barth DS (1990) Laminar analysis of extracellular field potentials in rat vibrissa/barrel cortex. J Neurophysiol 63:832–840.

Douglas RJ, Martin KA (2004) Neuronal circuits of the neocortex. Annu Rev Neurosci 27:419–451.

Douglas RJ, Martin KA, Whitteridge D (1991) An intracellular analysis of the visual responses of neurones in cat visual cortex. J Physiol (Lond) 440:659–696.

Drevets WC, Burton H, Videen TO, Snyder AZ, Simpson Jr JR, Raichle ME (1995) Blood flow changes in human somatosensory cortex during anticipated stimulation. Nature 373:249–252.

Druschky K, Kaltenhauser M, Hummel C, Druschky A, Huk WJ, Neundorfer

B, Stefan H (2003) Somatosensory evoked magnetic fields following passive movement compared with tactile stimulation of the index finger. Exp Brain Res 148:186–195.

Eimer M, Forster B (2003) Modulations of early somatosensory ERP components by transient and sustained spatial attention. Exp Brain Res 151:24–31.

Elston GN, Benavides-Piccione R, DeFelipe J (2001) The pyramidal cell in cognition: a comparative study in human and monkey. J Neurosci 21:RC163(1–5).

Ergenoglu T, Demiralp T, Bayraktaroglu Z, Ergen M, Beydagi H, Uresin Y (2004) Alpha rhythm of the EEG modulates visual detection performance in humans. Brain Res Cogn Brain Res 20:376–383.

Feldmeyer D, Lubke J, Silver RA, Sakmann B (2002) Synaptic connections between layer 4 spiny neurone-layer 2/3 pyramidal cell pairs in juvenile rat barrel cortex: physiology and anatomy of interlaminar signalling within a cortical column. J Physiol (Lond) 538:803–822.

Felleman DJ, Van Essen DC (1991) Distributed hierarchical processing in the primate cerebral cortex. Cereb Cortex 1:1–47.

Fischl B, Dale AM (2000) Measuring the thickness of the human cerebral cortex from magnetic resonance images. Proc Natl Acad Sci USA 97:11050–11055.

Forss N, Hari R, Salmelin R, Ahonen A, Hämäläinen M, Kajola M, Knuutila J, Simola J (1994a) Activation of the human posterior parietal cortex by median nerve stimulation. Exp Brain Res 99:309–315.

Forss N, Salmelin R, Hari R (1994b) Comparison of somatosensory evoked fields to airpuff and electric stimuli. Electroencephalogr Clin Neurophysiol 92:510–517.

Forss N, Merlet I, Vanni S, Hämäläinen M, Mauguiere F, Hari R (1996) Activation of human mesial cortex during somatosensory target detection task. Brain Res 734:229–235.

Freund TF, Magloczky Z, Soltesz I, Somogyi P (1986) Synaptic connections, axonal and dendritic patterns of neurons immunoreactive for cholecystokinin in the visual cortex of the cat. Neuroscience 19:1133–1159.

Friedman DP, Jones EG (1980) Focal projection of electrophysiologically defined groupings of thalamic cells on the monkey somatic sensory cortex. Brain Res 191:249–252.

Friedman DP, Jones EG, Burton H (1980) Representation pattern in the second somatic sensory area of the monkey cerebral cortex. J Comp Neurol 192:21–41.

Garabedian CE, Jones SR, Merzenich MM, Dale A, Moore CI (2003) Band-pass response properties of rat SI neurons. J Neurophysiol 90:1379–1391.

Garcia-Larrea L, Bastuji H, Mauguiere F (1991) Mapping study of somatosensory evoked potentials during selective spatial attention. Electroencephalogr Clin Neurophysiol 80:201–214.

Gardner EP, Hämäläinen HA, Warren S, Davis J, Young W (1984) Somatosensory evoked potentials (SEPs) and cortical single unit responses elicited by mechanical tactile stimuli in awake monkeys. Electroencephalogr Clin Neurophysiol 58:537–552.

Geyer S, Schleicher A, Zilles K (1997) The somatosensory cortex of human: cytoarchitecture and regional distributions of receptor-binding sites. NeuroImage 6:27–45.

Golmayo L, Nunez A, Zaborszky L (2003) Electrophysiological evidence for the existence of a posterior cortical-prefrontal-basal forebrain circuitry in modulating sensory responses in visual and somatosensory rat cortical areas. Neuroscience 119:597–609.

Gonzalez Andino SL, Michel CM, Thut G, Landis T, Grave de Peralta R (2005) Prediction of response speed by anticipatory high-frequency (gamma band) oscillations in the human brain. Hum Brain Mapp 24:50–58.

Guillery RW, Sherman SM (2002) Thalamic relay functions and their role in corticocortical communication: generalizations from the visual system. Neuron 33:163–175.

Hämäläinen M, Hari R, Ilmoniemi RJ, Knuutila J, Lounasmaa OV (1993) Magnetoencephalography—theory, instrumentation, and applications to noninvasive studies of the working human brain. Rev Mod Phys 65:413–497.

Hämäläinen MS, Sarvas J (1989) Realistic conductivity geometry model of the human head for interpretation of neuromagnetic data. IEEE Trans Biomed Eng 36:165–171.

Hari R, Forss N (1999) Magnetoencephalography in the study of human somatosensory cortical processing. Philos Trans R Soc Lond B Biol Sci 354:1145–1154.

Hari R, Aittoniemi K, Jarvinen ML, Katila T, Varpula T (1980) Auditory evoked transient and sustained magnetic fields of the human brain. Localization of neural generators. Exp Brain Res 40:237–240.

Hasselmo ME (1995) Neuromodulation and cortical function: modeling the physiological basis of behavior. Behav Brain Res 67:1–27.

Hoechstetter K, Rupp A, Meinck HM, Weckesser D, Bornfleth H, Stippich C, Berg P, Scherg M (2000) Magnetic source imaging of tactile input shows task-independent attention effects in SII. NeuroReport 11:2461–2465.

Hoechstetter K, Rupp A, Stancak A, Meinck HM, Stippich C, Berg P, Scherg M (2001) Interaction of tactile input in the human primary and secondary somatosensory cortex—a magnetoencephalographic study. NeuroImage 14:759–767.

Hsiao SS, O'Shaughnessy DM, Johnson KO (1993) Effects of selective attention on spatial form processing in monkey primary and secondary somatosensory cortex. J Neurophysiol 70:444–447.

Iguchi Y, Hoshi Y, Tanosaki M, Taira M, Hashimoto I (2005) Attention induces reciprocal activity in the human somatosensory cortex enhancing relevant- and suppressing irrelevant inputs from fingers. Clin Neurophysiol 116:1077–1087.

Ikeda H, Wang Y, Okada YC (2005) Origins of the somatic N20 and high-frequency oscillations evoked by trigeminal stimulation in the piglets. Clin Neurophysiol 116:827–841.

Jackson ME, Cauller LJ (1998) Neural activity in SII modifies sensory evoked potentials in SI in awake rats. NeuroReport 9:3379–3382.

Jones EG (1986) Connectivity of the primary sensory-motor cortex. In: Cerebral cortex. Sensory-motor areas and aspects of cortical connectivity, Ed 2 (Jones EG, Peters A, eds), pp 113–183. New York: Plenum.

Jones EG (1998) Viewpoint: the core and matrix of thalamic organization. Neuroscience 85:331–345.

Jones EG (2001) The thalamic matrix and thalamocortical synchrony. Trends Neurosci 24:595–601.

Jones SR, Pinto DJ, Kaper TJ, Kopell N (2000) Alpha-frequency rhythms desynchronize over long cortical distances: a modeling study. J Comput Neurosci 9:271–291.

Kaas JH, Garraghty PE (1991) Hierarchical, parallel, and serial arrangements of sensory cortical areas: connection patterns and functional aspects. Curr Opin Neurobiol 1:248–251.

Kakigi R, Hoshiyama M, Shimojo M, Naka D, Yamasaki H, Watanabe S, Xiang J, Maeda K, Lam K, Itomi K, Nakamura A (2000) The somatosensory evoked magnetic fields. Prog Neurobiol 61:495–523.

Kandel A, Buzsáki G (1997) Cellular-synaptic generation of sleep spindles, spike-and-wave discharges, and evoked thalamocortical responses in the neocortex of the rat. J Neurosci 17:6783–6797.

Karhu J, Tesche CD (1999) Simultaneous early processing of sensory input in human primary (SI) and secondary (SII) somatosensory cortices. J Neurophysiol 81:2017–2025.

Kisvarday ZF, Martin KA, Whitteridge D, Somogyi P (1985) Synaptic connections of intracellularly filled clutch cells: a type of small basket cell in the visual cortex of the cat. J Comp Neurol 241:111–137.

Koch C, Douglas R, Wehmeier U (1990) Visibility of synaptically induced conductance changes: theory and simulations of anatomically characterized cortical pyramidal cells. J Neurosci 10:1728–1744.

Korngreen A, Sakmann B (2000) Voltage-gated K+ channels in layer 5 neocortical pyramidal neurones from young rats: subtypes and gradients. J Physiol (Lond) 525:621–639.

Krupa DJ, Wiest MC, Shuler MG, Laubach M, Nicolelis MA (2004) Layer-specific somatosensory cortical activation during active tactile discrimination. Science 304:1989–1992.

Kulics AT (1982) Cortical neural evoked correlates of somatosensory stimulus detection in the rhesus monkey. Electroencephalogr Clin Neurophysiol 53:78–93.

Kulics AT, Cauller LJ (1986) Cerebral cortical somatosensory evoked responses, multiple unit activity and current source-densities: their interrelationships and significance to somatic sensation as revealed by stimulation of the awake monkey's hand. Exp Brain Res 62:46–60.

LaMotte RH, Mountcastle VB (1975) Capacities of humans and monkeys to discriminate vibratory stimuli of different frequency and amplitude: a correlation between neural events and psychological measurements. J Neurophysiol 38:539–559.

LaMotte RH, Mountcastle VB (1979) Disorders in somesthesis following lesions of parietal lobe. J Neurophysiol 42:400–419.

Lee L, Friston K, Horwitz B (2006) Large-scale neural models and dynamic causal modelling. NeuroImage 30:1243–1254.

Leek MR (2001) Adaptive procedures in psychophysical research. Percept Psychophys 63:1279–1292.

Linkenkaer-Hansen K, Nikulin VV, Palva S, Ilmoniemi RJ, Palva JM (2004) Prestimulus oscillations enhance psychophysical performance in humans. J Neurosci 24:10186–10190.

Lipton ML, Fu KM, Branch CA, Schroeder CE (2006) Ipsilateral hand input to area 3b revealed by converging hemodynamic and electrophysiological analyses in macaque monkeys. J Neurosci 26:180–185.

Lubke J, Markram H, Frotscher M, Sakmann B (1996) Frequency and dendritic distribution of autapses established by layer 5 pyramidal neurons in the developing rat neocortex: comparison with synaptic innervation of adjacent neurons of the same class. J Neurosci 16:3209–3218.

Mainen ZF, Sejnowski TJ (1996) Influence of dendritic structure on firing pattern in model neocortical neurons. Nature 382:363–366.

Martin T, Houck JM, Bish JP, Kicic D, Woodruff CC, Moses SN, Lee DC, Tesche CD (2006) MEG reveals different contributions of somatomotor cortex and cerebellum to simple reaction time after temporally structured cues. Hum Brain Mapp 27:552–561.

Mauguiere F, Merlet I, Forss N, Vanni S, Jousmaki V, Adeleine P, Hari R (1997a) Activation of a distributed somatosensory cortical network in the human brain. A dipole modelling study of magnetic fields evoked by median nerve stimulation. Part I: Location and activation timing of SEF sources. Electroencephalogr Clin Neurophysiol 104:281–289.

Mauguiere F, Merlet I, Forss N, Vanni S, Jousmaki V, Adeleine P, Hari R (1997b) Activation of a distributed somatosensory cortical network in the human brain: a dipole modelling study of magnetic fields evoked by median nerve stimulation. Part II: Effects of stimulus rate, attention and stimulus detection. Electroencephalogr Clin Neurophysiol 104:290–295.

McCormick DA (1992) Neurotransmitter actions in the thalamus and cerebral cortex and their role in neuromodulation of thalamocortical activity. Prog Neurobiol 39:337–388.

Meador KJ, Ray PG, Echauz JR, Loring DW, Vachtsevanos GJ (2002) Gamma coherence and conscious perception. Neurology 59:847–854.

Migliore M, Shepherd GM (2002) Emerging rules for the distributions of active dendritic conductances. Nat Rev Neurosci 3:362–370.

Moore CI, Nelson SB (1998) Spatio-temporal subthreshold receptive fields in the vibrissa representation of rat primary somatosensory cortex. J Neurophysiol 80:2882–2892.

Moore CI, Stern CE, Corkin S, Fischl B, Gray AC, Rosen BR, Dale AM (2000) Segregation of somatosensory activation in the human rolandic cortex using fMRI. J Neurophysiol 84:558–569.

Moore CI, Crosier E, Greve DN, Savoy R, Merzenich MM, Dale AM (2007) Cortical correlates of vibrotactile detection in humans. Cereb Cortex, in press.

Murakami S, Okada Y (2006) Contributions of principal neocortical neurons to magnetoencephalography and electroencephalography signals. J Physiol (Lond) 575:925–936.

Murakami S, Zhang T, Hirose A, Okada YC (2002) Physiological origins of evoked magnetic fields and extracellular field potentials produced by guinea-pig CA3 hippocampal slices. J Physiol (Lond) 544:237–251.

Murakami S, Hirose A, Okada YC (2003) Contribution of ionic currents to magnetoencephalography (MEG) and electroencephalography (EEG) signals generated by guinea-pig CA3 slices. J Physiol (Lond) 553:975–985.

Nicolelis MA, Fanselow EE (2002) Thalamocortical [correction of Thalamcortical] optimization of tactile processing according to behavioral state. Nat Neurosci 5:517–523.

Nishitani N, Hari R (2000) Temporal dynamics of cortical representation for action. Proc Natl Acad Sci USA 97:913–918.

Okada YC, Wu J, Kyuhou S (1997) Genesis of MEG signals in a mammalian CNS structure. Electroencephalogr Clin Neurophysiol 103:474–485.

Palva S, Linkenkaer-Hansen K, Naatanen R, Palva JM (2005) Early neural correlates of conscious somatosensory perception. J Neurosci 25:5248–5258.

Penfield W, Rasmusson T (1950) The cerebral cortex of man: a clinical study of localization and function. New York: Hafner.

Peterson NN, Schroeder CE, Arezzo JC (1995) Neural generators of early cortical somatosensory evoked potentials in the awake monkey. Electroencephalogr Clin Neurophysiol 96:248–260.

Pinto DJ, Jones SR, Kaper TJ, Kopell N (2003) Analysis of state-dependent transitions in frequency and long-distance coordination in a model oscillatory cortical circuit. J Comput Neurosci 15:283–298.

Ress D, Backus BT, Heeger DJ (2000) Activity in primary visual cortex predicts performance in a visual detection task. Nat Neurosci 3:940–945.

Riera JJ, Wan X, Jimenez JC, Kawashima R (2006) Nonlinear local electrovascular coupling. I: A theoretical model. Hum Brain Mapp 27:896–914.

Riera JJ, Jimenez JC, Wan X, Kawashima R, Ozaki T (2007) Nonlinear local electrovascular coupling. II: From data to neuronal masses. Hum Brain Mapp 28:335–354.

Rockland KS, Pandya DN (1979) Laminar origins and terminations of cortical connections of the occipital lobe in the rhesus monkey. Brain Res 179:3–20.

Sarter M, Parikh V (2005) Choline transporters, cholinergic transmission and cognition. Nat Rev Neurosci 6:48–56.

Sarvas J (1987) Basic mathematical and electromagnetic concepts of the biomagnetic inverse problem. Phys Med Biol 32:11–22.

Sastre-Janer FA, Regis J, Belin P, Mangin JF, Dormont D, Masure MC, Remy P, Frouin V, Samson Y (1998) Three-dimensional reconstruction of the human central sulcus reveals a morphological correlate of the hand area. Cereb Cortex 8:641–647.

Segev I, Rapp M, Manor Y, Yarom Y (1992) Analog and digital processing in single nerve cells: dendritic integration and axonal propagation. San Diego: Academic.

Sherman SM, Guillery RW (2002) The role of the thalamus in the flow of information to the cortex. Philos Trans R Soc Lond B Biol Sci 357:1695–1708.

Silva LR, Gutnick MJ, Connors BW (1991) Laminar distribution of neuronal membrane properties in neocortex of normal and reeler mouse. J Neurophysiol 66:2034–2040.

Somogyi P, Kisvarday ZF, Martin KA, Whitteridge D (1983) Synaptic connections of morphologically identified and physiologically characterized large basket cells in the striate cortex of cat. Neuroscience 10:261–294.

Staines WR, Graham SJ, Black SE, McIlroy WE (2002) Task-relevant modulation of contralateral and ipsilateral primary somatosensory cortex and the role of a prefrontal-cortical sensory gating system. NeuroImage 15:190–199.

Steinmetz PN, Roy A, Fitzgerald PJ, Hsiao SS, Johnson KO, Niebur E (2000) Attention modulates synchronized neuronal firing in primate somatosensory cortex. Nature 404:187–190.

Stoerig P (2006) Blindsight, conscious vision, and the role of primary visual cortex. Prog Brain Res 155:217–234.

Stuart GJ, Sakmann B (1994) Active propagation of somatic action potentials into neocortical pyramidal cell dendrites. Nature 367:69–72.

Tesche CD, Uusitalo MA, Ilmoniemi RJ, Huotilainen M, Kajola M, Salonen O (1995) Signal-space projections of MEG data characterize both distributed and well-localized neuronal sources. Electroencephalogr Clin Neurophysiol 95:189–200.

Thomson AM, Bannister AP (1998) Postsynaptic pyramidal target selection by descending layer III pyramidal axons: dual intracellular recordings and biocytin filling in slices of rat neocortex. Neuroscience 84:669–683.

Thomson AM, Bannister AP (2003) Interlaminar connections in the neocortex. Cereb Cortex 13:5–14.

Thomson AM, West DC, Wang Y, Bannister AP (2002) Synaptic connections and small circuits involving excitatory and inhibitory neurons in layers 2–5 of adult rat and cat neocortex: triple intracellular recordings and biocytin labelling in vitro. Cereb Cortex 12:936–953.

Towe AL (1966) On the nature of the primary evoked response. Exp Neurol 15:113–139.

Uematsu S, Lesser RP, Gordon B (1992) Localization of sensorimotor cortex: the influence of Sherrington and Cushing on the modern concept. Neurosurgery 30:904–912; discussion 912–903.

Uusitalo MA, Ilmoniemi RJ (1997) Signal-space projection method for separating MEG or EEG into components. Med Biol Eng Comput 35:135–140.

White LE, Andrews TJ, Hulette C, Richards A, Groelle M, Paydarfar J, Purves D (1997) Structure of the human sensorimotor system. I: Morphology and cytoarchitecture of the central sulcus. Cereb Cortex 7:18–30.

Worden MS, Foxe JJ, Wang N, Simpson GV (2000) Anticipatory biasing of visuospatial attention indexed by retinotopically specific alpha-band electroencephalography increases over occipital cortex. J Neurosci 20:RC63(1–6).

Yousry TA, Schmid UD, Alkadhi H, Schmidt D, Peraud A, Buettner A, Winkler P (1997) Localization of the motor hand area to a knob on the precentral gyrus. A new landmark. Brain 120:141–157.

Yu AJ, Dayan P (2005) Uncertainty, neuromodulation, and attention. Neuron 46:681–692.

Zhu JJ, Connors BW (1999) Intrinsic firing patterns and whisker-evoked synaptic responses of neurons in the rat barrel cortex. J Neurophysiol 81:1171–1183.

J Neurophysiol 102: 3554–3572, 2009.
First published October 7, 2009; doi:10.1152/jn.00535.2009.

Quantitative Analysis and Biophysically Realistic Neural Modeling of the MEG Mu Rhythm: Rhythmogenesis and Modulation of Sensory-Evoked Responses

Stephanie R. Jones,[1] Dominique L. Pritchett,[2] Michael A. Sikora,[1] Steven M. Stufflebeam,[1] Matti Hämäläinen,[1] and Christopher I. Moore[1,2]

[1]*Athinoula A. Martinos Center For Biomedical Imaging, Massachusetts General Hospital, Charlestown; and* [2]*McGovern Institute for Brain Research, Massachusetts Institute of Technology, Cambridge, Massachusetts*

Submitted 17 June 2009; accepted in final form 3 October 2009

Jones SR, Pritchett DL, Sikora MA, Stufflebeam SM, Hämäläinen M, Moore CI. Quantitative analysis and biophysically realistic neural modeling of the MEG mu rhythm: rhythmogenesis and modulation of sensory-evoked responses. *J Neurophysiol* 102: 3554–3572, 2009. First published October 7, 2009; doi:10.1152/jn.00535.2009. Variations in cortical oscillations in the alpha (7–14 Hz) and beta (15–29 Hz) range have been correlated with attention, working memory, and stimulus detection. The mu rhythm recorded with magnetoencephalography (MEG) is a prominent oscillation generated by Rolandic cortex containing alpha and beta bands. Despite its prominence, the neural mechanisms regulating mu are unknown. We characterized the ongoing MEG mu rhythm from a localized source in the finger representation of primary somatosensory (SI) cortex. Subjects showed variation in the relative expression of mu-alpha or mu-beta, which were nonoverlapping for roughly 50% of their respective durations on single trials. To delineate the origins of this rhythm, a biophysically principled computational neural model of SI was developed, with distinct laminae, inhibitory and excitatory neurons, and feedforward (FF, representative of lemniscal thalamic drive) and feedback (FB, representative of higher-order cortical drive or input from nonlemniscal thalamic nuclei) inputs defined by the laminar location of their postsynaptic effects. The mu-alpha component was accurately modeled by rhythmic FF input at approximately 10-Hz. The mu-beta component was accurately modeled by the addition of approximately 10-Hz FB input that was nearly synchronous with the FF input. The relative dominance of these two frequencies depended on the delay between FF and FB drives, their relative input strengths, and stochastic changes in these variables. The model also reproduced key features of the impact of high prestimulus mu power on peaks in SI-evoked activity. For stimuli presented during high mu power, the model predicted enhancement in an initial evoked peak and decreased subsequent deflections. In agreement, the MEG-evoked responses showed an enhanced initial peak and a trend to smaller subsequent peaks. These data provide new information on the dynamics of the mu rhythm in humans and the model provides a novel mechanistic interpretation of this rhythm and its functional significance.

INTRODUCTION

Two predominant rhythms are expressed in the neocortex in the frequency range from 7 to 30 Hz: alpha (7–14 Hz) and beta (15–29 Hz). Modulation of alpha and beta activity is correlated with successful perception in humans and awake monkeys (Bauer et al. 2006; Donner et al. 2007; Hanslmayr et al. 2007; Linkenkaer-Hansen et al. 2004; Mathewson et al. 2009; Mazaheri et al. 2009; Palva et al. 2005b; Pineda 2005; Schroeder and Lakatos 2009a; Schubert et al. 2008; van Wijk et al. 2009; Wilke et al. 2006; Worden et al. 2000; Zhang and Ding 2009). Recent studies have emphasized a potential role for the active deployment of these rhythms in the suppression of "distracting" sensory input (Jensen et al. 2002; Kelly et al. 2006; Mazaheri et al. 2009; Worden et al. 2000), presumably by suppression of evoked responses in early sensory cortices.

The mu rhythm measured with magnetoencephalography (MEG) over Rolandic cortex shows alpha and beta components (Hari and Salmelin 1997; Tiihonen et al. 1989). This finding is in contrast to the Rolandic mu rhythm measured with electroencephalography (EEG), in which only a dominant alpha component is typically observed (Kuhlman 1978; Zhang and Ding 2009). This historical distinction is likely attributable to differences in the recording techniques and has led to mixed usage of the term "mu" in the literature. This ambiguity in naming is indicative of the ongoing ambiguity with respect to the statistical characteristics and neural origins of the mu rhythm. Despite the fact that much research has been devoted to localizing the source of this rhythm in the brain—and to understanding the cellular-level neural mechanisms creating alpha and beta rhythms independently—the neural origin of the MEG mu complex remains unknown. In the present report, we investigated the two-component mu rhythm measured with MEG using experimental and modeling approaches. We refer to these components throughout as *mu-alpha* and *mu-beta*.

One prominent view of the origin of the MEG mu rhythm, based on source localization of sensor data from human studies, is that the mu-beta component is produced by the precentral motor cortex, whereas the mu-alpha component originates from the postcentral somatosensory cortex (Hari and Salmelin 1997; Salmelin and Hari 1994; Salmelin et al. 1995). These studies focused on localizing late event-related desynchronization (ERD) of the rhythm after movement. More recent work, focused on spontaneous activity and early ERD, has shown that both components can be expressed in a single area (Brovelli et al. 2004; Gaetz and Cheyne 2006; Kopell et al. 2000; Pinto et al. 2003; Szurhaj et al. 2003), with intracerebral recordings in humans suggesting a common source in primary somatosensory (SI) cortex (Szurhaj et al. 2003).

Studies that have investigated the cellular-level neural mechanisms inducing ongoing cortical alpha and beta rhythms have focused on the origin of the two frequency bands separately. A

Address for reprint requests and other correspondence: S. R. Jones, Mass General Hospital, Athinoula A. Martinos Center for Biomedical Imaging, 149 13th Street, Suite 2301, Charlestown, MA 02129 (E-mail: srjones@nmr.mgh.harvard.edu).

large body of experimental and computational work suggests neocortical alpha emerges from an approximately 10-Hz thalamocortical rhythm (Andersen and Andersson 1968; Contreras and Steriade 1995; Hughes and Crunelli 2005; Suffczynski et al. 2001; Traub et al. 2005). Other evidence suggests that neocortical alpha also depends on, or could emerge independently from, intrinsic properties in large layer V pyramidal neurons (Bollimunta et al. 2008; Jones et al. 2000; Pinto et al. 2003; Silva et al. 1991) and/or the local activity of low-threshold spiking interneurons (Fanselow et al. 2008).

Fewer studies of the neural origins of the cortical beta rhythm have been conducted. Slice recordings (Roopun et al. 2006; Whittington et al. 2000) and computational models (Jensen et al. 2002; Kopell et al. 2000; Pinto et al. 2003; Roopun et al. 2006) have shown a beta-frequency range oscillation in isolated cortex that depends on the kinetics of the M-type potassium current in excitatory neurons, combined with GABAergic inhibition. Roopun et al. (2006) further found that axonal gap junctions were critical to the maintenance of pharmacologically induced 20- to 30-Hz rhythms in slices from somatosensory cortex (referred to as a "beta 2" rhythm) and that lower-frequency beta rhythms (13–17 Hz; "beta 1") could be produced by period concatenation of higher-frequency beta (20–30 Hz) and gamma (30–50 Hz) oscillations (Kramer et al. 2008; Roopun et al. 2008). In all of these studies, the beta rhythm is argued to emerge from the activity of localized cells in a single cortical circuit that are spiking nearly synchronously and that the frequency of these rhythms depends on intrinsic membrane time constants.

Another body of research has suggested that beta activity mediates long-range communication between cortical areas, suggesting that intracortical projections may play a role in local beta expression (Buschman and Miller 2007; Hanslmayr et al. 2007; Roelfsema et al. 1997; Schubert et al. 2008; von Stein et al. 2000; Witham et al. 2007). For example, Von Stein et al. (2000) found coherence in beta-band activity between temporal and parietal EEG sensors during multimodel object representation in humans, and Buschman and Miller (2007) between parietal and frontal indwelling electrodes during selective attention in monkeys. In support for a role of interareal projections in the neocortex, Whitham et al. (2007) found interactions between 20-Hz activity in somatosensory and motor areas that did not depend on intrinsic spiking (Witham and Baker 2007) and claimed there was oscillatory coupling across the central sulcus. Brovelli et al. (2004) applied Granger causality analysis to 20-Hz oscillatory activity measured intracranially from multiple cortical sites in the monkey and claimed that the beta activity propagated from the primary somatosensory (SI) cortex to primary motor and parietal cortices. Nonlemniscal thalamic nuclei have also been proposed as relays for signal transmission between neocortical areas (Sherman 2005). Such thalamic nuclei are also ideally poised to generate oscillatory coherence across multiple cortical areas (Llinás and Ribary 2001). As such, beta activity related to long-range communication could also arise, at least in part, from these projections.

Difficulty establishing the neural mechanisms generating the MEG mu rhythm comes in part from the fact that the shared temporal dynamics of the mu-alpha and mu-beta components are not well characterized. Tiihonen et al. (1989) observed qualitatively that the mu-alpha and mu-beta components do not always overlap in time, suggesting they are not harmonics, but did not quantify this assertion (Palva et al. 2005b; Tiihonen et al. 1989). Evidence for cross-frequency coupling of these components has also been reported (Palva et al. 2005b). Quantifying the degree to which mu-alpha and mu-beta co-occur and covary in amplitude is crucial to understanding their relative interdependence and to constraining computational models of their origins.

An important related topic is delineation of the mechanistic underpinnings of the impact of ongoing mu power on evoked sensory responses. This relation is particularly important, given studies showing that both ongoing mu power and SI tactile-evoked responses predict perception (Jones et al. 2007; Kulics 1982; Linkenkaer-Hansen et al. 2004; Zhang and Ding 2009). In recent studies of mu-alpha, prestimulus power shows an inverted U-shaped relation to tactile detection (Linkenkaer-Hansen et al. 2004; Zhang and Ding 2009) and a similar relationship was seen for mu-beta (Linkenkaer-Hansen et al. 2004). In studies of the relationship between time-domain peaks in tactile-evoked responses and detection, Kulics (1982) observed that greater evoked activity in the local field potential (LFP) near 70 ms predicted detection of tactile input by monkeys with electrodes implanted in SI and that differences in later activity (105–130 ms) were correlated with reaction time. Similarly, in humans, Jones et al. (2007) showed that greater amplitude of components of the SI-evoked response 70–130 ms poststimulus was a key predictor of detection. Zhang and Ding (2009) recorded greater late evoked components (~140 ms) in sensorimotor EEG electrodes on successfully detected trials and Palva et al. (2005) showed greater response 30–150 ms poststimulus for detection in sensorimotor MEG sensors.

Despite the links between prestimulus mu expression or evoked response amplitude and detection, the impact of spontaneous mu on peaks in the time-domain tactile-evoked response (ER) has received limited attention. Nikouline et al. (2000) reported that large variation in the prestimulus mu-alpha band activity was related to "relatively stable" early parts ($\leq$60 ms; referred to as P35 and P60) of median nerve ERs recorded using MEG, which showed a small positive correlation with greater alpha power predicting a larger early component (Nikouline et al. 2000). Zhang and Ding (2009) reported that for late components (~140 ms) of the tactile ER measured with EEG, there was a complex and largely parabolic relationship between mu-alpha power and evoked amplitude (Zhang and Ding 2009). Further, although mechanisms for changes in later (>250 ms) components of median nerve (Nikulin et al. 2007) and visual (Mazaheri and Jensen 2008) evoked responses have been associated with baseline shifts and phase resetting of alpha activity (Hanslmayr et al. 2007; Makeig et al. 2002), to our knowledge no systematic study has been performed to delineate the specific impact of MEG mu power (containing alpha and beta components) on different aspects of the earlier tactile responses that have been linked to perceptual success.

To investigate these questions, we recorded whole-head 306-channel MEG data and applied an equivalent current dipole inverse solution technique to look at activity from the hand area of SI, a technique that has been found to consistently localize signals discretely to the anterior bank of the postcentral gyrus, area 3b (Jones et al. 2007). We studied the prestimulus mu rhythm generated by this somatosensory source and its

connection to peaks in the early (<175 ms) time-domain–evoked responses. On single trials, we observed that during the prestimulus time period high-power epochs of mu-alpha and mu-beta were not simultaneous in their emergence, but did co-occur at rates greater than chance. These findings suggest that mu-alpha and mu-beta emerge from separable generators within SI that share common elements. We did not explore evoked poststimulus oscillations because our analysis of this period was focused on the region in which our model had predictive power in the evoked response (0–175 ms).

We then implemented a biophysically principled laminar cortical model of SI to make specific predictions with respect to the underlying neural mechanisms inducing the mu rhythm, its modulations in prestimulus power, and their influence on early peaks (<175 ms) in the time-domain tactile-evoked response. This model was expanded from our previous SI model that accurately reproduced the different time-domain–evoked response components in SI measured with MEG. The model included pyramidal neurons and interneurons in the supra- and infragranular layers. Importantly, this model also included thalamocortical feedforward (FF) input and inputs to distal dendrites that could arise from intracortical feedback (FB) or from nonlemniscal thalamic input.

Our results showed that the mutual generation of the mu-alpha and mu-beta components of the prestimulus rhythm, as well as the relative separation of these components in time, can be reproduced by the SI model. The data and model indicated these rhythms are not simple harmonics and are not regulated by time constants of intrinsic membrane properties. The mu-alpha component was reproduced with an approximately 10-Hz stochastic thalamocortical FF input. Accurately capturing mu-beta and its interactions with mu-alpha, in contrast to previous modeling studies emphasizing local cortical circuits and intrinsic properties, required rhythmic supragranular input, consistent with FB from higher cortical areas and/or input from nonlemniscal thalamic sources. To accurately reproduce the observed mu-alpha and mu-beta emergence and statistical interdependence, this FB was simulated not as a 20-Hz signal, but rather as a stochastic approximately 10-Hz signal. Further, mu-beta was not achieved when the approximately 10-Hz supragranular inputs were perfectly out of phase, as one might expect for generation of a 20-Hz oscillation, but rather almost perfectly aligned with the approximately 10-Hz FF input (<10-ms mean delay).

Investigation of the influence of prestimulus mu rhythm on the gain of the early-evoked sensory response (0–175 ms) in the model showed that mu power had a dominant effect on the initial peaks of the time-domain signal (<70 ms). This prediction was confirmed in the MEG data. Further, the model predicted that a key impact of high mu on peaks of the early evoked response is enhanced recruitment of excitatory and inhibitory interneurons and that recruitment of the interneurons caused suppression of subsequent (70–100 ms) components.

METHODS

MEG experiment

MEG data were collected from 10 neurologically healthy, right-handed, 18- to 45-yr-old adults during performance of a tactile-detection paradigm. The experimental protocol was approved by the Massachusetts General Hospital Internal Review Board and each subject gave informed consent prior to data acquisition. The stimulus paradigm and data acquisition are described in detail in Jones et al. (2007), which reported on tactile-evoked response components for 7 of these subjects; data from an additional 3 subjects were collected for the present report. Here, we outline key aspects of the experimental paradigm and current data analysis methods.

STIMULUS PARADIGM. Brief taps were delivered to the subject's right hand in the form of a single cycle of a 100-Hz sine wave (10-ms duration) via a custom piezoelectric device. Subjects rested their hand on a Delrin frame that held a piezoelectric transducer parallel to the finger (Noliac ceramic multilayer bender plate: $32 \times 7.8 \times 1.88$ mm). A deflection stroke drove a 7-mm-diameter Delrin contractor through a 1-cm circular rigid surround and into the fingertip.

The detection threshold of each subject was obtained prior to imaging using a parameter estimation by sequential testing (PEST) convergence procedure (Dai 1995; Leek 2001). During MEG recordings, for 70% of presented trials, stimulus strength was maintained at a perceptual threshold level (50% detection) using a dynamic algorithm (see Jones et al. 2007). Suprathreshold stimuli (10% of all trials; 350-μm deflection; 100% detection) and null trials (20%) were randomly interleaved with the threshold stimuli. Trial duration was 3 s. Each subject underwent eight runs with 120 trials. Trial onset was indicated by a 60-dB, 2-kHz auditory cue delivered to both ears for 2 s. During the auditory cue, the 10-ms finger-tap stimulus was delivered between 500 and 1,500 ms, in 100-ms intervals, from trial onset. The number of trials of a given latency to tap was randomly distributed during each run. Following the cessation of the auditory cue, subjects reported detection or nondetection of the stimulus with button presses, using the second or third digit of the left hand, respectively. The auditory cue ended ≥500 ms after the tactile stimulus and 1,000 ms before the next trial began.

MEG DATA ACQUISITION. By use of a 306-channel MEG (Elekta-Neuromag Vectorview), neuromagnetic responses were recorded with 306 sensors arranged in triplets of two planar gradiometers and a magnetometer at 102 sites. In addition to MEG, the vertical and horizontal electrooculogram (EOG) signals were recorded with electrodes placed close to the left eye. Four head-position indicator (HPI) coils were placed on the subject's head to coregister the subject's anatomical magnetic resonance image (MRI) and the MEG sensors. The data were sampled at 600 Hz with the band-pass set to 0.01–200 Hz. The responses were averaged on-line for quality control. In the off-line analysis, the data were reaveraged using a band-pass of 0.1–200 Hz. The chosen high-pass filter corner frequency was low enough to retain possible slow variations in the dc level of the neural signals while eliminating low-frequency environmental noise. Inspection of the localized SI spontaneous activity (see description of source analysis in the following text) showed that it was stable through ≥10-s time windows during which there was modulation of the mu rhythm without dc offset. Epochs with EOG peak-to-peak amplitude exceeding 150 μV were excluded from the analysis.

MEG SOURCE ANALYSIS. Source analysis was used to locate the primary current-dipole source to contralateral SI and to find the time course of this source, taking into account the presence of other active areas. This method was motivated by and described in greater detail in Jones et al. (2007), but is also described here. The SI contribution to the somatosensory-evoked field was isolated using the following approach. Because we did not observe consistent activity over the ipsilateral secondary somatosensory cortex (SII), or in other brain areas, we modeled the data with two dipoles (contralateral SI and SII). This fit was then optimized by use of signal-space projection (SSP) (Tesche et al. 1995; Uusitalo and Ilmoniemi 1997). A least-squares fit with the dipole forward solution was calculated through the use of a spherically symmetric conductor model (Hamalainen and Sarvas 1989; Sarvas 1987). At the peak activity in the suprathreshold stimulus signals from one data run (average of 12 trials; mean = 68 ms,

SD = 8 ms), we observed an initial equivalent current dipole (ECD). An anatomical MRI was then coregistered with the MEG, confirming this source localized to SI in 7 of 10 subjects. We then removed the contribution of the SI ECD using the SSP method and the residual data fit with a second ECD (Nishitani and Hari 2000; Tesche et al. 1995; Uusitalo and Ilmoniemi 1997). In all fit data during peak responses, the goodness-of-fit of the two-dipole model was >70%. We then removed the effect of the second ECD from the data using SSP and refitted the SI ECD to the residual. The ECD localizations fitted to the suprathreshold data were used to model all responses. Only the last 100 trials for a given response were considered for analysis, to account for adaptation and learning effects with training.

Large baseline rhythmic activity interfered with the localization of peak responses for 2 of the 10 subjects. In these cases, the SI source was placed in the finger representation of area 3b within the anterior bank of the postcentral gyrus (Moore et al. 2000; Penfield and Rasmussen 1950; Sastre-Janer et al. 1998; Uematsu et al. 1992; White et al. 1997; Yousry et al. 1997) and the SII dipole source was placed in the parietal operculum. For one of the 10 subjects, anatomical MRI data could not be obtained. In this case, SI dipole localization was determined by field contours on the spherical head model, consistent with the predicted position of contralateral SI. Removal of these 3 subjects from our analysis did not have a significant impact on our results (see Fig. 3).

FREQUENCY DOMAIN ANALYSIS. Power spectral density (PSD) analyses (Figs. 3*A* and 7*A*) were calculated for frequencies from 1 to 60 Hz using the Welch's periodogram method as implemented in Matlab, with overlapping 0.5-s windows.

Time–frequency representations (TFRs) or spectrograms of the data were calculated from 1 to 40 Hz on the SI ECD time courses by convolving the signals with a complex Morlet wavelet of the form $w(t, f_0) = A \exp(-t^2/2\sigma_t^2) \exp(2i\pi f_0 t)$, for each frequency of interest f_0, where $\sigma_t = m/2\pi f_0$ and i is the imaginary unit. The normalization factor was $A = 1/(\sigma_t\sqrt{2\pi})$ and the constant m, defining the compromise between time and frequency resolution, was 7. TFRs of power were calculated as the squared magnitude of the complex wavelet-transformed data. The normalization factor used is such that the sum of the magnitude of the wavelet coefficients over all frequencies is one, unlike that preserving the sum of squared magnitudes of the wavelet coefficients used in, e.g., Tallon-Baudry et al. (1997). Our normalization factor emphasizes higher frequencies with the distinct benefit of allowing us to more clearly visualize the time course of 15- to 29-Hz mu-beta activity (e.g., compare Fig. 3, *A* and *C*). Therefore the low-frequency activity (<7 Hz) is much less pronounced than that in the traditional PSD plots.

POWER SORTING ALGORITHM. When sorting trials over mu (7–29 Hz), mu-alpha (7–14 Hz), or mu-beta (15–29 Hz) power for analysis in Figs. 5, 7, and 9*B*, spectrograms (described earlier) calculated for each trial were averaged over the frequency band of interest and then sorted from high to low power. The top and bottom 10% of the sorted trials were excluded from further analysis.

CALCULATION OF SYMMETRY INDEX. The symmetry index of the oscillation waveform around zero, as shown in Fig. 6, was calculated as follows. We first applied a band-pass of the entire mu frequency range (7–29 Hz) to the signal. We then found the local maxima (peaks) and minima (troughs) in the filtered data and identified the time points corresponding to each peak and trough. These time points were used to obtain signal peak and trough values from the unfiltered data. The symmetry index (SInd) was calculated as [abs (peak) − abs (trough)]/[abs (peak) + abs (trough)] (Galaburda et al. 1990). A positive symmetry index indicates greater-amplitude peaks, a negative value indicates greater-amplitude troughs, and a zero value indicates that an oscillation was symmetric around zero.

Computational neural model

The computational neural modeling presented is expanded from our previous model of a laminar SI network, as described in detail in Jones et al. (2007) and the code is available to the public on the NEURON ModelDB website (http://senselab.med.yale.edu/modeldb/ShowModel.asp?model=113732). Here, we describe key features of the model and its expansion.

SI CORTICAL COLUMN MODEL. Our simulated SI cortical column network consisted of 100 multiple-compartment excitatory pyramidal neurons (PNs) and 35 single-compartment inhibitory interneurons (INs) per layer (Thomson et al. 2002) in layers II/III and V, expanded from 10 PNs and 3 PNs in each layer in our previous model (Jones et al. 2007). Postsynaptic dendritic contact points of the local excitatory and inhibitory synapses are depicted in Fig. 1*A* (see Jones et al. 2007 for supporting literature). Connection lines are schematic representations of axonal-to-dendritic input. Axons were not explicitly modeled. The PNs were arranged in a two-dimensional (2D) grid as shown in Fig. 1*D*. INs were interleaved evenly between every 2 PNs (not shown in Fig. 1*D*). Fast and slow excitatory (α-amino-3-hydroxy-5-methyl-4-isoxazolepropionic acid/*N*-methyl-D-aspartate [AMPA/NMDA]) and inhibitory (γ-aminobutyric acid type A/type B [$GABA_A$/$GABA_B$]) synapses were simulated using an alpha function that was "turned on" by the soma of the presynaptic cell crossing a voltage threshold (mV = 0). The synaptic dynamics were defined by

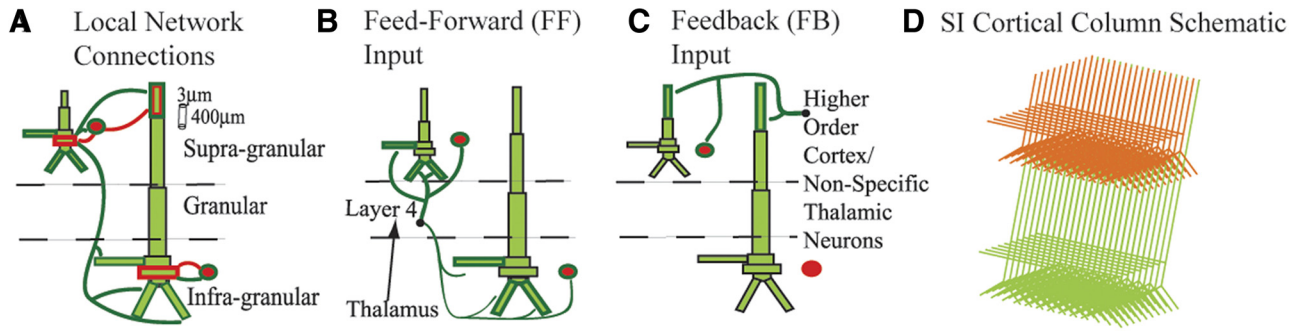

FIG. 1. Schematic of primary somatosensory cortex (SI) computational model network architecture. *A*: local network synaptic connections between multiple-compartment pyramidal neurons (PNs, green) and single-compartment inhibitory neurons (INs, red). Bold outlined dendrites were contacted. Within-layer PN-to-PN synapses (not shown) were also present on dark green outlined dendrites. *B*: excitatory feedforward (FF) input connections. The black arrow is only schematic because lemniscal thalamic input was not explicitly modeled. *C*: excitatory feedback (FB) input connections from presumed higher-order cortical and/or nonspecific thalamic neurons. The FF and FB inputs were modeled as spike train generators with a predetermined temporal profile and synaptic strength. *D*: schematic of expanded SI cortical column model containing a 2-dimensional grid of 100 PNs and 35 INs evenly spaced between every 2 PNs, in the supra- (PNs shown in orange) and infragranular layers (PNs shown in green); INs not shown. Each set of synaptic weights had a Gaussian spatial profile (Table 1).

the following rise/decay time constants and reversal potentials, respectively: AMPA 0.5/5 ms, 0 mV; NMDA 1/20 ms, 0 mV; $GABA_A$ 0.5/5 ms, −80 mV; $GABA_B$ 1/20 ms, −80 mV. The conductance of the synaptic connections within the local network grid were defined with a symmetric 2D Gaussian spatial profile, with a delay incorporated into the synaptic connection between two cells defined by an inverse Gaussian (Jones 1986; Kaas and Garraghty 1991). The maximum synaptic conductances and Gaussian weight space constants (WSCs, number of cells from center) are listed in Table 1 along with the minimum synaptic delay and corresponding Gaussian delay space constant (DSC).

SINGLE-CELL MORPHOLOGY AND PHYSIOLOGY. The morphology and physiology of the INs in each layer were simulated with single compartments and contained fast sodium (I_{Na}) and potassium currents (I_{Kdr}) to create spiking activity. The PNs in layers II/III and V were simulated with eight and nine segments, respectively, based on the reduction by Bush and Sejnowski (1993), and used a compartment length of 50 microns. The PNs in layer II/III produced an adapting spike trains to injected current created by active currents in the somatic and dendritic compartments, including a fast sodium current (I_{Na}), a delayed rectifier potassium current (I_{Kdr}), an adapting potassium current (I_M), and a leak current (I_L). The layer V PNs produced bursting responses to injected current (Fig. 1*B*) and contained the same currents as those of the PNs in layer II/III, with the addition of a calcium current (I_{Ca}), a potassium-activated calcium current (I_{KCa}), and h- and T-currents in the somatic and dendritic compartments. See Fig. 1*B* in Jones et al. (2007) for examples of spiking behavior. A low-threshold calcium current (I_T) and a hyperpolarization-activated mixed cation current (I_h) are additions to our previous model. The I_T channel density was constant in all segments at 2×10^{-4} S/cm^2. The I_h channel density was increased exponentially from the soma (where it was set at 1×10^{-6} S/cm^2) to apical dendrite, with a space constant of 3×10^{-3}. This matches I_h densities observed in rat somatosensory cortex (Kole et al. 2006). For further details, supporting literature, and specific parameters see Jones et al. (2007) and the web-available code at http://senselab.med.yale.edu/modeldb/ShowModel.asp?model=113732.

SYNAPTIC ARCHITECTURE OF EXOGENOUS DRIVE TO SI. Exogenous drives to the local network were simulated to reproduce *1*) ongoing mu rhythms and *2*) evoked responses in the model. In each case, the exogenous drive was excitatory only (Cauller and Connors 1994; Cauller et al. 1998; Guillery and Sherman 2002) and was defined by the laminar location in SI of its synaptic effects based on general principles of cortical circuitry (Douglas and Martin 2004; Felleman and Van Essen 1991; Friedman and Jones 1980; Jones 2001; Rockland and Pandya 1979). The sources of SI drive were modeled as spike generators with predefined temporal profiles and postsynaptic conductances that were distinct for the activity of ongoing rhythmic and evoked responses (described in the following text).

TABLE 1. *Local network synaptic connection parameters*

Parameter	Maximal Conductance, μS AMPA/NMDA or $GABA_A/GABA_B$	WSC	Minimum Synaptic Delay, ms	DSC
L2/3e to L2/3e	0.0005/0.0005	3	1	3
L2/3e to L2/3i	0.0005	3	1	3
L2/3e to L5e	0.00025	3	1	3
L2/3e to L5i	0.00025	3	1	3
L2/3i to L2e	0.05/0.05	50	1	50
L2/3i to L5e	0.001	50	1	50
L2/3i to L2/3i	0.02	20	1	20
L5e to L5e	0.005/0.0005	3	1	3
L5e to L5i	0.0005	3	1	3
L5i to L5e	0.025/0.025	70	1	70
L5i to L5i	0.02	20	1	20

Targeted dendritic compartments are outlined in Fig. 1*A*. e, excitatory; i, inhibitory; WSC, weight space constant; DSC, delay space constant.

Feedforward (FF) drive emerged from the granular layer, layer IV, and contacted the supragranular L2/3 neurons, with a delayed and weaker connection to the infragranular layer V neurons (see Fig. 1*B* for specific poststimulus dendritic compartments). Activity in layer IV is modeled to reflect drive from the thalamus based on several studies of intracranial laminar electrophysiological recordings of evoked responses in SI, including responses to vibrissa and thalamic stimuli in rodents (Barth and Di 1991; Castro-Alamancos and Connors 1996; Di et al. 1990; Douglas and Martin 2004; Kandel and Buzsáki 1997), trigeminal stimulation in piglets (Ikeda et al. 2005), and to tactile (Cauller and Kulics 1991; Kulics and Cauller 1986) and median nerve stimuli in awake monkeys (Lipton et al. 2006; Peterson et al. 1995). The maximal conductances onto INs were always twice as strong as those onto PNs for all FF inputs (Giove et al. 2003). In our previous study, this FF drive was referred to as "granular layer output." For descriptive purposes, we have changed the nomenclature in the current study.

Feedback (FB) drive to the SI network contacted the distal apical dendrites in the supragranular layers of each neural population (Fig. 1*C*). This connection was representative of input from higher-order cortical areas or nonspecific thalamic sources (Douglas and Martin 2004; Felleman and Van Essen 1991; Friedman et al. 1980; Jackson and Cauller 1998; Jones 2001; Rockland and Pandya 1979). In our previous study, this FB drive was referred to as "supragranular layer input."

Temporal dynamics and conductances of ongoing and evoked exogenous drive to SI

Stochastic ongoing rhythmic drive (Fig. 2) was generated by delivering 10 "burst" spike trains, each consisting of two spikes with an interstimulus interval (ISI) of 10 ms, which was set based on experimental evidence (Hughes and Crunelli 2005), to the SI network in an FF synaptic activation pattern (Fig. 1*C*). To reproduce approximately 10-Hz input, all 10 bursts arrived nominally every 100 ms, with a Gaussian random distribution in arrival time for each burst (mean ISI of 100 ms; default variance of 400 ms). On every cycle, a similar input pattern (same number of bursts and arrival time statistics) arrived to the SI network in an FB synaptic activation pattern (Fig. 1*D*), delayed from the FF input by a fixed amount. This driving sequence is shown schematically in Fig. 2. The mean delay between the approximately 10-Hz FF and FB ongoing inputs, the number of prestimulus "bursts"/spike trains on each cycle (i.e., the "amplitude" of the input), the SD of the arrival time of each burst to the SI network (i.e., the "variance" of the input), and the maximal postsynaptic conductance of the inputs were varied parametrically to investigate their separate influence on an expressed mu rhythm (Fig. 8).

Stochastic events in each simulation were regulated by the arrival time of each of the input bursts, for both FF and FB inputs. On each cycle of the rhythmic input, the timing of each two-spike burst event (Fig. 2) was chosen from a Gaussian distribution, with mean fixed at 100-ms intervals (e.g., 0, 100, 200 ms, etc.) and variance of 400 ms. With this mechanism, on every cycle the relative net postsynaptic conductance of the FF and FB drives changed. All other parameters were fixed for each simulation with default values of delay = 5 ms, number of input bursts = 10, variance of input bursts = 400 ms. The default conductances for FF and FB inputs were as follows: low mu, maximal weight of 0.4 picosiemens (pS) onto PNs and 0.8 pS onto INs; high mu, maximal weight of 0.6 pS onto PNs and 1.2 pS onto INs. Synaptic weights and delays were distributed by a symmetric 2D Gaussian spatial profile with maximal weight and minimal delay in the center and WSC of 100 and DSC of 100 for all connections. The minimal delay between the FF input and the layer II/III PNs and INs was 0 ms and the layer V PNs and INs was 1 ms. The driving parameters for the ongoing rhythmic input in our model were all

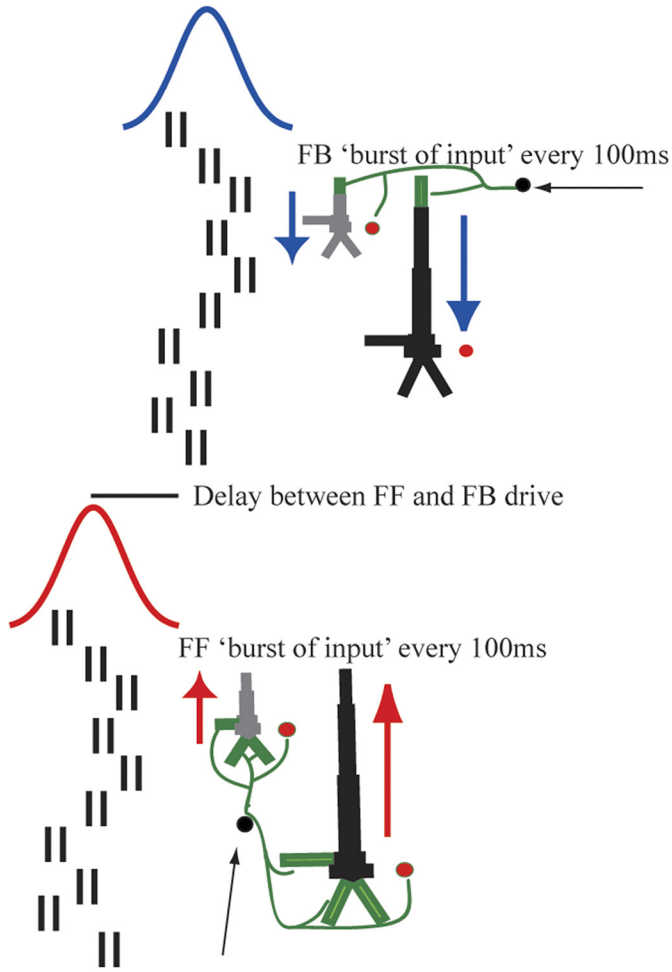

FIG. 2. Schematic illustration of alternating 10-Hz FF and FB drive to the SI network. Approximately every 100 ms (Gaussian, mean interstimulus interval [ISI] 100 ms, SD = 20 ms), 10 "bursts" of input (doublet spike trains, ISI 10 ms) excite the SI network in an FF connection pattern followed by an analogous delayed FB input. Red and blue arrows depict intracellular current flow. FF inputs induce current flow up the dendrites and FB inputs current flow down the dendrites.

chosen so that the oscillations in the pyramidal neurons remained subthreshold (Zhu et al. 2009).

EVOKED RESPONSE INPUTS. These were simulated as in Jones et al. (2007), with a sequence of FF input, followed by FB, followed by a reemergent late feedforward (LFF) input (schematically drawn in Fig. 9*A*). The timing of the input sequence was fixed as in Table 2. Each driving spike train consisted of a single presynaptic spike on each trial and the weights were distributed uniformly across the SI networks as in Table 2. The stochastic ongoing drive was unchanged during the evoked response sequence. Evoked responses were simulated to begin at various phases in simulated mu-alpha and mu-beta cycles as described in RESULTS.

CALCULATION OF NET CURRENT DIPOLE. The SI ECD was calculated as the net sum across the population of the intracellular currents flowing within the PN dendrites in a direction perpendicular to the longitudinal axis of the apical dendrite multiplied by the corresponding length of the dendrite.

SIMULATIONS. All simulations were performed using the shareware software program NEURON (available http://www.neuron.yale.edu/neuron/). A fixed time-step implicit Euler integration method was used with a time increment $dt = 0.025$ ms. Frequency analysis of all simulated rhythms was identical to that performed on the MEG data. Simulated evoked responses were smoothed by convolution with a 15-ms box filter. On publication, the code that produced all simulated data herein will be available on the ModelDB website http://senselab.med.yale.edu/senselab/modeldb/.

RESULTS

MEG experiments

Somatosensory mu rhythm in trial averages. Consistent with previous studies, the ongoing mu rhythm recorded here expressed peaks of activity in the mu-alpha (7–14 Hz) and mu-beta (15–29 Hz) frequency bands. The dual peak in mu can be observed in the mean and SE across subjects of the PSD calculated from the frequency range 1–60 Hz (Fig. 3*A*, blue curve; $n = 10$ Ss, mean of 200 1-s prestimulus trials per subject, calculated with Welch's periodogram; see METHODS). Peaks in both the mu-alpha and mu-beta range are evident in this analysis and the relative mu-alpha and mu-beta expressions vary across subjects (Fig. 3*B*). The gray curve in Fig. 3*A* shows the corresponding results when the data from the three subjects—whose SI dipole localizations were not determined by standard methods—were removed (see METHODS) and their individual subject data are shown in black in Fig. 3*B*. Although the overall power of the oscillations is smaller without these subjects, the overall shape is preserved and the dual-peak mu phenomenon is still present.

The two distinct components, mu-alpha and mu-beta, can be visualized more clearly when looking at time–frequency representations (TFRs; spectrograms) of the data from two example subjects (Fig. 3*C*, average $n = 100$ trials of 1-s prestimulus data, each calculated with Mortlet wavelets; see METHODS). The spectrograms from these subjects show clear bands of mu-alpha and mu-beta activity in the average data. We subsequently show that, although the relative mu-alpha and mu-beta expressions across subjects are not the same, the existence of separable activity in both frequency ranges persists in all subjects and in single trials.

Somatosensory mu rhythm on single trials. These initial analyses suggested that there was not a fixed relationship between mu-alpha and mu-beta expressions across subjects, indicating different neural generators. To further investigate the relation between these bands, we analyzed the spontaneous

TABLE 2. *Exogenous synaptic input parameters for evoked responses*

Parameter	Input Times Across Trials	Maximal Conductance, μS Default AMPA/NMDA
FF to L2/3e	25	0.001
FF to L2/3i		0.002
FF to L5e		0.0005
FF to L5i		0.001
FB to L2/3e	7	0.001/0.001
FB to L2/3i		0.0005/0.0005
FB to L5e		0.001/0.001
LFF to L2/3e	135	0.0053
LFF to L2/3i		0.0053
LFF to L5e		0.0027
LFF to L5i		0.0027

Targeted dendritic compartments are shown in Fig. 1, *B* and *C*. FF, feedforward; FB, feedback; LFF, late feedforward.

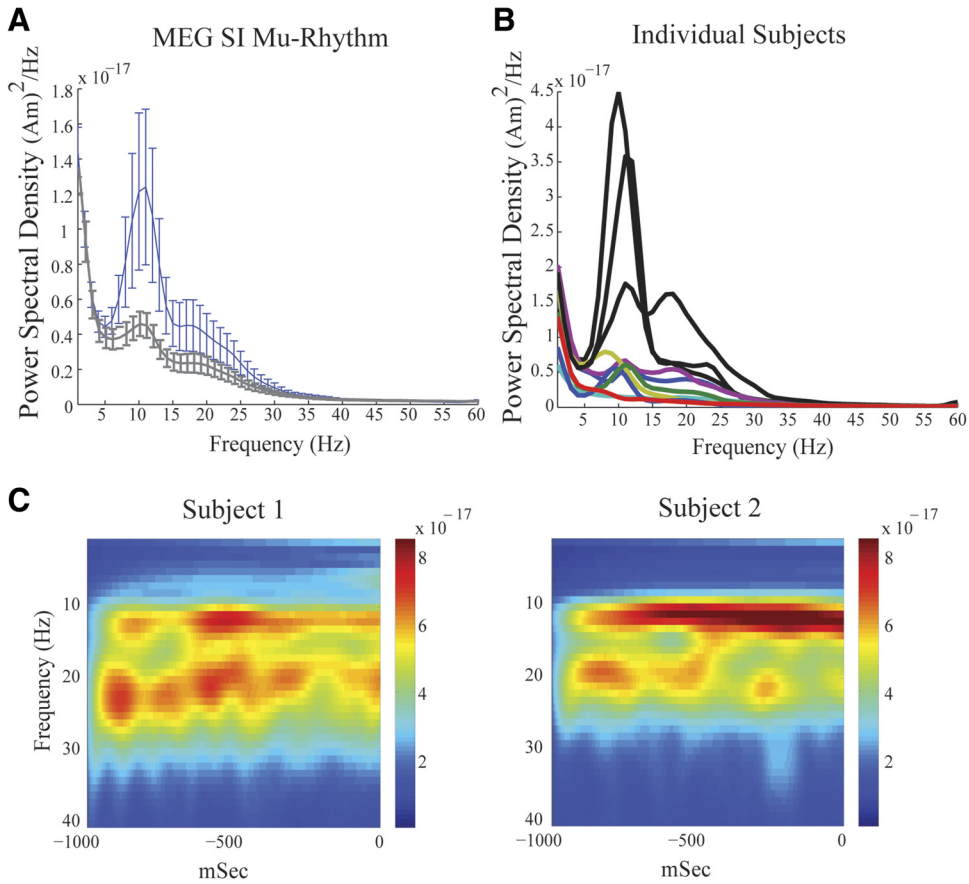

FIG. 3. Magnetoencephalographic (MEG) SI mu rhythms. *A*, blue curve: grand mean power spectral density (PSD) vs. frequency averaged across 10 subjects, 200 trials each (SE bars) showing 2 peaks of activity in the mu-band between 7 and 29 Hz. Gray curve: analogous curve with removal of data from 3 subjects with nonstandard SI dipole localization methods. *B*: PSD vs. frequency in each subject; subjects with nonstandard dipole localization are shown in black. *C*: example frequency vs. time spectrograms averaged over 100 trials (1-s prestimulus time period) from 2 subjects, emphasizing that the SI mu rhythm is a 2-component rhythm containing separate bands of mu-alpha and mu-beta activity. The unit of power is $(Am)^2$.

SI signal in individual trials. Figure 4 shows two examples of SI frequency distributions and corresponding waveforms during 1-s prestimulus epochs for four subjects. These spectrograms are different from the average responses (Fig. 3*C*). In single trials, periods of high mu-alpha and mu-beta power often have nonoverlapping time courses. We note that subjects 3 and 4 had nonstandard dipole localizations and larger overall power (Fig. 3*B*). However, these subjects still showed the characteristic periods of nonoverlapping high mu-alpha and mu-beta power. This feature implies that these rhythms are not simple harmonics, further indicating separable neural generators.

To quantify this observation, we calculated the probability that high power in mu-alpha and mu-beta was expressed simultaneously in the spontaneous mu rhythm. We sorted the relative power of mu-alpha and mu-beta in each 100-ms window. We then calculated the probability that bins in the top third of the mu-alpha and mu-beta power distributions were identical. If these rhythms were generated from an identical neural process, they would be predicted to correlate perfectly. A completely random association would predict overlap on roughly 10% of bins. We found overlap on 50% of bins (Fig. 5, *inset*, 50.31% mean, SD = 0.056% n = 10 Ss, calculated from 2,000 100-ms time windows per subject). This finding implies a degree of independence for the two rhythms, but also that they co-occurred at greater than chance levels, suggesting they share components of neural mechanism.

To further characterize the relation between alpha and beta occurrence, we plotted a histogram of the ratio of alpha to beta power calculated in the same 100-ms time windows (Fig. 5, n = 2,000 trials, 10 Ss, 1,000 bins). The mean and median of the histogram were 2.4 and 1.3, respectively. The normalization applied to the TFR data in our analysis favors the observation of higher-frequency bands (see METHODS). As such, the dominance of alpha power in this analysis, despite the normalization applied, underscores the relative prevalence of this oscillation in the mu signal.

Computational neural model

Simulating MEG SI activity. We have previously developed a laminar SI model that predicted the neural origin of the tactile-evoked response in MEG and provided insight into the changes in this response that predicted successful detection of a threshold-level stimulus (Jones et al. 2007). Here, we expanded this model from 10 pyramidal neurons (PNs) and 3 interneurons (INs) per layer, to a grid of 100 PNs and 35 INs per layer (see METHODS, Fig. 1) and used it to investigate the neural origin of the spontaneous SI mu rhythm, its modulations in power, and how these modulations influence cortical excitability and evoked response gain.

As in our previous study (Jones et al. 2007), the model consisted of a biophysically realistic laminar cortical model of a local SI network (Fig. 1). Two types of exogenous drive provided excitatory synaptic input to the SI column, one in an FF connection pattern representing input from the thalamus to layer IV and subsequently to layer II/III (Fig. 1*B*), and one in an FB connection emulating higher-order cortical sources to the superficial layer II/III (Fig. 1*C*).

The MEG SI ECD is calculated by the net longitudinal current flow within PNs in the model (Hamalainen et al. 1993;

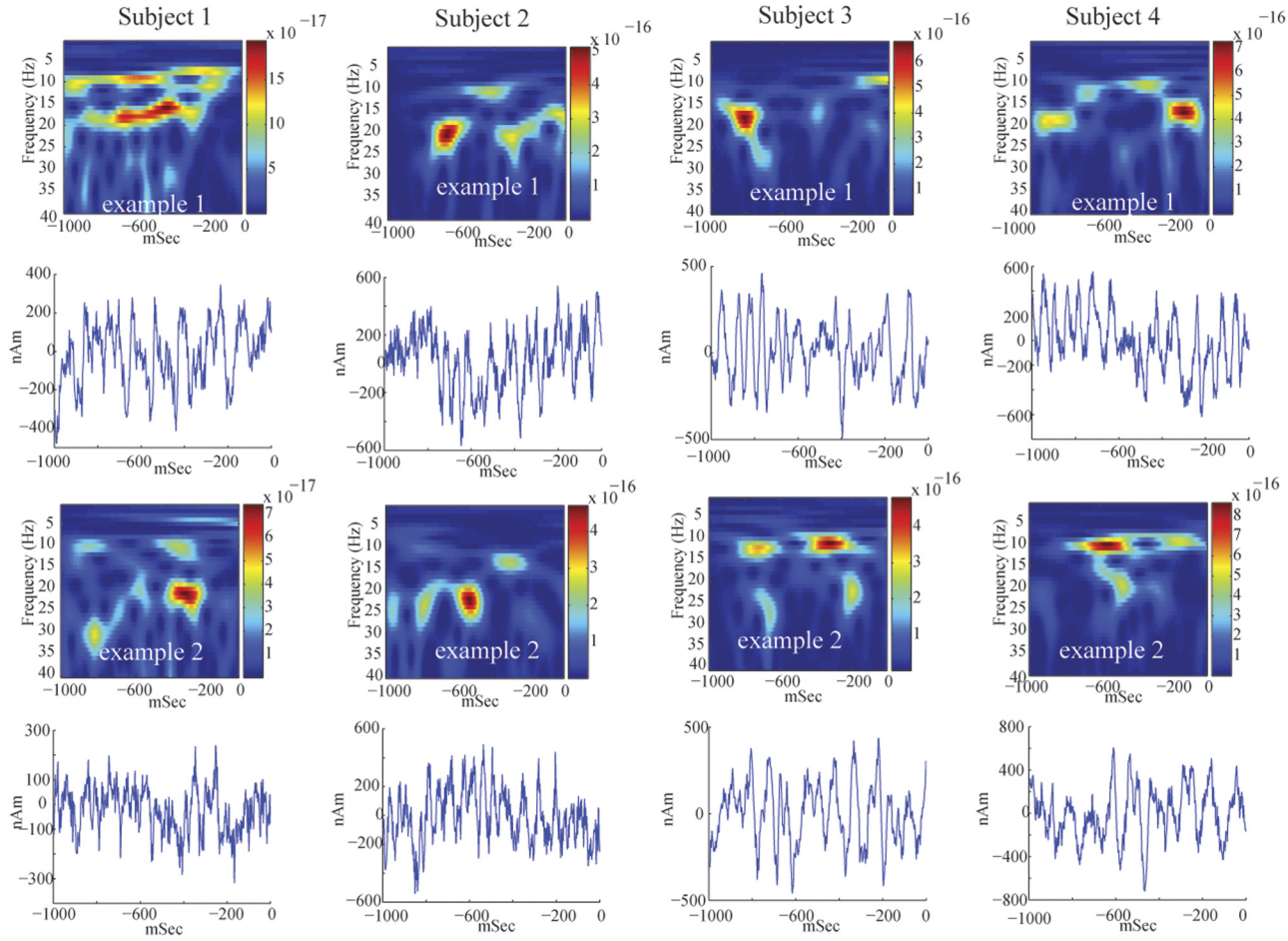

FIG. 4. Single-trial mu rhythms. Two examples of single-trial SI frequency spectrograms and waveforms from 4 subjects. The unit of power is $(Am)^2$. On a single-trial basis, peaks in mu-alpha and mu-beta power often occur at different points in time, indicating that the rhythms are not harmonics of each other and may have different neural sources. The corresponding waveforms oscillation around zero polarity.

Hari and Salmelin 1997; Hari et al. 1980; Ikeda et al. 2005; Jones et al. 2007; Okada et al. 1997). Therefore the polarity of the waveform of a given oscillation provides specific insight into the direction of current flow within the pyramidal neurons across the cortical lamina. In a previous study (Jones et al. 2007), we determined that positive polarity corresponded to net current flow anterior, which in the case of area 3b corresponds to flow "up" the PN dendrites toward the cortical surface and negative polarity corresponded to net current flow down the PN dendrites toward the cell bodies/white matter (see METHODS). The example single-trial waveforms of the spontaneous SI mu rhythm in Fig. 4 (*bottom panels*) oscillated around zero for each subject, suggesting current flow that oscillates up and down the cortical laminae.

Nearly synchronous stochastic FF input followed by FB input creates a physiologically realistic mu rhythm. Our strategy for simulating single-trial mu rhythms in the model was based on current theories as to the origin of 10- and 20-Hz activity in the cortex (see INTRODUCTION and METHODS). In expanding our cortical model to study the mu rhythm, we included several intrinsic currents in our PNs that have previously been proposed to be important in the generation of alpha and beta activity (h-currents, T-currents, M-currents, Ca-currents). We initially thought that these currents would be essential for the generation of the mu-alpha and mu-beta components of the SI mu rhythm. Because our network was trying to reproduce in vivo data from awake humans, we also included exogenous driving inputs to the SI network in an FF and FB manner (Fig. 1). In the following text, we show that, whereas the intrinsic currents necessarily define the time constant of integration along the dendrite, the timing and strength of the excitatory FF and FB inputs determine the mu-alpha and mu-beta expression.

To simulate the single-trial spontaneous SI MEG mu rhythms, as shown for example in Fig. 6*A*, we first drove the SI network with a stochastic approximately 10-Hz burst of FF rhythmic drive, to see whether the mu rhythm would emerge from this simulated rhythmic lemniscal thalamic input combining with intrinsic cellular and local network properties. Details of the driving sequence are shown in Fig. 2 and described in METHODS.

The spectrogram from the simulated data in Fig. 6*B* shows that approximately 10-Hz FF rhythmic input alone created a primarily 10-Hz response in the model. The corresponding waveform shows that each cycle of the FF input created an upward current flow in the pyramidal neuron dendrites, resulting in a solely positive-polarity oscillation that lasted about 100 ms. This waveform contrasts with MEG data, where the polarity of the signal oscillates around zero (compare waveforms in Fig. 6, *A* and *B*; see also Fig. 4), suggesting that the current

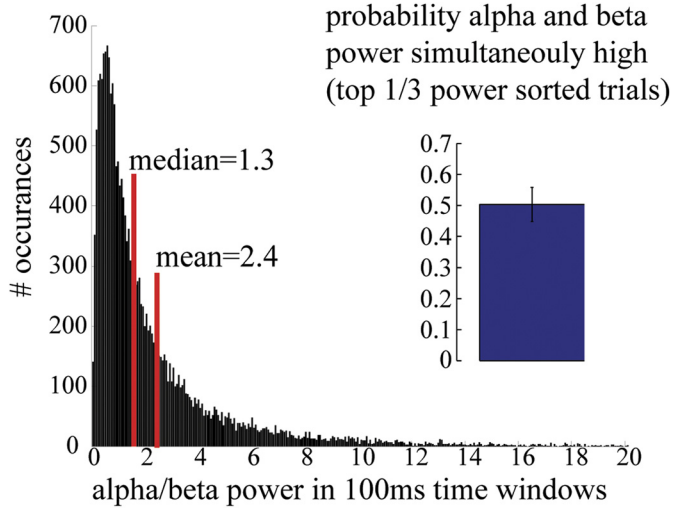

FIG. 5. Mu-alpha and mu-beta components of the MEG SI mu rhythm are nonoverlapping MEG data showing a histogram of the ratio of alpha to beta power over 100-ms time bins (n = 2,000 trials, 10 Ss). The mean (2.4) and median (1.3) of this histogram are >1, underscoring the relative prevalence of alpha power in the mu signal. *Inset*: MEG data showing probability that high mu-alpha and mu-beta power (top 33% of all power) occur simultaneously roughly 50% of the time (mean = 50.31%; SD = 0.056%).

flow oscillates up and down the pyramidal neurons. Importantly, consistent with the notion that large-scale MEG/EEG ongoing oscillations represent the subthreshold activity of large numbers of synchronous neurons (Zhu et al. 2009), the driving parameters in our model were all chosen so that the oscillations in the pyramidal neurons remained subthreshold.

Our previous modeling study (Jones et al. 2007) showed that negative-polarity signals could be produced by FB excitatory input to the apical dendrites of pyramidal neurons lying in the superficial layers that induce a downward current flow. Therefore emulating approximately 10-Hz FB, a second stochastic 10-Hz burst of rhythmic excitatory synaptic input was provided to the apical dendrites of the layers II/III and V pyramidal neurons. The statistics of this FB drive were analogous to the FF drive, as described in METHODS and shown schematically in Fig. 2. Approximately every 100 ms, an FF burst was followed by an FB burst. In the example shown in Fig. 6*C*, on each cycle, the FF and FB inputs were nearly synchronous (Gaussian mean difference, 5 ms; FF and FB weights, 0.4 pS; n = 10; variance, 400). See the following text for further details on the importance of phasic latency and other input statistics (Fig. 8). Under these conditions, the 10- and 20-Hz components of the mu rhythm were robustly reproduced and the waveform of the rhythm oscillated around zero, with a subset of nonsimultaneous intervals of strong mu-alpha and mu-beta power, as observed in our MEG data (compare Fig. 6*C* with Fig. 6*A* and Fig. 4). The parameters regulating the mu-alpha and mu-beta components are described in detail in the following section (Fig. 7).

To test whether the waveforms are symmetric around zero, we calculated a symmetry index (SInd) for the MEG (Fig. 6*D*) and model data (Fig. 6*E*). The SInd was derived as described in METHODS and is such that a positive SInd value indicates greater-amplitude peaks, a negative value indicates greater-amplitude troughs, and a zero value indicates that an oscillation was symmetric around zero. Figure 6*D* (*top panel*) depicts the mean and SD of the SInd for each of the 10 subjects (n = 200, 1-s prestimulus trials); the *bottom panel* shows a histogram of the SInd across all subjects and trials, with the *inset* showing the mean and SD of the histogram. The SD of each individual subject overlaps zero, with four subjects >0 and six <0. The SInd was not significantly different from zero across the subjects ($P < 0.001$, t-test). Similarly, Fig. 6*E* shows a histogram of the SInd across trials in the model (n = 40, 1-s trials, parameters as in Fig. 6*C*) and *inset* with mean and SD of the histogram. As in the MEG data, the SInd index in the model was not significantly different from zero ($P < 0.001$).

In the model, prominent mu-beta cycles emerged when the stochastic FB input came in at the proper moment and strength to cut the FF alpha cycle in half (compare red boxes in Fig. 6, *B* and *C*), creating an oscillation that looks similar to that in the MEG data (Fig. 6*A*). As described historically in recordings of the MEG mu rhythm, our SI signal waveforms exhibit a "comb-like" or "arch-shaped" signal (Tiihonen et al. 1989), where the upward deflections appear more rounded, whereas the downward deflections have sharp edges forming what looks like several connected arches, as shown in Figs. 4 and 6*A*. This feature is also qualitatively reproduced by our model data (Fig. 6*C*) and arises as follows in the model. The 10-Hz FF input produces positive upward deflections that last about 100 ms (i.e., the rounded portion of the "arch"; Fig. 6*B*, *right*). The additional nearly 10-Hz FB input acts to push current flow in the opposite direction. In the example shown in Fig. 6*C*, the 10-Hz FF and FB inputs arrive nearly synchronously (5-ms delay); thus for part of the upward deflection the FB input works directly against the FF input, whereas at the end of the upward deflection, the FB input is able to abruptly push current flow down the dendrites, creating the "sharp" downward edges of the arch.

To create oscillations that were the same magnitude as that of oscillations seen experimentally, on the order of 100 nAm (Fig. 6*A*, *right*), the modeling data were multiplied by 30,000 (Fig. 6. *B* and *C*, *right*), which suggests that the subthreshold activity of nearly 200 × 30,000 = 6 million layers II/III and V pyramidal neurons contributed to the observed mu rhythm. Based on the general estimate of about 75,000 PNs per about 1 mm^2 of the cortical sheet (Cheung et al. 2007), these findings suggest that in this study, about 80 mm^2 (0.8 cm^2) of cortical space was synchronized to generate the observed rhythms. This volume estimate would lie within the volume of the human hand representation, defined as the omega-shaped bend in the postcentral gyrus (Moore et al. 2000). This prediction is significantly larger than the number of neurons predicted to contribute to the tactile-evoked response in our previous and current modeling results shown in Fig. 9*A*, which was on order of 60,000 spiking neurons (200 PNs × 300 scaling factor = 60,000 PNs).

Statistical properties of the mu rhythm on single trials. To further validate the model prediction that the SI mu rhythm is created by nearly synchronous, stochastic, alternating 10-Hz FF and 10-Hz FB inputs, we quantified other properties of the simulated mu rhythm in a manner analogous to the MEG data. In each case, we found consistency between the MEG and model data.

First, we calculated the mean and SE of the PSD for frequencies from 1 to 60 Hz across 100 1-s trials of the stochastically simulated spontaneous mu rhythm (Fig. 7*A*, n = 50 trials; all parameters fixed as in Fig. 6*C*). Peaks of activity

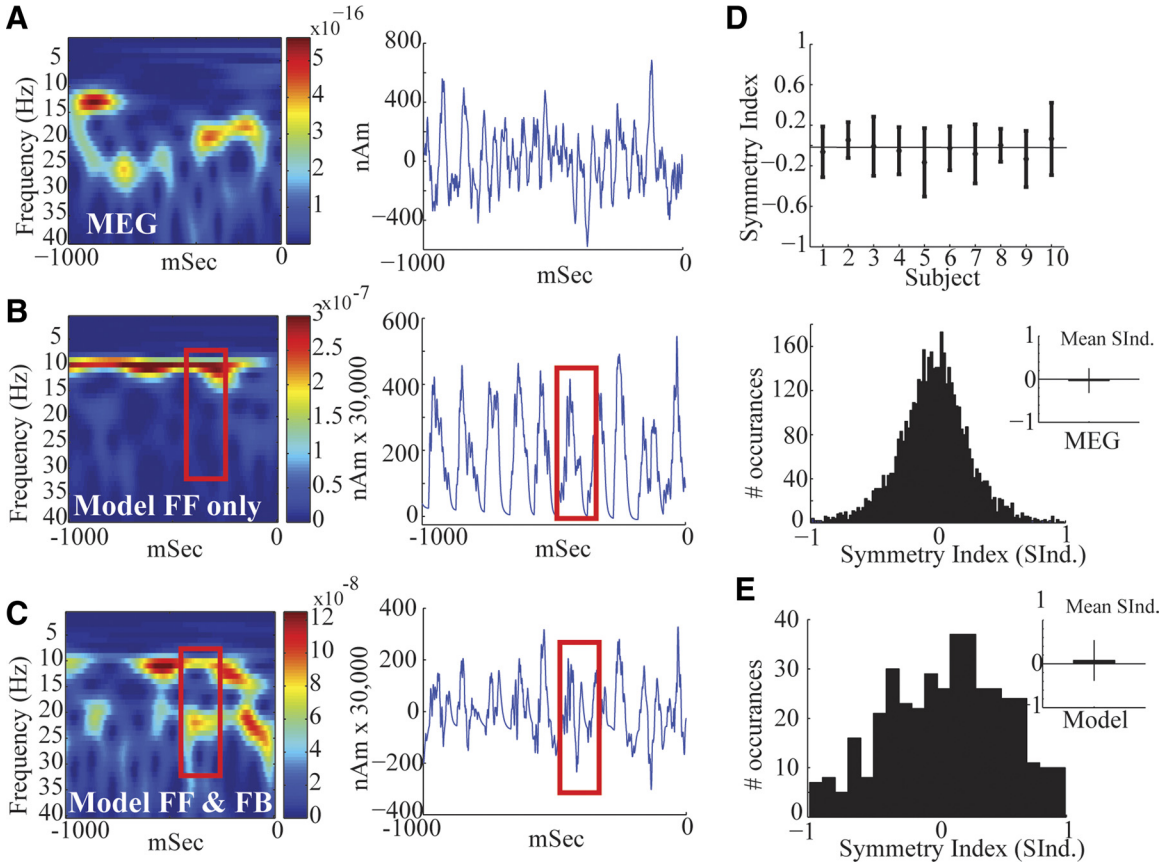

FIG. 6. Modeling SI mu rhythms with alternating nearly synchronous approximately 10-Hz FF and FB input. *A*: MEG data showing an example prestimulus SI mu rhythm from a single trial. *B*: simulating 10-Hz stochastic FF inputs only to SI (depicted schematically in Fig. 2) reproduces a strong 10-Hz MEG signal and very weak 20 Hz. The unit of power is $(Am)^2$. *C*: alternating 10-Hz FF followed by 10-Hz FB inputs (5-ms delay) reproduces equal power, nonoverlapping, 10- and 20-Hz components, with a waveform that oscillates around zero, analogous to the experimental MEG data. Red boxes show that mu-beta cycles emerge when the FB input is strong enough to cut the mu-alpha oscillation in half. *D*, *top*: mean and SD of the symmetry index (SInd) of the MEG SI mu rhythm waveform around zero, for each subject. *Bottom*: histogram of SInd across all subjects and trials. *Inset*: mean and SD of histogram. The SInd is not significantly different from zero ($P < 0.001$). *E*: analogous histogram of SInd across trials in the model ($n = 40$, 1-s trials, parameters as in *C*), which is also not significantly different from zero ($P < 0.001$). *Inset*: mean and SD of histogram.

emerge in the mu-alpha and mu-beta range. As in the grand average MEG data, the mu-alpha power has a higher peak in this PSD analysis, but a second smaller peak in the mu-beta range is also present (compare Fig. 7*A* with Fig. 3*A*).

Second, we calculated the probability that, for a given 100-ms time window, mu-alpha and mu-beta were in the top third of trials sorted from low to high power in the model. We found that they co-occurred roughly 50% of the time (Fig. 7*B*, *inset*, 48.7% calculated from 100 100-ms time windows), analogous to the mean of our grand-average MEG data (compare with Fig. 5, *inset*).

Third, we plotted a histogram of the ratio of alpha to beta power calculated in 100-ms time windows (Fig. 7*B*, grand total 1,000 prestimulus time windows, 100 bins). We found that the distribution of this histogram had the same qualitative shape as that calculated from the MEG data (compare Figs. 7*B* and 5). Further, as in the MEG data, the mean (1.4) and median (1.1) of the histogram were >1. A further examination of the model

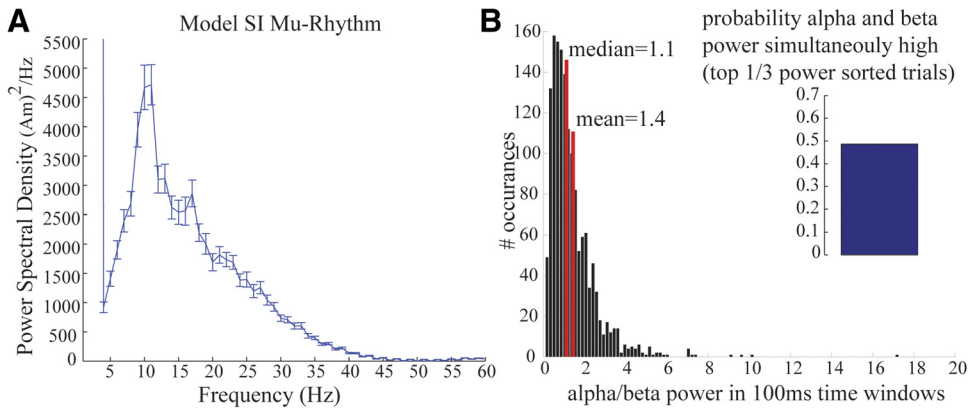

FIG. 7. Mu-alpha and mu-beta components of model SI mu rhythms are nonoverlapping. *A*: PSD vs. frequency averaged across 50 trials (SE bars) showing 2 peaks of activity in the mu-band between 7 and 29 Hz, in agreement with the MEG data (compare with Fig. 3*A*). *B*: model data showing a histogram of the ratio of variance to power over 100-ms time windows ($n = 1{,}000$ trials). The mean (1.4) and median (1.1) of this histogram are >1, analogous to the MEG data (compare with MEG data in Fig. 5). *Inset*: model data showing probability that high mu-alpha and mu-beta power (top 33% of all power) occur simultaneously roughly 50% of the time (mean = 48.6%, calculated from 100 0.1-s time windows of simulated data; compare with MEG data in Fig. 5, *inset*).

parameters controlling the relative dominance of alpha and beta power is given in the following text (Fig. 8).

Parameters controlling relative mu-alpha and mu-beta power dominance. We varied the statistics of the input patterns shown schematically in Fig. 2 and detailed in METHODS, to examine their effect on the dominance of mu-alpha or mu-beta power expressed in the spectrograms generated from the model data. We began by parametrically varying the mean delay between the approximately 10-Hz FF and FB input, from 0 to 95 ms at 5-ms intervals (Fig. 8*A*; all other parameters were fixed as in Fig. 6*C*; also see METHODS). We calculated the mean ratio of mu-beta/mu-alpha power over a 1-s simulation and found that when inputs arrived nearly synchronously with FB following FF (delay <10 ms), or vice versa, the relative dominance of mu-alpha and mu-beta power was approximately equal (mu-beta/mu-alpha power ≃ 1; see endpoints of parabola in Fig. 8*A*). In contrast, when the alternating approximately 10-Hz FF and FB inputs were asynchronous (delay = 50 ms), the mu-alpha rhythm dominated the signal (mu-beta/mu-alpha ≃ 0). In this case, the FF input created a positive-polarity signal for half of a 10-Hz cycle and the FB input created a negative-polarity signal for the remaining half of a 10-Hz cycle, where the peaks of the two halves are 50 ms apart, defined by the 50-ms delay (data not shown).

We then investigated the influence of the variance (relative synchrony in presynaptic spiking, set by the SD of the "input bursts"), amplitude (measured as number of "input bursts"), and efficacy (differences in the postsynaptic conductance evoked by an identical presynaptic input) of the separate FF and FB inputs on the relative mu-beta to mu-alpha power (Fig. 8, *B*, *C*, and *D*, respectively; each parameter was tested at the three values on the *x*-axis; see METHODS and Fig. 2 for definition and illustration of each parameter). In each case, manipulations that enhanced the FF drive [increased synchrony (decreased variance), amplitude, and postsynaptic conductance] increased mu-alpha power (red curves), and manipulations that enhanced FB drive increased mu-beta power (blue curves).

Each of these mechanisms for increasing drive to the network [increased synchrony (decreased variance), amplitude, and efficacy of postsynaptic input] had the net effect of increasing the size of the net postsynaptic conductance. Based on this parameter search, in the remainder of our modeling investigation we simulated high mu power by simultaneously increasing the postsynaptic conductance of the FF and FB inputs, thus producing an increase in mu-alpha and mu-beta power (Fig. 8*E*). Low mu power was simulated with smaller postsynaptic conductance (high mu 0.6 pS to PNs and 1.2 pS to Ins; low mu 0.4 pS to PNs and 0.8 pS to INs).

Impact of mu power on tactile-evoked responses. Our previous modeling results indicated that the SI-evoked response measured with MEG was created by a specific temporal sequence of exogenous excitatory inputs to the SI network (Jones et al. 2007). This sequence consisted of FF input at ≃25 ms poststimulus, followed by FB input at ≃70 ms, and by a late

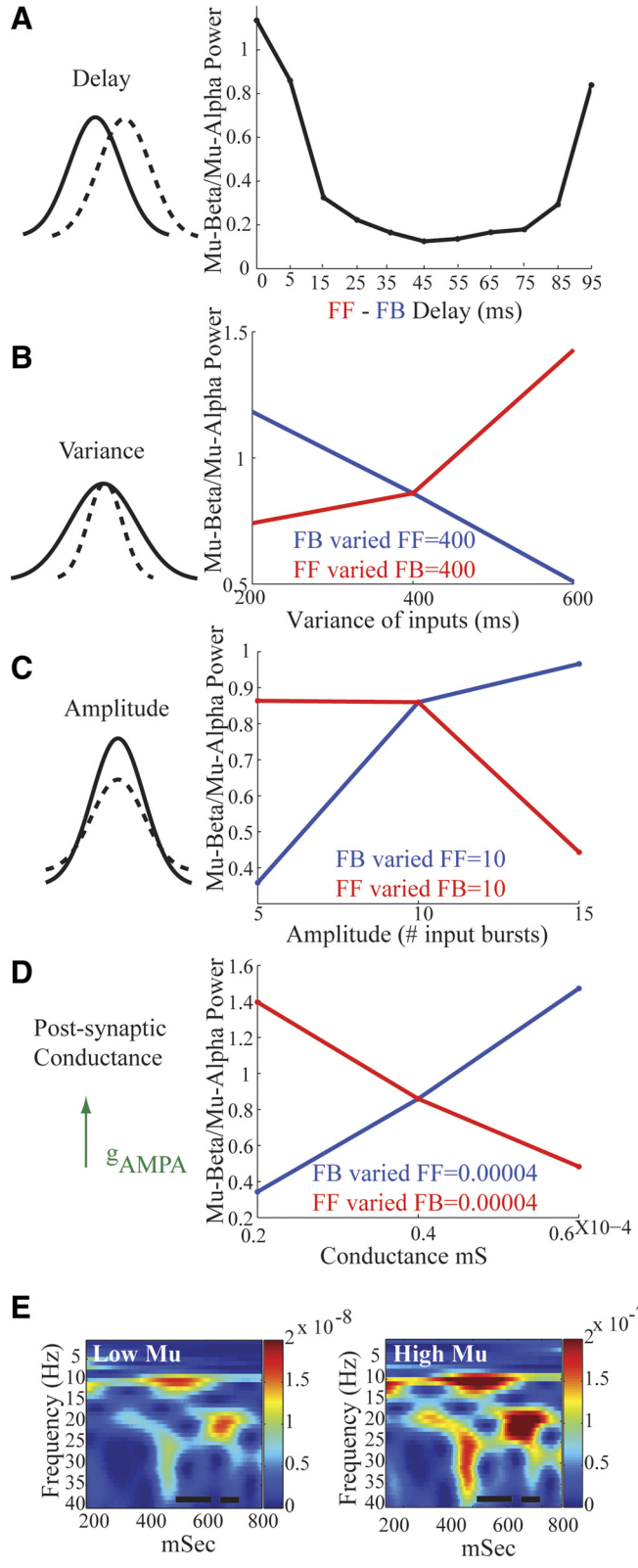

FIG. 8. Statistics of FF and FB input that influence relative mu-alpha and mu-beta power. *A*: small delays (mean <10 ms) between approximately 10-Hz FF and FB drives create nearly equal mu-alpha and mu-beta power (mu-beta/mu-alpha ≃ 1). If the FF inputs are increased via increased synchrony (decreased variance, *B*), amplitude (*C*), or postsynaptic conductance (*D*), the relative mu-alpha dominance increases (mu-beta/mu-alpha decreases, red curves). Analogous increases in the FB input increase the relative mu-beta power (mu-beta/mu-alpha increases, blue lines). *E*: simulated high and low mu rhythms (Low Mu FF = FB postsynaptic conductance = 0.4e-4 millisiemens [mS], High Mu FF = FB postsynaptic conductance = 0.6e-4; each FF = FB variance = 400 ms and amplitude = 10 input bursts). The unit of power is $(Am)^2$. Black bars represent time windows in which evoked responses are simulated in Fig. 9*A*.

feedforwad (LFF) input at ≃135 ms (shown schematically in Fig. 9*A*, where each input consisted of single presynaptic spikes per trial; see METHODS). The sequence that induced the SI-evoked signal may be interpreted as initial FF input from the periphery through the lemniscal thalamus to granular layers, followed by FB input from higher-order cortex or nonspecific thalamic sources to the supragranular layers, followed by a second wave of lemniscal thalamic input to the granular layers.

Here, we used our expanded model to investigate the effects of prestimulus mu power on SI-evoked response magnitude and timing. The evoked response input sequence was delivered at several starting phases (SPs) within simulated high and low prestimulus mu-alpha and mu-beta cycles (marked with black bars in Fig. 8*E*) and results were averaged (Fig. 9*A*). The SP is defined as the mean time of the initial lemniscal thalamic FF input to the SI network, which was followed by FB input 45 ms later (mean SP +45 ms) and a subsequent LFF input 65 ms later (mean SP +65 ms). This sequence was delivered at 20 different equally spaced SPs in the marked mu-alpha cycle and 10 different equally spaced SPs in the marked mu-beta cycle; the results were averaged over all 30 trials (see Table 2 for default postsynaptic conductances and input times of evoked response inputs).

When given during either high or low prestimulus mu power, the average simulated evoked response created a waveform with a negative-polarity peak at about 70 ms (M70) and two positive-polarity peaks at about 100 ms (M100) and about 135 ms (M135), respectively (Fig. 9*A*). The timings and polarities of the peaks are similar to those generated in our previous study, in which prestimulus rhythms were not considered (Jones et al. 2007).

Several significant differences emerged in the evoked response waveforms simulated during low and high prestimulus mu conditions (compare dark and light blue curves in Fig. 9*A*; red stars indicate time points where the difference was $P \leq 0.05$; purple stars: $P \leq 0.01$, paired t-test, $n = 30$ trials). The greatest difference was the emergence of a positive peak near approximately 50 ms, labeled M50, under high prestimulus mu that was negligible under low mu (M50 = max 40–60 ms, $P < 0.01$). In addition, in the model, the magnitude of the M70 was

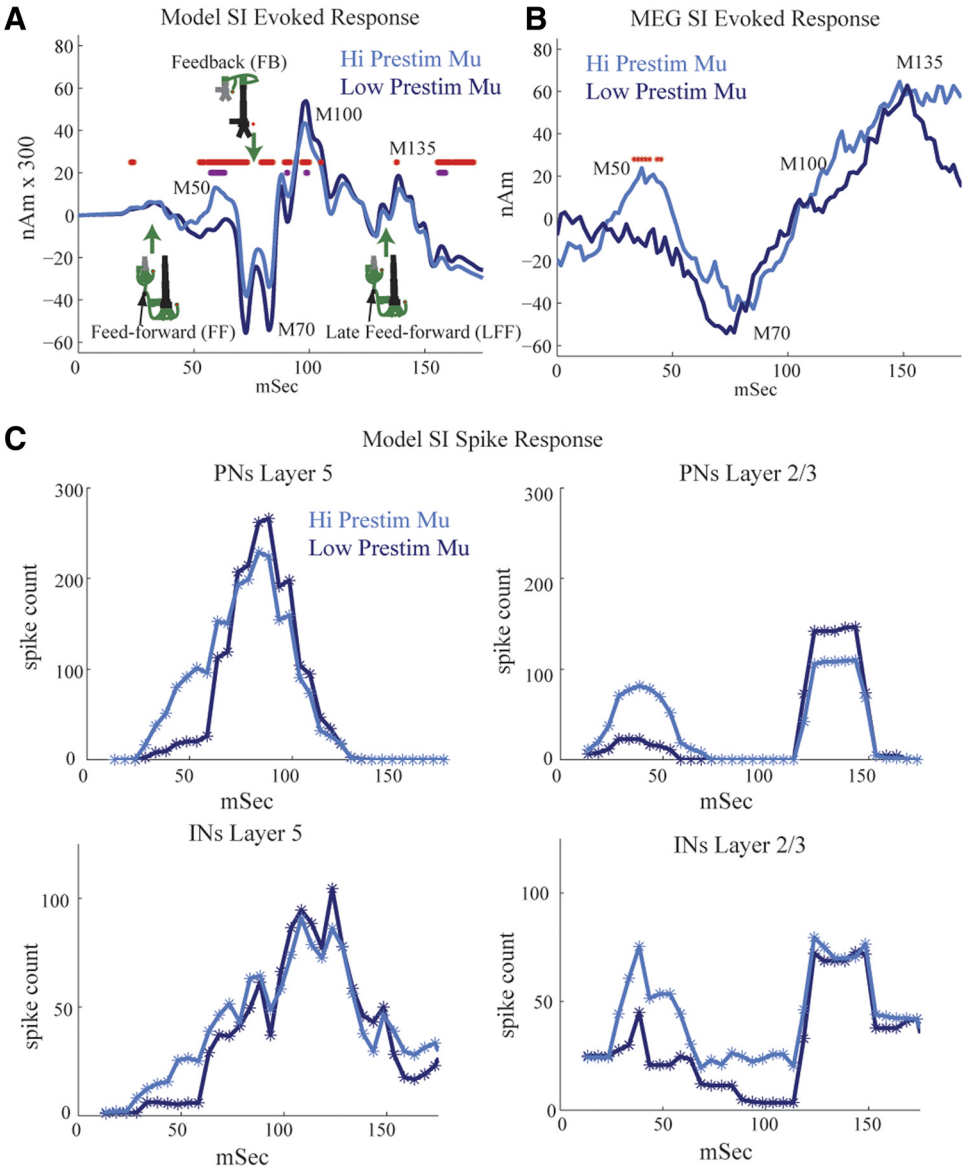

FIG. 9. Modeling the impact of mu on SI-evoked responses. *A*: simulated evoked responses under high and low mu conditions. High mu creates an early positive peak at about 50 ms (M50) and subsequent suppressed response at about 70 ms and later (difference between high and low mu; purple stars, $P < = 0.01$; red stars, $P < = 0.05$, paired t-test, mean $n = 30$ trials each, with starting phases equally spaced in mu-alpha and mu-beta cycles shown with black bars in Fig. 8*E*). *B*: MEG SI-evoked responses sorted over high and low prestimulus mu power (50% detection rate) reveals early M50 peak and trend to decreased M70 peak under high mu, as predicted by the model (red stars, $P < = 0.05$). *C*: evoked spike rates of neuron populations under high and low prestimulus mu. Under high mu conditions, the initial roughly 25-ms evoked input to the SI network induces greater firing in the INs and PNs and thus an early positive peak near 50 ms (M50) in the SI-evoked response. Activity in the INs suppresses subsequent firing and a slight decrease in the magnitude of the evoked response, beginning at about 70 ms. In contrast, under low mu conditions, the initial evoked input induces little inhibitory firing from the initial FF at ≃25 ms input and thus a slightly greater evoked response beginning at about 70 ms.

smaller (M70 = min 50–100 ms, $P < 0.05$). There were also slight but significant differences between the M100 and M135 peaks, and later [150–175] ms activity such that the magnitude was larger under low mu conditions (M100 = max 75–125; M135 = max 125–175, mean 150–175 ms, $P < 0.05$; see Fig. 9*A*). Predictions as to the underlying neural activity creating these differences are discussed in the following text (Fig. 9*C*).

We next related these predicted differences to the SI-evoked response waveforms in the MEG signal and found consistency between the model and experimental data. Figure 9*B* shows the MEG SI-evoked response sorted over high and low prestimulus mu trials for an equal number of hit-and-miss trials comprising a 50% detection rate ($n = 10$ Ss, 30 high and low mu trials per subject). We found that the prestimulus mu power significantly influenced the early evoked response (<70 ms), and showed trends to a difference in the later components. As in the model data, a significant positive peak near 50 ms, labeled M50, emerged under high prestimulus mu (Fig. 9*B*, $P < 0.05$ marked with red asterisks). This peak was followed by a trend that approached significance for a decreased M70 peak under high mu (M70 = min 60–75 ms, $n = 7/10$ Ss, $P = 0.1$ sign-test), followed by a late trend toward larger magnitude under high mu (mean 150–175 ms, $n = 8/10$ Ss, $P = 0.055$ sign-test).

The late trend to higher-magnitude response under high mu conditions and the nonreturn to baseline between the M100 and M135 peaks, in the MEG data are discrepant with the model results. The nonreturn to baseline was also observed in our previous study (Jones et al. 2007) where the strengths of the FF and FB inputs in the current study were derived. One way that this difference could be rectified in the model is by assuming that the late FF input at ≃135 ms synchronously drives a greater number of neurons. This effect can be achieved in the model by multiplying by a separate increased scaling factor at the late time points (>100 ms; data not shown). A large late FF input that occurs ≃135 ms after the stimulus may arise as part of an induced poststimulus approximately 10-Hz thalamocortical oscillation, which may be stronger with high prestimulus mu. A strong induced 10-Hz oscillation is consistent with the notion that the stimulus "phase resets" the 10-Hz component of the oscillation (Hanslamayer et al. 2007; Makeig et al. 2002).

Increased excitation and inhibition during high mu influences the M50 and M70 and evoked response peaks. To better understand how increased prestimulus drive during high-prestimulus mu rhythms created an initially larger M50 response followed by a smaller M70 and later response between the M100 and M135 peaks, we examined the evoked spiking in the network model. We plotted the mean number of spikes (smoothed over 5-ms bins) for the pyramidal and inhibitory neuron populations in our network during high and low prestimulus mu power (Fig. 9*C*, pooled responses, 30 trials). We found that when the evoked response was simulated during high mu power (light blue curves), the FF input at ≃25 ms induced more spiking in pyramidal and inhibitory neurons in layers II/III and V compared with low mu (dark blue curves). Firing in the pyramidal cells to the initial FF approximately 25 ms input peaked near 50 ms, creating the initial M50 positive peak seen in the evoked response following high prestimulus mu (light blue curve, Fig. 9*A*). The positive polarity of the M50 peak comes from back-propagation of action potentials up the apical dendrites of the pyramidal neurons (Jones et al. 2007). The strong early evoked inhibition suppresses the pyramidal response to subsequent FB input at about 70 ms, creating a decreased response and less spiking under high mu conditions (compare <70 ms dark and light traces for L5 and L2/3 excitatory cells in Fig. 9*C*). In turn, the decreased activity in the E cells created a smaller M70 and later responses in the model (compare dark blue and light blue curves in Fig. 9*A*).

DISCUSSION

We used MEG imaging and biophysically principled computational neural modeling to provide a detailed characterization of the mu-alpha and mu-beta components of the spontaneous SI mu rhythm, investigate its neural origin, and investigate its impact on early (0–175 ms) evoked responses. The MEG recordings revealed an SI mu rhythm with mu-alpha and mu-beta components, whose relative expression was subject dependent. On single trials, the mu-alpha and mu-beta components were not simultaneous in their emergence, but did co-occur at rates greater than chance.

Our model results led to the novel prediction that the SI mu rhythm arises from a stochastic nearly synchronous alternating sequence of approximately 10-Hz FF followed by FB excitatory input to SI. Simulating mu in this manner reproduced many key features of the MEG data, including: a mu rhythm with both mu-alpha and mu-beta components; a rhythm that oscillates symmetrically around zero polarity; nonsimultaneity of mu-alpha and mu-beta components in time; and an enhanced early (M50) peak in the tactile-evoked response under high mu.

The predicted enhancement in the early response when stimulus presentation coincided with epochs of high mu power was observed in our data. We note that the model was completed prior to running our analyses of rhythmogenesis or evoked response modulation and that the only model parameters available to manipulation during analysis were those described in the text (primarily the strength and arrival synchrony of FB and FF signals). The convergence of experimental and model analysis given this principled modeling approach supports the predictive value of the neural interpretation of model behavior.

To our knowledge, our results provide the first evidence that the mu rhythm arises from the combination of two stochastic approximately 10-Hz rhythms that arrive to the SI network at different laminar locations corresponding to thalamic FF input and intracortical FB input. Because the rhythmic approximately 10-Hz FF and FB inputs and SI cortical structure in our model are defined by general principles of cortical circuitry (Felleman and Van Essen 1991; Hughes and Crunelli 2005), the predicted mechanisms may be applicable to the generation of mu-alpha and/or mu-beta frequency rhythms observed in other cortical areas. Table 3 summarizes the results of our MEG findings, the corresponding predictions of our biophysical model, and the mechanistic interpretation of each finding from the model.

Importance of feedforward and feedback input

In expanding our previous SI model (Jones et al. 2007) to study mu rhythms, we included several pyramidal neuron intrinsic currents (see INTRODUCTION and METHODS) and local excitatory and inhibitory interactions, hypothesizing that these factors would prove important for the generation of the mu-alpha and mu-beta components of the SI mu rhythm. Because our network was trying to reproduce in vivo data from awake

TABLE 3. *Summary of MEG results, model reproductions, and predicted neural mechanisms*

MEG Data	Model Reproduction	Predicted Neural Mechanisms
(1) Mu rhythm originating from SI with mu-alpha and mu-beta components (Fig. 3).	Net subthreshold intracellular current flow in layers II/III and V PNs (the simulated SI MEG signal) produced a mu rhythm with mu-alpha and mu-beta components (Fig. 6*C*).	The mu-alpha rhythm is generated by thalamic lemniscal input generating current flow propagation up the PN dendrites primarily away from the soma. The mu-beta rhythm is generated by input from other cortical regions outside the hand representation expressing a mu-alpha oscillation. This input arrives in layers II/III and generates current flow "down" PN dendrites toward the soma. The arrival time of this intracortical input is stochastic and nearly synchronous in alternating with the ongoing approximately 10-Hz FF thalamic input. Alternative distal dendritic inputs (e.g., from nonspecific thalamic projections) could also contribute to mu-beta emergence.
(2) Mu rhythm oscillates around zero with both current polarities present (Figs. 4 and 6, *A* and *D*).	Simulated mu rhythm exhibited current flow that oscillates up and down the cortical layers symmetrically around zero (Fig. 6, *C* and *E*).	Alternating excitatory synaptic drive to dendrites in the infragranular layers (FF) and supragranular (FB) layers drives subthreshold intracellular current flow up and down the PN dendrites.
(3) Mu-alpha and mu-beta components often occurred at different times (Figs. 4 and 5).	Simulated mu rhythm contained mu-alpha and mu-beta components that had the same simultaneity characteristics as those of the MEG data (Figs. 6*C* and 7*B*).	Stochastic in timing of each FF and FB "input burst" (Fig. 2), arriving about every 100 ms, changes the relative dominance of the net FF and FB input strength on each cycle. Enhancing the FF inputs increases the mu-alpha power, whereas enhancing the FB inputs increases the mu-beta power (Fig. 8).
(4) As predicted initially by the model, tactile evoked responses during high prestimulus mu-, compared with low-mu conditions, exhibited an early M50 positive peak, followed by a trend toward a decreased M70 peak (Fig. 9*B*).	Simulated SI evoked responses via a sequence of FF (~25 ms post-stim) followed by FB (~70 ms) and LFF input (~135 ms) input during high mu, compared with low mu (Fig. 8*E*) exhibited an early M50 positive peak and a decreased M70 peak (Fig. 9*A*).	High-mu states created an ongoing depolarization in the PNs and INs, causing greater firing in both populations to the initial FF input. Back-propagation of action potentials in the PNs created the M50 peak. Recruited inhibition in turn decreased the subsequent excitatory cell response to the approximately 70-ms FB input, decreasing the M70 peak (Fig. 9*C*).

humans, we also included exogenous driving inputs to SI in an FF and FB manner (Fig. 1). In contrast to our initial assumptions, we found that although the intrinsic current kinetics in the pyramidal neurons were essential to the time constant of the subthreshold integration of current flow along the dendrites, the dominant time constants regulating mu-alpha and mu-beta frequency in the model were determined by the relative strength and timing of the exogenous rhythmic excitatory inputs that drive current flow up and down the pyramidal neuron dendrites (Fig. 8). These exogenous inputs were necessary to accurately reproduce 10- and 20-Hz components and distribution of the awake human SI mu rhythm.

Intuitively, one might predict that alternating 10-Hz inputs at a 50-ms delay would ideally combine to generate a 20-Hz MEG signal. However, our results suggest that the inputs must arrive nearly simultaneously (<10 ms) for 20-Hz cycles to emerge. In this case, approximately 10-Hz current flow that is driven up the pyramidal neuron dendrites (via FF input) is cut in half by current flow driven down the dendrites (via FB input) to create a 20-Hz cycle. With perfectly asynchronous (50-ms delay) FF and FB inputs, a dominant mu-alpha rhythm is produced. This result, and the fact that stronger FF inputs increase mu-alpha, whereas stronger FB inputs increase mu-beta (Fig. 8, *B–D*), leads to direct predictions as to the source of variability in mu-alpha or mu-beta expression across subjects (Fig. 3*B*). We may surmise that subjects with dominant mu-alpha components possess stronger rhythmic FF input and/or that the intracortical FB input arrives with a phase delay near 50 ms. In contrast, we predict that subjects with dominant mu-beta components possess stronger FB input and/or nearly perfectly aligned (<10-ms delay) FF and FB inputs.

Subthreshold oscillations and their relation to higher-frequency gamma rhythms

Several studies report that low-frequency alpha and/or beta range rhythms are directly coupled to higher-frequency gamma (40–80 Hz) rhythms. This effect has been observed in vivo in humans in electrocorticographic data (Canolty et al. 2006), MEG data (Palva et al. 2005a), and intracranial cortical LFP recordings (Lakatos et al. 2005; Schroeder and Lakatos 2009b). In our data, we do not see prominent gamma activity in the prestimulus time period (Fig. 3), likely due to the fact that our MEG signal measures the subthreshold synchronous activity of a large number of pyramidal neurons (Hamalainen et al. 1993; Zhu et al. 2009), estimated to be on the order of 6 million. Gamma rhythms are likely produced by a smaller subnetwork of spiking excitatory and inhibitory neurons (Cardin et al. 2009; Kopell et al. 2000; Pinto et al. 2003; Vierling-Claassen et al. 2008; Whittington et al. 2000) and are thus not recorded

in our signal. Further, due to the limited size of our network, the model cannot currently simultaneously reproduce both large- and small-scale phenomena.

Coordination of ongoing 10- and 20-Hz activity between brain areas

The prediction that the SI mu rhythm is driven by approximately 10-Hz rhythmic FF and FB in the model implies that the SI mu rhythm is correlated with 10-Hz activity in lemniscal thalamic sources (providing FF inputs), as well as in higher-order cortical sources (providing FB inputs) and/or nonlemniscal thalamic input. These hypotheses are consistent with several studies that report the existence of coherence in power (Schubert et al. 2008; Zhang and Ding 2009) and phase-locking (Hanslmayr et al. 2007; Palva et al. 2005a) between SI mu rhythms and alpha and beta frequency activity in prefrontal cortex and other higher-order cortical areas. Most significantly, Zhang and Ding (2009) recently applied Granger causality analysis to 10-Hz activity measured from EEG electrodes above somatosensory and prefrontal cortices and found that 10-Hz activity propagates from prefrontal cortex to SI. Palva et al. (2005) observed local cross-frequency phase synchrony between alpha- and beta-band oscillations widely across the cortex, particularly over the somatomotor regions, during rest conditions that increased with execution of mental arithmetic tasks (see also Nikulin and Brismar 2006). Interareal 10- to 10-Hz phase synchrony (and even more so 10- to 20-Hz synchrony) increased with task demands with the strongest effects at long distances. Hanslmayr et al. (2007) examined interareal within-frequency phase synchrony between EEG electrodes during a visual-perception task and found prestimulus alpha (8–12 Hz) phase synchrony mainly between frontal and parietal electrode sites that decreased with perception. Beta (20–30 Hz) phase synchrony was also observed and increased with perception. Schubert et al. (2008) used EEG during a somatosensory perceptual masking task and found that prestimulus beta activity (18–26 Hz) in prefrontal and sensorimotor electrodes covaried such that they were both lower during perceived trials. These results emphasize the cooperation of alpha- and beta-band activity across the brain and support the prediction that the SI mu rhythm may arise from rhythmic interactions of 10-Hz oscillations projected to SI in an FB manner from higher-order areas. However, our FB inputs could also arise from nonspecific thalamic inputs oscillating with a slight phase shift from that of the lemniscal driver nucleus (Guillery and Sherman 2002; Hughes and Crunelli 2005; Jones 2001). The prediction of near synchrony in inputs necessary to generate beta may be better explained by a common thalamic source, which may represent a different form of "feedback" or may represent a distinct form of input.

Symmetric oscillations and their relation to evoked responses

Our finding that the prestimulus SI mu rhythm oscillates symmetrically around zero is in contrast to previous studies that have observed nonsymmetric alpha-frequency oscillations that contribute to the generation of late (>250 ms) components of sensory-evoked responses. Nikulin et al. (2007) reported baseline shifts in mu-alpha frequency activity in sensorimotor MEG sensors on the scalp. These shifts in the mean of the oscillation over time were reported to be responsible for late (>250 ms) components of median nerve-evoked response. In another study, Mazaheri and Jensen (2008) observed asymmetric amplitude modulations in posterior alpha activity that was proposed to contribute to slow components (>300 ms) of visual-evoked responses over occipital cortex. Both studies conjectured that the baseline shifts and asymmetric oscillations were likely due to differences in outward and inward neural currents producing the magnetic field, which they posit are unlikely to be equal.

Our data and modeling results suggest that the net inward and outward current flow, within pyramidal neurons across the SI network, are approximately balanced, creating a symmetric index near zero in our signal (Fig. 6). The discrepancy between our results and those of Nikulin et al. (2007) and Mazaheri and Jensen (2008) may arise from several areas. These studies showed that differences in the later components of evoked sensory responses (>250 ms) were tied to asymmetry in the prestimulus alpha oscillation. In our study, we investigated only the evoked response components <175 ms. Notably, in our data there is a late trend (135–175 ms) to a larger MEG SI-evoked response under high prestimulus mu that was not reproduced by the model. We conjecture that this trend may arise from stronger poststimulus approximately 135-ms FF inputs to the network during high prestimulus mu conditions. This timing (~100 ms after the first evoked FF input arrives to the network) is consistent with the idea that there is also a stronger poststimulus evoked 10-Hz oscillation that is perhaps phase-locked (Hanslamayer et al. 2007; Makeig et al. 2002). Investigation of evoked poststimulus oscillations is not a focus of our study and we do not make any strong claims regarding these phenomena here.

Further, we studied activity localized to a primary equivalent current dipole in SI, whereas the other studies investigated sensor data. Both approaches have strengths. A benefit of dipole localization is that it provides a more concrete localization of a single signal source. Mazaheri and Jensen (2008) described the presence of a bipolar field pattern in their asymmetry index measure that was indicative of the existence of a current dipole located between the positive and negative signals. However, they did not investigate the location of the proposed dipole in the brain or find a consistent direction of the dipole current across subjects, from which inward and outward could be defined.

Last, we calculated the symmetry index of our signal across the entire frequency band of the SI mu rhythm complex (7–29 Hz), whereas the previous studies investigated asymmetries in activity from signals that had been band-passed in the alpha or beta range. Nikulin et al. (2007) used an independent component analysis to filter sensor data in the range of 8–13 Hz and investigated baseline shifts in the mean amplitude of the filtered signal. Inspection of our signal over long time periods (10 s) showed modulation of the mu rhythm without such a dc-offset effect (see METHODS). Mazaheri and Jensen (2008) band-passed their data using narrow width intervals from 5 to 40 Hz (e.g., 8–12 Hz for alpha activity) and found peaks and troughs in the band-passed data. The time points of the peak and trough values in the band-passed signal were used to calculate the peak and trough values in the original signal from which the symmetry index was calculated.

Our analysis methods for finding peaks and troughs in the data are analogous to those of Mazaheri and Jensen (2008). However, in Fig. 6 we quantified the symmetry index from peaks and troughs calculated from a broader band filter of our

signal that contained the entire mu range (5–30 Hz) (see METHODS). In an additional analysis, we quantified the symmetry index from calculated peaks and troughs in our signal by first band-passing in narrow width bands (3-Hz widths) from 5 to 40 Hz, precisely as in Mazaheri and Jensen (2008). We found the symmetry index to be significantly different from zero at only 5–7 Hz in that analysis of the data ($P = 0.03$, *t*-test; data not shown). However, closer inspection of the calculation of peaks and troughs from the data filtered in this small band showed that this is not the most accurate way to calculate these values in our signal. This method produced peaks and troughs that did not align with the true values in the raw data. In contrast, a band-pass that contained the entire mu range (5–30 Hz) produced precise alignment of peaks and troughs in the band-passed and raw data, thus providing a more accurate measure of symmetry in our signal. Supplemental Fig. S1 shows examples of single-trial (1-s) raw-data waveforms from the MEG and model SI signal, along with the band-passed versions of these signals in a narrow low-frequency band from 5 to 7 Hz (Supplemental Fig. S1, *A* and *C*) and in a band containing the entire mu range, 5–30 Hz (Supplemental Fig. S1, *B* and *D*).[1] Calculated peaks and troughs are shown on the band-passed and raw data with red and green asterisks, respectively. In the case of calculating the peaks and troughs from the 5- to 7-Hz filtered signals, the calculated peak and trough values do not line up with those apparent in the raw data and, in several instances, are flipped such that troughs are higher than peaks (Supplemental Fig. S1, *A* and *C*). In contrast, when calculating the peaks and troughs from the broader-band 5- to 30-Hz filtered signal, there is clear alignment between the calculated values and those in the raw data (Supplemental Fig. S1, *B* and *D*). The misalignment in peaks and troughs when using only a narrow low-frequency band is likely due to the fact that our SI dipole signal is a true two-component signal that contains prominent alpha and beta activity and band-passing the signal in a small frequency range distorts this fact. The observed misalignment in peaks and troughs would be less pronounced in signals that contained a predominantly 10-Hz oscillation, as in Mazaheri and Jensen (2008).

Motor gating of sensorimotor mu rhythms and somatosensory-evoked responses

Our study focuses on the sensorimotor mu rhythm and tactile-evoked responses exhibited by a primary current dipole localized to the hand representation of SI, without considering motor activity. Nevertheless, there is synergy between our results and the literature examining movement-induced decreases in sensorimotor mu rhythms and gating of somatosensory-evoked responses. Movement desynchronizes sensorimotor mu rhythms (Neuper et al. 2006; Pfurtscheller et al. 1997; Salenius et al. 1997). Several studies have also shown that limb and digit movements attenuate early components (≤45 ms) of electrically induced (typically median nerve) somatosensory-evoked potentials (Cheron and Borenstein 1987; Cohen and Starr 1987; Nishihira et al. 1997; Rossini et al. 1999; Rushton et al. 1981; Tapia et al. 1987). Direct electrophysiological recordings in animal models suggest that this attenuation is due to decreases in neuronal spiking activity, most probably of pyramidal neurons (Chapin and Woodward 1982; Ro et al. 2000). Rossini et al. (1999) used high-resolution EEG to localize this effect in human somatosensory, motor, and supplementary motor areas and found that in each area the gating effect was strongest at peaks between 30- and 45-ms post-nerve stimulation.

Our results show that decreased mu in SI predicts a decreased M50 peak, occurring with a maximum between 40- and 60-ms post-tactile stimulation. Our model predicts that this decrease is due to lower neuronal firing rates in SI pyramidal neurons (Fig. 8). The decreases in mu in our study are spontaneous and not directly related to motor movement; the attenuated peak occurs at a slightly longer latency than that in the described studies, likely due to the slower propagation time to the cortex from a brief tactile stimulation versus a strong electric stimulation to the nerve. However, the parallels in the two phenomena—decreased mu power predicting decreased evoked responses—suggest that similar circuits and mechanisms are common. In the following text we discuss how prestimulus mu-related changes in evoked activity may also be connected to facilitating detection of tactile-evoked responses.

Influence of the prestimulus mu rhythm on evoked response gain and implications for detection

In the present study, we intentionally excluded analysis of the impact of mu oscillations on detection. The focus of the present study was on mu—its rhythmogenesis and its impact on the evoked response—and the additional domain of relating these findings to perceptual success requires its own extensive treatment. Specifically, to determine the effects of mu power on the SI-evoked response, independent of perceptual success, trials were chosen to comprise a 50% detection rate for high and low mu conditions. That said, our results show that the changes in the evoked response driven by high or low mu conditions are different from those we showed in a previous study to predict detections. Our modeling results predicted that the ongoing mu rhythm influenced early components of the SI-evoked response (≤70 ms), with a weaker effect on later evoked activity ≤175 ms (Fig. 9*A*). This hypothesis was confirmed in the MEG data when sorting trials over high and low prestimulus mu power. Under high prestimulus mu conditions, a significant early M50 positive peak emerged, followed by a trend toward a weaker M70 response (Fig. 9*B*). In our previous study (Jones et al. 2007), we found that the later components of the SI-evoked response, beginning at about 70 ms (M70), were correlated with detection of a threshold-level tactile stimulus, such that the response magnitude was greater on detected trials. The model predicted that the late differences with detection reflected poststimulus changes in higher-order cortex or nonspecific thalamic projections that created earlier and stronger evoked FB at ≃70 ms and LFF input at ≃135 ms to SI on detected trials (see Jones et al. 2007). Several studies have reported a nearly inverse relationship between mu power and detection (Hanslmayr et al. 2007; Linkenkaer-Hansen et al. 2004; Schubert et al. 2008; Zhang and Ding 2009). In light of these findings, we may conjecture a possible relationship between low prestimulus rhythms in SI and "higher-order areas" on detected trials. Low-power ongoing rhythms in the higher-order area, producing weak ongoing approximately 10-Hz FB to SI, have greater early (<70 ms) poststimulus-evoked re-

[1] The online version of this article contains supplemental data.

sponses that in turn create greater FB to SI at nearly 70 ms on detected trials.

Conclusion

In summary, our study is the first to characterize the interdependence of the mu-alpha and mu-beta components of the SI MEG measured mu rhythm on single trials. Our computational model provides a novel mechanistic interpretation of the mu rhythm and its functional significance and presents the first evidence that the SI mu rhythm may arise from a stochastic nearly synchronous alternating sequence of approximately 10-Hz FF followed by FB input to the SI network. Importantly, specific predictions of our computational model are in agreement with the characteristics of the SI activity based on source modeling of our MEG data.

ACKNOWLEDGMENTS

We thank D. Ziegler and P. Hosseini-Varnamkhasti in the Brain and Cognitive Science Department at Massachusetts Institute of Technology for excellent technical support in implementation of data analysis methods, D. Vierling-Claassen and Q. Wan for thorough remarks on the manuscript, and M. Hines for continued support in NEURON software coding.

GRANTS

This work was supported by National Institutes of Health Grants P41-RR-14075, K25-MH-072941, 1RO1-NS-045130-01, and T32-GM-007484; National Science Foundation Grant 0316933; the Athinoula A. Martinos Center for Biomedical Imaging; and the McGovern Institute for Brain Research.

REFERENCES

Andersen P, Andersson SA. *Physiological Basis of the Alpha Rhythm*. New York: Appleton-Century-Crofts, 1968.

Barth DS, Di S. Laminar excitability cycles in neocortex. *J Neurophysiol* 65: 891–898, 1991.

Bauer M, Oostenveld R, Peeters M, Fries P. Tactile spatial attention enhances gamma-band activity in somatosensory cortex and reduces low-frequency activity in parieto-occipital areas. *J Neurosci* 26: 490–501, 2006.

Bollimunta A, Chen Y, Schroeder CE, Ding M. Neuronal mechanisms of cortical alpha oscillations in awake-behaving macaques. *J Neurosci* 28: 9976–9988, 2008.

Brovelli A, Ding M, Ledberg A, Chen Y, Nakamura R, Bressler SL. Beta oscillations in a large-scale sensorimotor cortical network: directional influences revealed by Granger causality. *Proc Natl Acad Sci USA* 101: 9849–9854, 2004.

Buschman TJ, Miller EK. Top-down versus bottom-up control of attention in the prefrontal and posterior parietal cortices. *Science* 315: 1860–1862, 2007.

Bush PC, Sejnowski TJ. Reduced compartmental models of neocortical pyramidal cells. *J Neurosci Methods* 46: 159–166, 1993.

Canolty RT, Edwards E, Dalal SS, Soltani M, Nagarajan SS, Kirsch HE, Berger MS, Barbaro NM, Knight RT. High gamma power is phase-locked to theta oscillations in human neocortex. *Science* 313: 1626–1628, 2006.

Cardin JA, Carlen M, Meletis K, Knoblich U, Zhang F, Deisseroth K, Tsai LH, Moore CI. Driving fast-spiking cells induces gamma rhythm and controls sensory responses. *Nature* 459: 663–667, 2009.

Castro-Alamancos MA, Connors BW. Spatiotemporal properties of short-term plasticity sensorimotor thalamocortical pathways of the rat. *J Neurosci* 16: 2767–2779, 1996.

Cauller LJ, Clancy B, Connors BW. Backward cortical projections to primary somatosensory cortex in rats extend long horizontal axons in layer I. *J Comp Neurol* 390: 297–310, 1998.

Cauller LJ, Connors BW. Synaptic physiology of horizontal afferents to layer I in slices of rat SI neocortex. *J Neurosci* 14: 751–762, 1994.

Cauller LJ, Kulics AT. The neural basis of the behaviorally relevant N1 component of the somatosensory-evoked potential in SI cortex of awake monkeys: evidence that backward cortical projections signal conscious touch sensation. *Exp Brain Res* 84: 607–619, 1991.

Chapin JK, Woodward DJ. Somatic sensory transmission to the cortex during movement: gating of single cell responses to touch. *Exp Neurol* 78: 654–669, 1982.

Cheron G, Borenstein S. Specific gating of the early somatosensory evoked potentials during active movement. *Electroencephalogr Clin Neurophysiol* 67: 537–548, 1987.

Cheung AF, Pollen AA, Tavare A, DeProto J, Molnar Z. Comparative aspects of cortical neurogenesis in vertebrates. *J Anat* 211: 164–176, 2007.

Cohen LG, Starr A. Localization, timing and specificity of gating of somatosensory evoked potentials during active movement in man. *Brain* 110: 451–467, 1987.

Contreras D, Steriade M. Cellular basis of EEG slow rhythms: a study of dynamic corticothalamic relationships. *J Neurosci* 15: 604–622, 1995.

Dai H. On measuring psychometric functions: a comparison of the constant-stimulus and adaptive up-down methods. *J Acoust Soc Am* 98: 3135–3139, 1995.

Di S, Baumgartner C, Barth DS. Laminar analysis of extracellular field potentials in rat vibrissa/barrel cortex. *J Neurophysiol* 63: 832–840, 1990.

Donner TH, Siegel M, Oostenveld R, Fries P, Bauer M, Engel AK. Population activity in the human dorsal pathway predicts the accuracy of visual motion detection. *J Neurophysiol* 98: 345–359, 2007.

Douglas RJ, Martin KA. Neuronal circuits of the neocortex. *Annu Rev Neurosci* 27: 419–451, 2004.

Fanselow EE, Richardson KA, Connors BW. Selective, state-dependent activation of somatostatin-expressing inhibitory interneurons in mouse neocortex. *J Neurophysiol* 100: 2640–2652, 2008.

Felleman DJ, Van Essen DC. Distributed hierarchical processing in the primate cerebral cortex. *Cereb Cortex* 1: 1–47, 1991.

Friedman DP, Jones EG. Focal projection of electrophysiologically defined groupings of thalamic cells on the monkey somatic sensory cortex. *Brain Res* 191: 249–252, 1980.

Friedman DP, Jones EG, Burton H. Representation pattern in the second somatic sensory area of the monkey cerebral cortex. *J Comp Neurol* 192: 21–41, 1980.

Gaetz W, Cheyne D. Localization of sensorimotor cortical rhythms induced by tactile stimulation using spatially filtered MEG. *Neuroimage* 30: 899–908, 2006.

Galaburda A, Rosen G, Sherman G. Individual variability in cortical organization: its relationship to brain laterality and implications for function. *Neuropsychologica* 28: 529–546, 1990.

Giove F, Mangia S, Bianciardi M, Garreffa G, Di Salle F, Morrone R, Maraviglia B. The physiology and metabolism of neuronal activation: in vivo studies by NMR and other methods. *Magn Reson Imaging* 21: 1283–1293, 2003.

Guillery RW, Sherman SM. Thalamic relay functions and their role in corticocortical communication: generalizations from the visual system. *Neuron* 33: 163–175, 2002.

Hamalainen M, Hari R, Ilmoniemi RJ, Knuutila J, Lounasmaa OV. Magnetoencephalography: theory, instrumentation, and applications to noninvasive studies of the working human brain. *Rev Mod Phys* 65: 413–497, 1993.

Hamalainen MS, Sarvas J. Realistic conductivity geometry model of the human head for interpretation of neuromagnetic data. *IEEE Trans Biomed Eng* 36: 165–171, 1989.

Hanslmayr S, Aslan A, Staudigl T, Klimesch W, Herrmann CS, Bauml KH. Prestimulus oscillations predict visual perception performance between and within subjects. *Neuroimage* 37: 1465–1473, 2007.

Hari R, Aittoniemi K, Jarvinen ML, Katila T, Varpula T. Auditory evoked transient and sustained magnetic fields of the human brain. Localization of neural generators. *Exp Brain Res* 40: 237–240, 1980.

Hari R, Salmelin R. Human cortical oscillations: a neuromagnetic view through the skull. *Trends Neurosci* 20: 44–49, 1997.

Hughes SW, Crunelli V. Thalamic mechanisms of EEG alpha rhythms and their pathological implications. *Neuroscientist* 11: 357–372, 2005.

Ikeda H, Wang Y, Okada YC. Origins of the somatic N20 and high-frequency oscillations evoked by trigeminal stimulation in the piglets. *Clin Neurophysiol* 116: 827–841, 2005.

Jackson ME, Cauller LJ. Neural activity in SII modifies sensory evoked potentials in SI in awake rats. *Neuroreport* 9: 3379–3382, 1998.

Jensen O, Gelfand J, Kounios J, Lisman JE. Oscillations in the alpha band (9–12 Hz) increase with memory load during retention in a short-term memory task. *Cereb Cortex* 12: 877–882, 2002.

Jones EG. Connectivity of the primary sensory-motor cortex. In: *Cerebral Cortex Sensory-Motor Areas and Aspects of Cortical Connectivity*, edited by Jones EG, Peters A. New York: Plenum, 1986, p. 113–183.

Jones EG. The thalamic matrix and thalamocortical synchrony. *Trends Neurosci* 24: 595–601, 2001.

Jones SR, Pinto DJ, Kaper TJ, Kopell N. Alpha-frequency rhythms desynchronize over long cortical distances: a modeling study. *J Comput Neurosci* 9: 271–291, 2000.

Jones SR, Pritchett DL, Stufflebeam SM, Hamalainen M, Moore CI. Neural correlates of tactile detection: a combined MEG and biophysically based computational modeling study. *J Neurosci* 27: 10751–10764, 2007.

Kaas JH, Garraghty PE. Hierarchical, parallel, and serial arrangements of sensory cortical areas: connection patterns and functional aspects. *Curr Opin Neurobiol* 1: 248–251, 1991.

Kandel A, Buzsáki G. Cellular-synaptic generation of sleep spindles, spike-and-wave discharges, and evoked thalamocortical responses in the neocortex of the rat. *J Neurosci* 17: 6783–6797, 1997.

Kelly SP, Lalor EC, Reilly RB, Foxe JJ. Increases in alpha oscillatory power reflect an active retinotopic mechanism for distracter suppression during sustained visuospatial attention. *J Neurophysiol* 95: 3844–3851, 2006.

Kole MH, Hallermann S, Stuart GJ. Single Ih channels in pyramidal neuron dendrites: properties, distribution, and impact on action potential output. *J Neurosci* 26: 1677–1687, 2006.

Kopell N, Ermentrout GB, Whittington MA, Traub RD. Gamma rhythms and beta rhythms have different synchronization properties. *Proc Natl Acad Sci USA* 97: 1867–1872, 2000.

Kramer MA, Roopun AK, Carracedo LM, Traub RD, Whittington MA, Kopell NJ. Rhythm generation through period concatenation in rat somatosensory cortex. *PLoS Comput Biol* 4: e1000169, 2008.

Kuhlman WN. Functional topography of the human mu rhythm. *Electroencephalogr Clin Neurophysiol* 44: 83–93, 1978.

Kulics AT. Cortical neural evoked correlates of somatosensory stimulus detection in the rhesus monkey. *Electroencephalogr Clin Neurophysiol* 53: 78–93, 1982.

Kulics AT, Cauller LJ. Cerebral cortical somatosensory evoked responses, multiple unit activity and current source-densities: their interrelationships and significance to somatic sensation as revealed by stimulation of the awake monkey's hand. *Exp Brain Res* 62: 46–60, 1986.

Lakatos P, Shah AS, Knuth KH, Ulbert I, Karmos G, Schroeder CE. An oscillatory hierarchy controlling neuronal excitability and stimulus processing in the auditory cortex. *J Neurophysiol* 94: 1904–1911, 2005.

Leek MR. Adaptive procedures in psychophysical research. *Percept Psychophys* 63: 1279–1292, 2001.

Linkenkaer-Hansen K, Nikulin VV, Palva S, Ilmoniemi RJ, Palva JM. Prestimulus oscillations enhance psychophysical performance in humans. *J Neurosci* 24: 10186–10190, 2004.

Lipton ML, Fu KM, Branch CA, Schroeder CE. Ipsilateral hand input to area 3b revealed by converging hemodynamic and electrophysiological analyses in macaque monkeys. *J Neurosci* 26: 180–185, 2006.

Llinás R, Ribary U. Consciousness and the brain. The thalamocortical dialogue in health and disease. *Ann NY Acad Sci* 929: 166–175, 2001.

Makeig S, Westerfield M, Jung TP, Enghoff S, Townsend J, Courchesne E, Sejnowski TJ. Dynamic brain sources of visual evoked responses. *Science* 295: 690–694, 2002.

Mathewson KE, Gratton G, Fabiani M, Beck DM, Ro T. To see or not to see: prestimulus alpha phase predicts visual awareness. *J Neurosci* 29: 2725–2732, 2009.

Mazaheri A, Jensen O. Asymmetric amplitude modulations of brain oscillations generate slow evoked responses. *J Neurosci* 28: 7781–7787, 2008.

Mazaheri A, Nieuwenhuis IL, van Dijk H, Jensen O. Prestimulus alpha and mu activity predicts failure to inhibit motor responses. *Hum Brain Mapp* 30: 1791–1800, 2009.

Moore CI, Stern CE, Corkin S, Fischl B, Gray AC, Rosen BR, Dale AM. Segregation of somatosensory activation in the human rolandic cortex using fMRI. *J Neurophysiol* 84: 558–569, 2000.

Neuper C, Wortz M, Pfurtscheller G. ERD/ERS patterns reflecting sensorimotor activation and deactivation. *Prog Brain Res* 159: 211–222, 2006.

Nikouline VV, Wikstrom H, Linkenkaer-Hansen K, Kesaniemi M, Ilmoniemi RJ, Huttunen J. Somatosensory evoked magnetic fields: relation to pre-stimulus mu rhythm. *Clin Neurophysiol* 111: 1227–1233, 2000.

Nikulin VV, Brismar T. Phase synchronization between alpha and beta oscillations in the human electroencephalogram. *Neuroscience* 137: 647–657, 2006.

Nikulin VV, Linkenkaer-Hansen K, Nolte G, Lemm S, Muller KR, Ilmoniemi RJ, Curio G. A novel mechanism for evoked responses in the human brain. *Eur J Neurosci* 25: 3146–3154, 2007.

Nishihira Y, Araki H, Funase K, Imanaka K. Selective modification of somatosensory evoked potential during voluntary finger movement in humans. *Percept Mot Skills* 85: 259–266, 1997.

Nishitani N, Hari R. Temporal dynamics of cortical representation for action. *Proc Natl Acad Sci USA* 97: 913–918, 2000.

Okada YC, Wu J, Kyuhou S. Genesis of MEG signals in a mammalian CNS structure. *Electroencephalogr Clin Neurophysiol* 103: 474–485, 1997.

Palva JM, Palva S, Kaila K. Phase synchrony among neuronal oscillations in the human cortex. *J Neurosci* 25: 3962–3972, 2005a.

Palva S, Linkenkaer-Hansen K, Naatanen R, Palva JM. Early neural correlates of conscious somatosensory perception. *J Neurosci* 25: 5248–5258, 2005b.

Penfield W, Rasmussen T. *The Cerebral Cortex of Man: A Clinical Study of Localization and Function*. New York: Macmillan, 1950.

Peterson NN, Schroeder CE, Arezzo JC. Neural generators of early cortical somatosensory evoked potentials in the awake monkey. *Electroencephalogr Clin Neurophysiol* 96: 248–260, 1995.

Pfurtscheller G, Neuper C, Andrew C, Edlinger G. Foot and hand area mu rhythms. *Int J Psychophysiol* 26: 121–135, 1997.

Pineda JA. The functional significance of mu rhythms: translating "seeing" and "hearing" into "doing." *Brain Res Brain Res Rev* 50: 57–68, 2005.

Pinto DJ, Jones SR, Kaper TJ, Kopell N. Analysis of state-dependent transitions in frequency and long-distance coordination in a model oscillatory cortical circuit. *J Comput Neurosci* 15: 283–298, 2003.

Ro JY, Debowy D, Ghosh S, Gardner EP. Depression of neuronal firing rates in somatosensory and posterior parietal cortex during object acquisition in a prehension task. *Exp Brain Res* 135: 1–11, 2000.

Rockland KS, Pandya DN. Laminar origins and terminations of cortical connections of the occipital lobe in the rhesus monkey. *Brain Res* 179: 3–20, 1979.

Roelfsema PR, Engel AK, Konig P, Singer W. Visuomotor integration is associated with zero time-lag synchronization among cortical areas. *Nature* 385: 157–161, 1997.

Roopun AK, Kramer MA, Carracedo LM, Kaiser M, Davies CH, Traub RD, Kopell NJ, Whittington MA. Period concatenation underlies interactions between gamma and beta rhythms in neocortex (Abstract). *Front Cell Neurosci* 2: 1, 2008.

Roopun AK, Middleton SJ, Cunningham MO, LeBeau FE, Bibbig A, Whittington MA, Traub RD. A beta2-frequency (20–30 Hz) oscillation in nonsynaptic networks of somatosensory cortex. *Proc Natl Acad Sci USA* 103: 15646–15650, 2006.

Rossini PM, Babiloni C, Babiloni F, Ambrosini A, Onorati P, Carducci F, Urbano A. "Gating" of human short-latency somatosensory evoked cortical responses during execution of movement. A high resolution electroencephalography study. *Brain Res* 843: 161–170, 1999.

Rushton DN, Rothwell JC, Craggs MD. Gating of somatosensory evoked potentials during different kinds of movement in man. *Brain* 104: 465–491, 1981.

Salenius S, Schnitzler A, Salmelin R, Jousmaki V, Hari R. Modulation of human cortical rolandic rhythms during natural sensorimotor tasks. *Neuroimage* 5: 221–228, 1997.

Salmelin R, Hamalainen M, Kajola M, Hari R. Functional segregation of movement-related rhythmic activity in the human brain. *Neuroimage* 2: 237–243, 1995.

Salmelin R, Hari R. Spatiotemporal characteristics of sensorimotor neuromagnetic rhythms related to thumb movement. *Neuroscience* 60: 537–550, 1994.

Sarvas J. Basic mathematical and electromagnetic concepts of the biomagnetic inverse problem. *Phys Med Biol* 32: 11–22, 1987.

Sastre-Janer FA, Regis J, Belin P, Mangin JF, Dormont D, Masure MC, Remy P, Frouin V, Samson Y. Three-dimensional reconstruction of the human central sulcus reveals a morphological correlate of the hand area. *Cereb Cortex* 8: 641–647, 1998.

Schroeder CE, Lakatos P. Low-frequency neuronal oscillations as instruments of sensory selection. *Trends Neurosci* 32: 9–18, 2009a.

Schroeder CE, Lakatos P. The gamma oscillation: master or slave? *Brain Topogr* 22: 24–26, 2009b.

Schubert R, Haufe S, Blankenburg F, Villringer A, Curio G. Now you'll feel it, now you won't: EEG rhythms predict the effectiveness of perceptual masking. *J Cogn Neurosci* 21: 2407–2419, 2008.

Sherman SM. Thalamic relays and cortical functioning. *Prog Brain Res* 149: 107–126, 2005.

Silva LR, Amitai Y, Connors BW. Intrinsic oscillations of neocortex generated by layer 5 pyramidal neurons. *Science* 251: 432–435, 1991.

Suffczynski P, Kalitzin S, Pfurtscheller G, Lopes da Silva FH. Computational model of thalamo-cortical networks: dynamical control of alpha rhythms in relation to focal attention. *Int J Psychophysiol* 43: 25–40, 2001.

Szurhaj W, Derambure P, Labyt E, Cassim F, Bourriez JL, Isnard J, Guieu JD, Mauguière F. Basic mechanisms of central rhythms reactivity to preparation and execution of a voluntary movement: a stereoelectroencephalographic study. *Clin Neurophysiol* 114: 107–119, 2003.

Tallon-Baudry C, Bertrand O, Delpuech C, Permier J. Oscillatory gamma-band (30–70 Hz) activity induced by a visual search task in humans. *J Neurosci* 17: 722–734, 1997.

Tapia MC, Cohen LG, Starr A. Selectivity of attenuation (i.e., gating) of somatosensory potentials during voluntary movement in humans. *Electroencephalogr Clin Neurophysiol* 68: 226–230, 1987.

Tesche CD, Uusitalo MA, Ilmoniemi RJ, Huotilainen M, Kajola M, Salonen O. Signal-space projections of MEG data characterize both distributed and well-localized neuronal sources. *Electroencephalogr Clin Neurophysiol* 95: 189–200, 1995.

Thomson AM, West DC, Wang Y, Bannister AP. Synaptic connections and small circuits involving excitatory and inhibitory neurons in layers 2–5 of adult rat and cat neocortex: triple intracellular recordings and biocytin labelling in vitro. *Cereb Cortex* 12: 936–953, 2002.

Tiihonen J, Kajola M, Hari R. Magnetic mu rhythm in man. *Neuroscience* 32: 793–800, 1989.

Traub RD, Contreras D, Cunningham MO, Murray H, LeBeau FE, Roopun A, Bibbig A, Wilent WB, Higley MJ, Whittington MA. Single-column thalamocortical network model exhibiting gamma oscillations, sleep spindles, and epileptogenic bursts. *J Neurophysiol* 93: 2194–2232, 2005.

Uematsu S, Lesser RP, Gordon B. Localization of sensorimotor cortex: the influence of Sherrington and Cushing on the modern concept. *Neurosurgery* 30: 904–913, 1992.

Uusitalo MA, Ilmoniemi RJ. Signal-space projection method for separating MEG or EEG into components. *Med Biol Eng Comput* 35: 135–140, 1997.

van Wijk BC, Daffertshofer A, Roach N, Praamstra P. A role of beta oscillatory synchrony in biasing response competition? *Cereb Cortex* 19: 1294–1302, 2009.

Vierling-Claassen D, Siekmeier P, Stufflebeam S, Kopell N. Modeling GABA alterations in schizophrenia: a link between impaired inhibition and altered gamma and beta range auditory entrainment. *J Neurophysiol* 99: 2656–2671, 2008.

von Stein A, Chiang C, Konig P. Top-down processing mediated by interareal synchronization. *Proc Natl Acad Sci USA* 97: 14748–14753, 2000.

White LE, Andrews TJ, Hulette C, Richards A, Groelle M, Paydarfar J, Purves D. Structure of the human sensorimotor system. I. Morphology and cytoarchitecture of the central sulcus. *Cereb Cortex* 7: 18–30, 1997.

Whittington MA, Traub RD, Kopell N, Ermentrout B, Buhl EH. Inhibition-based rhythms: experimental and mathematical observations on network dynamics. *Int J Psychophysiol* 38: 315–336, 2000.

Wilke M, Logothetis NK, Leopold DA. Local field potential reflects perceptual suppression in monkey visual cortex. *Proc Natl Acad Sci USA* 103: 17507–17512, 2006.

Witham CL, Baker SN. Network oscillations and intrinsic spiking rhythmicity do not covary in monkey sensorimotor areas. *J Physiol* 580: 801–814, 2007.

Witham CL, Wang M, Baker SN. Cells in somatosensory areas show synchrony with beta oscillations in monkey motor cortex. *Eur J Neurosci* 26: 2677–2686, 2007.

Worden MS, Foxe JJ, Wang N, Simpson GV. Anticipatory biasing of visuospatial attention indexed by retinotopically specific alpha-band electroencephalography increases over occipital cortex. *J Neurosci* 20: RC63, 2000.

Yousry TA, Schmid UD, Alkadhi H, Schmidt D, Peraud A, Buettner A, Winkler P. Localization of the motor hand area to a knob on the precentral gyrus. A new landmark. *Brain* 120: 141–157, 1997.

Zhang Y, Ding M. Detection of a weak somatosensory stimulus: role of the prestimulus mu rhythm and its top-down modulation. *J Cogn Neurosci* (April 28, 2009). doi:10.1162/jocn.2009.21247.

Zhu Z, Zumer JM, Lowenthal ME, Padberg J, Recanzone GH, Krubitzer LA, Nagarajan SS, Disbrow EA. The relationship between magnetic and electrophysiological responses to complex tactile stimuli (Abstract). *BMC Neurosci* 10: 4, 2009.

Behavioral/Systems/Cognitive

Cued Spatial Attention Drives Functionally Relevant Modulation of the Mu Rhythm in Primary Somatosensory Cortex

Stephanie R. Jones,[1]* Catherine E. Kerr,[2]* Qian Wan,[2,3] Dominique L. Pritchett,[3] Matti Hämäläinen,[1] and Christopher I. Moore[3]

[1]Athinoula A. Martinos Center for Biomedical Imaging, Massachusetts General Hospital, Charlestown, Massachusetts 02129, [2]Harvard Osher Research Center, Harvard Medical School, Boston, Massachusetts 02215, and [3]McGovern Institute for Brain Research, Massachusetts Institute of Technology, Cambridge, Massachusetts 02139

Cued spatial attention modulates functionally relevant alpha rhythms in visual cortices in humans. Here, we present evidence for analogous phenomena in primary somatosensory neocortex (SI). Using magnetoencephalography, we measured changes in the SI mu rhythm containing mu-alpha (7–14 Hz) and mu-beta (15–29 Hz) components. We found that cued attention impacted mu-alpha in the somatopically localized hand representation in SI, showing decreased power after attention was cued to the hand and increased power after attention was cued to the foot, with significant differences observed 500–1100 ms after cue. Mu-beta showed differences in a time window 800–850 ms after cue. The visual cue also drove an early evoked response beginning ~70 ms after cue with distinct peaks modulated with cued attention. Distinct components of the tactile stimulus-evoked response were also modulated with cued attention. Analysis of a second dataset showed that, on a trial-by-trial basis, tactile detection probabilities decreased linearly with prestimulus mu-alpha and mu-beta power. These results support the growing consensus that cue-induced alpha modulation is a functionally relevant sensory gating mechanism deployed by attention. Further, while cued attention had a weaker effect on the allocation of mu-beta, oscillations in this band also predicted tactile detection.

Introduction

The historical view of electroencephalography/magnetoencephalography (EEG/MEG)-measured alpha rhythms (7–14 Hz) as a "resting" brain state is being challenged by evidence that they are actively and topographically deployed to gate information processing. Cued spatial attention leads to decreased alpha amplitudes in parietal-occipital EEG sensors contralateral to the attended site in visual (Worden et al., 2000; Kelly et al., 2006, 2009; Thut et al., 2006) and intersensory visual–auditory (Foxe et al., 1998; Fu et al., 2001) tasks. Alpha decreases are accompanied by increases in opposing hemifields, and lateralized alpha amplitudes predict reaction times and visual discriminability (Worden et al., 2000; Kelly et al., 2006, 2009; Thut et al., 2006). Recent work has also shown that attentional biases are tied to changes in components of the broadband cue-induced evoked response (ER) in early visual cortices (Kelly et al., 2009).

In the somatosensory neocortex in humans, a spontaneous mu rhythm containing a complex of mu-alpha (7–14 Hz) and mu-beta (15–29 Hz) components is commonly observed above rolandic cortex (Tiihonen et al., 1989; Jones et al., 2009). These rhythms show an event-related desynchronization (ERD) with stimulation or movement, and in premovement periods, with a subsequent synchronization (ERS). There is an increase in alpha-band ERS over the sensorimotor neocortex during visual processing, with a simultaneous alpha ERD over visual cortices, and vice versa during movement (Pfurtscheller, 1992) (see also Rougeul et al., 1979). Further, premovement alpha ERD is accentuated in elite athletes over the entire brain, suggesting that this is a functionally relevant mechanism that can be enhanced with practice (Del Percio et al., 2009).

Several studies have shown that selective somatic attention impacts movement- or sensory-induced ERD and ERS changes in sensorimotor mu-alpha and mu-beta activity (Bauer et al., 2006; Babiloni et al., 2008; Dockstader et al., 2010). However, allocation of these rhythms following an attentional cue, in anticipation of tactile sensory processing, has not been investigated.

In the present study, we used MEG imaging to investigate whether similar effects to those observed in the visual system are also present in somatosensation, using the well localized hand representation in SI as our substrate (Jones et al., 2007, 2009). We investigated whether spatial attention directed to or away from

Received June 10, 2010; revised Aug. 2, 2010; accepted Aug. 12, 2010.

This work was supported by the National Institutes of Health (P41RR14075, K25MH072941, K01AT003459, 1R01-NS045130-01, and T32 GM007484), the National Science Foundation (0316933), and the Osher Institute. We thank the anonymous reviewers for particularly thoughtful comments on earlier drafts of this manuscript and the Athinoula A. Martinos Center for Biomedical Imaging and the McGovern Institute for Brain Research for their support of this research.

*S.R.J. and C.E.K. contributed equally to this work.

Correspondence should be addressed to Stephanie R. Jones, Athinoula A. Martinos Center for Biomedical Imaging, Massachusetts General Hospital, 149 13th Street, Suite 2301, Charlestown, MA 02129. E-mail: srjones@nmr.mgh.harvard.edu.

DOI:10.1523/JNEUROSCI.2969-10.2010

 0270-6474/10/3013760-06$15.00/0

the hand impacted allocation of mu-alpha and mu-beta, the predictive value of these rhythms for detection, and the impact of cued attention on evoked responses. We observed an impact in each of these dimensions, indicating that the decreased expression of localized alpha oscillations could be causally beneficial to attentional regulation employed across neocortical areas.

Materials and Methods

Subjects

MEG data were collected from 12 neurologically healthy (exclusion criteria included musculoskeletal diseases, arthritis, lupus, multiple sclerosis, scleroderma, and diagnosed current psychiatric disorder), right-handed, 18- to 50-year-old adults (mean age = 31.6 years, SD = 7 years, 1 male and 11 female). Subjects were medication free or on stable doses of selective serotonin reuptake inhibitor medication. The experimental protocol was approved by the Massachusetts General Hospital Internal Review Board, and each subject gave informed consent before data acquisition.

Stimuli

Subjects' hand and foot rested on solid plastic frames through which tactile stimuli were delivered. The stimulus (single cycle of a 100 Hz sine wave, 10 ms duration) was generated by fused multilayer piezoelectric benders, which provide more favorable force and higher-frequency resonance characteristics than typical ceramic wafers (Noliac) (see Jones et al., 2007). Stimuli were applied to the distal pads of the third digit of the left hand and first digit of the left foot via a Delrin contactor affixed to the piezoelectric bender (7 mm diameter presented within a 1 cm circular rigid surround). The device was not glued to the skin. Instead, matched intensity of stimulation, relative to perceptual threshold, was maintained individually for each subject using a parameter estimation sequential testing (PEST) convergence procedure (Dai, 1995; Leek, 2001). During the cued detection runs described below, stimulus strength was maintained at 66% detection threshold with suprathreshold (100% detected) and null stimuli randomly interleaved for 10% and 20% of the trials, respectively. The PEST procedure and the hand stimulation device and protocol were as used by Jones et al. (2007, 2009).

Experimental procedure

Localization runs. To aid localization of primary equivalent current dipoles (ECDs) in contralateral SI, each experiment began with presentation of suprathreshold stimuli to the left hand third digit for 3 min with an interstimulus interval of 3 s (60 trials per subject). Separate localization runs were also performed on the first digit of the foot, as an original goal of our study was to look at the somatotopic precision of attention allocation by comparing hand and foot activity. However, consistent dipoles could not be reconstructed from the foot localization data using the standard ECD localization techniques described below. Thus, only hand area activity is presented, as its precise position in the SI map could be confirmed.

Cued detection runs. Subjects were instructed to fixate on a cross on a projection screen. PEST procedure was used for 3 min at the beginning to determine subjects' initial detection thresholds. This run was followed by at least 5 cued detection runs, described in Figure 1, consisting of a 3.5 s trial that began with the fixation cross changing into a visual word cue on a projection screen directing the participant to attend to the "Hand" (the attend-in condition), the "Foot" (the attend-out condition), or "Either" location. The visual cue was accompanied by a 60 dB, 2 kHz tone delivered to both ears to mask audible clicks created by the tactile stimulator and remained constant for 2.5 s. At a randomized time between 1.1 and 2.1 s (fixed 100 ms intervals) after the visual cue, the piezoelectric stimulator delivered a brief tactile stimulus to either the finger or toe. At the end of the 2.5 s visual cue, and at least 400 ms after tactile stimulus, subjects reported detection or nondetection of the stimulus at the cued location with button presses using the second and third digits of the right hand, respectively. The next trial began 1 s after cessation of the visual cue. There were 120 trials per run, 40 of each attention condition, totaling at least 200 trials of 3 stimulus strengths in each condition.

MEG data acquisition and source analysis. The MEG signals were recorded using a 306-channel whole-head planar dc-SQUID Neuromag Vectorview system. Data were acquired at 601 Hz and filtered from 0.1 to 200 Hz. Four head position coils recorded head position in the Dewar for coregistration with structural MR images. Vertical and horizontal electro-oculogram (EOG) signals were recorded with electrodes placed close to the left eye. Epochs with EOG peak-to-peak amplitude exceeding 100 μV were excluded from analysis.

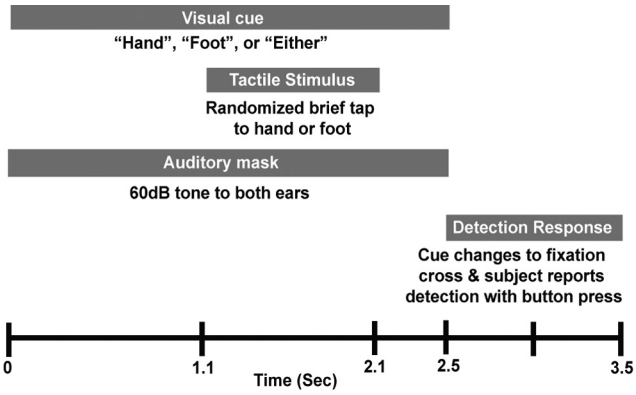

Figure 1. Experimental design for cued detection runs. See Materials and Methods.

The contribution from the left third digit representation in SI to the measured fields was estimated using a least-squares fit with a dipole forward solution calculated using a spherically symmetric conductor model of the head (Hämäläinen and Sarvas, 1989). Averaged data from the localization runs described above were used to find an ECD (Elekta-Neuromag software) at the time of peak activity (mean peak activity = 66.8 ms, SD = 6.4 ms) in the mean signal from the suprathreshold stimuli (minimum $n = 50$ runs per subject). The goodness of fit of this single dipole model was larger than 70% in all fit data during peak responses. Coregistration of the SI source localization with the individual's anatomical MRIs confirmed that the source emerged from the anterior band of the postcentral gyrus finger representation of area 3b in SI (Moore et al., 2000) in all subjects (see Fig. 2*A*). All analysis considered the forward solution from this SI source.

Analysis

Time evolution of spectral power. This metric was calculated using a complex wavelet analysis, from which time–frequency representations (TFRs) of near instantaneous changes were determined. The TFRs were calculated from 1 to 40 Hz on the SI ECD time courses by convolving signals with a complex Morlet wavelet of the form $w(t, f_0) = A \exp(-t^2/2[\sigma_t^2])\exp(2i\pi f_0 t)$, for each frequency of interest f_0, where $\sigma_t = m/2\pi f_0$, and i is the imaginary unit. The normalization factor was $A = 1/(\sigma_t\sqrt{2\pi})$, and the constant m defining the compromise between time and frequency resolution was 7, as in the Jones et al. (2009) study. Time–frequency representations of mu-alpha and mu-beta power were calculated as the squared magnitude of the complex wavelet-transformed data averaged across the range of interest. For the postcue analysis (see Fig. 2*B*), baseline was calculated as averaged power [−200, 0] ms relative to the cue—averaged across attend-in and attend-out trials separately. For the prestimulus analysis (see Fig. 2*C*), baseline was calculated as average power [−500, 0] ms relative to the stimulus.

Data were analyzed using the last 100 trials of each condition. This choice reflects preliminary analysis across multiple studies in our laboratory (S. R. Jones and C. I. Moore, unpublished data) indicating that the initial 100 trials provide less stable and consistent neurophysiological activity patterns across individuals.

Visual cue and tactile stimulus broadband evoked responses. SI evoked responses were calculated across an equal number of attend-in and attend-out trials per subject from threshold-level tactile stimulation to the finger (number of trials mean = 88 trials; SD = 10). Averages were baseline normalized by subtracting the mean over [−100, 0] ms from the cue or stimulus, for each subject (see Fig. 3). A response artifact from 1.7 to 2.1 s in one subject was removed from Figure 3*A*.

Impact of mu-alpha and mu-beta on detection probabilities. We could not use the current data to assess the impact of mu-alpha and mu-beta on detection probabilities because the subset of relevant data was a statistically small sample. The relevant data consisted of the "hit" and "miss" trials in the attend-hand condition, and there were only a small number of miss trials per subject in this subcondition (number of miss trials: mean = 11, SD = 6; number of hit trials: mean = 83, SD = 11). Therefore, we conducted analysis using a second dataset where the statistics were tractable. As in the present study, subjects detected taps applied to the third digit fingertip (of the right hand) using the same stimulator, and signals were localized to the hand dipole using identical means. Because foot trials and "either" trials were not interleaved—subjects attended to the hand throughout—we had a more extensive trial base for comparing hit and miss trials (last 100 trials analyzed). Details of data collection were described in detail in prior reports by our group (Jones et al., 2007, 2009; Ziegler et al., 2010).

Analysis methods were as in the Linkenkaer-Hansen et al. (2004) study. In brief, for each subject mu-alpha and mu-beta power was averaged over a 1 s prestimulus time window for each of the last 100 threshold-level stimulus trials, and binned into 10 power percentile bins (10 averages per bin) sorted from low to high. The probability of detection in each bin was calculated as a percentage change in hit rate (number of detected trials/total number of trials) from the mean (see Fig. 4).

Statistical analyses. Nonparametric Wilcoxon sign-rank tests were used to assess the statistical significance of differences in attend-in and attend-out conditions across subjects at every time point (see Figs. 2*B*,*C*, 3). The Wilcoxon test was preferred over ANOVA because the data were non-normally distributed (Shapiro–Wilks test). Linear regression on the mean percentage change in hit rate across subjects was used to assess the impact of mu-alpha and mu-beta power on detection (see Fig. 4).

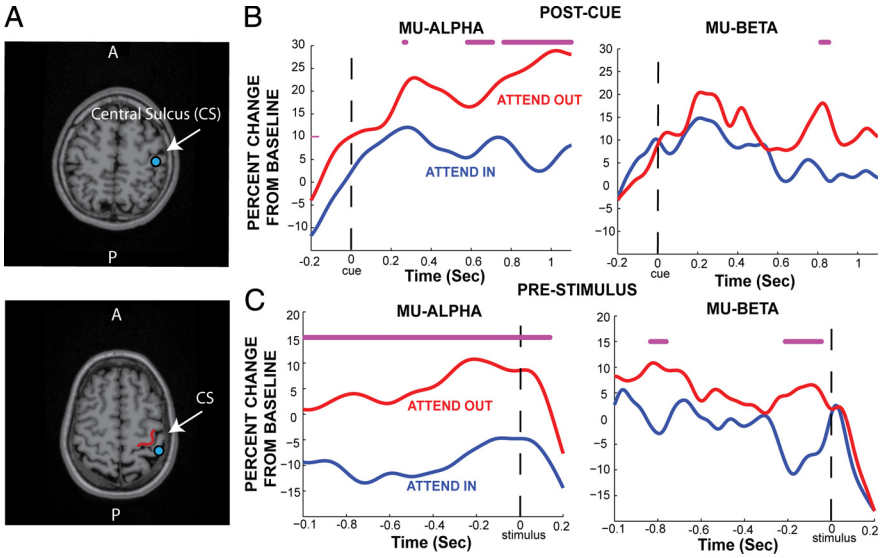

Figure 2. Impact of cued attention on SI mu-alpha and mu-beta. ***A***, Two examples of the estimated SI ECD localizations (blue dots) overlaid on the subjects' structural MRI brain images. Response evoked by a suprathreshold tactile stimulus to the left hand, third digit, was localized to the SI hand representation in area 3b, confirmed by proximity to the Ω shape (marked in red bottom panel), in the anterior bank of the contralateral postcentral gyrus. ***B***, Continuous postcue temporal evolution of the hand area SI mu-alpha (7–14 Hz) and mu-beta (15–29 Hz) activity in attend-in and attend-out conditions (avg. $n = 12$ Ss). ***C***, Corresponding continuous prestimulus evolution of mu-alpha mu-beta. Asterisks, Significant difference between conditions ($p < 0.05$).

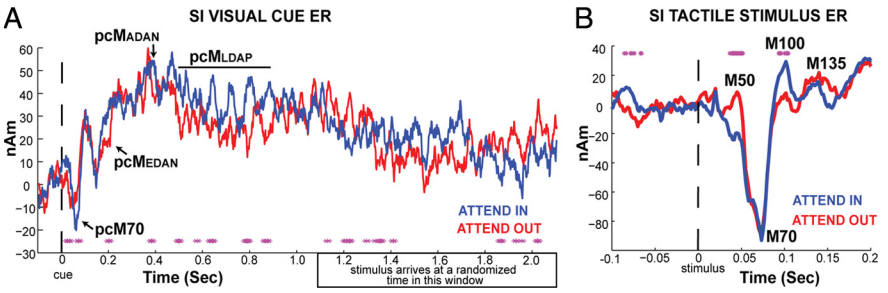

Figure 3. Impact of cued attention visual cue and tactile stimulus SI ERs. ***A***, Average hand area SI broadband ER from the visual cue in attend-in and attend-out conditions (mean $n = 12$ Ss). ***B***, Corresponding average SI broadband ER from subsequent threshold-level tactile stimulation to the hand in attend-in and attend-out conditions. Asterisks, Significant difference between conditions ($p < 0.05$).

Results

We investigated the temporal evolution of changes in mu-alpha (7–14 Hz) and mu-beta (15–29 Hz) power in a localized dipole source in the right hand area of SI after a cue to attend to tactile finger stimulation to the contralateral left hand (attend-in condition), or to tactile toe-stimulation to the left foot (attend-out condition). Figure 2*A* shows example localizations in two subjects in the SI hand representation in the anterior bank of the postcentral gyrus (area 3b), confirmed by proximity to the Ω-shaped bend (marked in red in Fig. 2*A*, bottom panel) in the central sulcus (Moore et al., 2000). Figure 2*B* shows the corresponding average percentage change from baseline [$n = 12$ subjects (Ss)] in SI mu-alpha and mu-beta power during the time period [−100, 1100] ms relative to the cue in attend-in and attend-out conditions. A significant difference across subjects was observed between the conditions in the mu-alpha band during the anticipatory postcue time period [500, 1100] ms relative to the cue ($p < 0.05$ marked with asterisks, Wilcoxon sign-rank test). Significant differences in the mu-beta band were observed for a time window of [800, 850] ms.

Aligning trials to the tactile stimulus onset ([−1000, 200] ms), rather than visual cue, also showed a dominant effect of cued attention on prestimulus mu-alpha activity (Fig. 2*C*). Significant differences between attend-in and attend-out conditions are seen in the mu-alpha across the entire prestimulus time period, and in the [−200, 0] ms time window for mu-beta, with another period of significance around −800 ms.

Next, we investigated attentional modulation of the broadband SI evoked response to the visual cue and subsequent threshold-level tactile stimulus (Fig. 3). There was a rapid response in SI to the visual cue with an initial peak near 70 ms (labeled pcM70, for "postcue M70," for reference in Fig. 3*A*) that was greater in the attend-in condition. Several other time points showed a significant difference between attend-in and attend-out conditions, and the timings of these differences was consistent with previously reported modulation of EEG measured event-related potentials (ERPs) during attention deployment in parietal, frontal, and visual cortices (Kelly et al., 2009). Most notable are the statistically significant differences at 200 ms, 400 ms, and

several intervals between 500 and 900 ms (see magenta asterisks in Fig. 3*A*). The 200 ms difference is consistent with that seen in parietal cortices and typically referred to as an "early directing attention negativity" (EDAN), labeled pcMEDAN (for "postcue MEG EDAN") in Figure 3*A*. The difference near 400 ms is consistent with the anterior directing attention negativity (ADAN) observed in frontal cortices, and the later noncontinuous differences between 500 and 900 ms are in line with those seen over occipital cortex known as late directing attention positivity (LDAP), labeled pcMADAN and pcMLDAP, respectively.

Figure 3*B* shows the SI tactile ER at [−100, 200] ms. Peaks in the waveform were consistent with previous reports using similar stimuli (Jones et al., 2007, 2009). Four peaks occurring at ~50 ms (M50), 70 ms (M70), 100 ms (M100), and 135 ms (M135), respectively, are labeled for visualization as in the Jones et al. (2007, 2009) studies. A previous study showed that high prestimulus mu-alpha and mu-beta was correlated with an increase in the magnitude of the M50 peak and a subsequent trend toward decreased M70 and later response elements (Jones et al., 2009). Here, we found that there was also a significant difference in the magnitude of the ER near the M50 peak between the attend-in and attend-out conditions, such that the magnitude of the ER was greater in the attend-out conditions, when prestimulus mu-alpha and mu-beta were higher (Fig. 3*B*, significant time points marked with asterisks, $p < 0.05$ Wilcoxon sign-rank test). There was also a significant difference in the ER near the M100 peak ($p < 0.05$ Wilcoxon sign-rank).

Although a slow cue-locked fluctuation is apparent visually in the averaged cue ER in attend-in and attend-out conditions (Fig. 3*A*), this did not bias the averaged tactile ER (Fig. 3*B*) since the tactile stimulus was jittered within the [1.1, 2.1] s postcue time window (marked in Fig. 3*A*). However, it is possible this early ER was impacted by postcue attentional modulation of the mu-alpha and mu-beta activity that is not phase locked to the cue (Fig. 2) (see Discussion).

We assessed trial-by-trial impact of prestimulus mu-alpha and mu-beta in our SI signal on tactile detection probabilities, using a second dataset that used analogous MEG and tactile detection methods, but with sustained attention to the finger (Jones et al., 2007, 2009; Ziegler et al., 2010). This previously collected dataset gave greater statistical power than the current data, where the relevant hit and miss trials represented a statistically small sample (see Materials and Methods). Following prior convention (Linkenkaer-Hansen et al., 2004), on individual trials average prestimulus mu-alpha and mu-beta power was calculated (1 s before stimulus) and sorted from high to low power into 10 equally sized percentile bins. Detection probabilities in each bin were calculated as the percentage change in hit rate from the mean (see Materials and Methods). We found a linear relationship between tactile detection probabilities and mu-alpha and mu-beta power ($p < 0.05$, F test, $R^2 = 0.65$ and $R^2 = 0.85$, respectively) such that the hit probability was greater during trials with lower prestimulus mu-alpha and mu-beta power (Fig. 4).

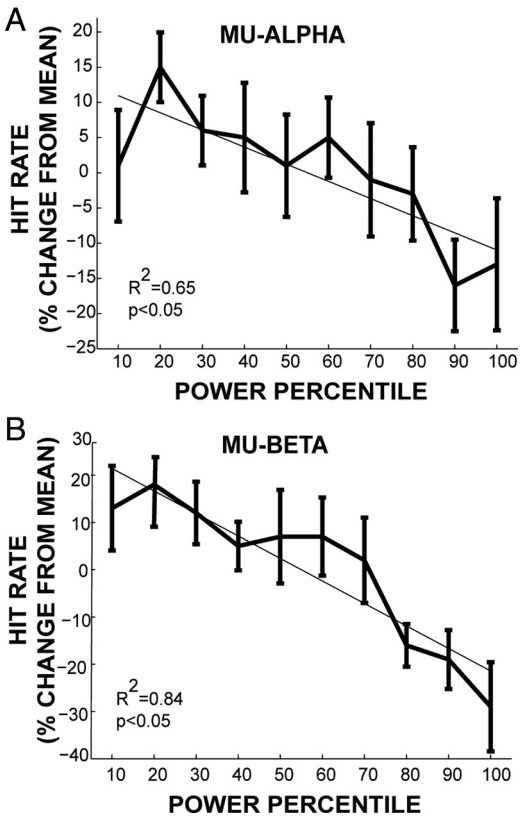

Figure 4. Impact of prestimulus mu-alpha and mu-beta power on detection probabilities. ***A***, Tactile detection probabilities, measured as percentage change in hit rate from the mean, as a function mu-alpha power sorted into 10 power percentile bins. Bold traces, Mean and SE across subjects ($n = 10$ Ss); thin traces, linear fit from linear regression analysis ($R^2 = 0.65$, $p < 0.05$). ***B***, Analogous traces as a function of mu-beta power ($R^2 = 0.84$, $p < 0.05$). This analysis was performed on data from the Jones et al. (2007, 2009) studies (see Materials and Methods).

Discussion

Consistent with findings in visual cortices, we observed that cued attention modulates anticipatory postcue mu-alpha activity and early peaks in the broadband visual cue- and tactile stimulus-induced ERs in the SI hand representation. We found a significant difference in the postcue change from baseline of mu-alpha power between attend-in and attend-out conditions. Detection probabilities were greater during lower prestimulus mu-alpha and mu-beta power. These results are consistent with the theory that attentionally induced focal alpha changes are an active mechanism for modulation of sensory information processing (Foxe et al., 1998; Worden et al., 2000; Kelly et al., 2006, 2009; Thut et al., 2006; Klimesch et al., 2007). Further, our results show that although attentional cuing has a weaker impact on SI mu-beta rhythms, they also predict tactile detection.

Attentional modulation of low-frequency rhythms and their impact on perception

Prior research connecting low-frequency oscillations and cued attention in somatosensory cortex in humans has focused on sensory-stimulus- and movement-induced ERD and subsequent ERS in alpha and beta frequencies (Bauer et al., 2006; Babiloni et al., 2008; Dockstader et al., 2010) (see also Pfurtscheller, 1992). These studies also investigated attentional modulation of somatosensory gamma (35–80 Hz) activity. Gamma was not a focus of our study because it is not robust in our spontaneous SI signal (see Jones et al., 2009).

Our finding of a linear relationship between mu-alpha and mu-beta power and tactile detection agrees with Schubert et al. (2009), who found a linear relationship between alpha and beta amplitudes in EEG electrodes over SI and tactile detection probability. These results also are consistent with the relationship between smaller alpha amplitudes and increased perception and decreased reaction times in the visual system (Thut et al., 2006; Hanslmayr et al., 2007; van Dijk et al., 2008; Kelly et al., 2009). Other studies in the somatosensory (Linkenkaer-Hansen et al.,

2004; Zhang and Ding, 2010) and visual (Rajagovindan and Ding, 2010) systems have reported an inverted-U relationship between alpha power and detection probabilities. We also found that, on trials with the lowest values of mu-alpha power, detection probability diminished compared to slightly higher values (compare 10th and 20th percentiles in Fig. 4), suggesting that a minimal baseline of alpha activity is necessary for optimal signal propagation. These results imply that the reduction of mu-alpha and mu-beta activity in SI with cued attention is an active cortical gating mechanism that increases the perceptual salience of tactile signals.

Attentional modulation of visual cue and tactile stimulus SI ERs

Studies have shown consistent effects regarding the timing and spatial specificity of distinct components of postcue EEG measured ERPs in parietal, frontal, and low-level visual areas (e.g., Kelly et al., 2009). We have shown that attentional modulation of broadband visual cue-induced ERs components exists at similar times in our high-resolution localized SI signal. In addition to changes near 200 ms (pcMEDAN), 400 ms (pcMADAN), and between 500 and 900 ms activity (pcMLDAP), we found an earlier significant difference at ~70 ms (pcM70), such that the magnitude of the peak was greater in attend-in conditions (Fig. 3*A*), suggesting rapid attentional modulation in SI.

While fitting data to a single dipole is a necessary simplification in our study, the pcM70 response difference is likely restricted to activity from SI. Rapid responses (<100 ms) to visual stimuli have been observed previously in SI. Zhou and Fuster (1997, 2000) showed a change in firing rate (predominantly increases) in single units in the anterior parietal cortex of trained monkeys, including the hand representation area in SI, during a visual cue indicating a subsequent tactile choice. In this visuohaptic memory task, a change in firing rate was observed as early as ~50–100 ms after visual cue and lasted throughout a memory retention period (~20 s). Further, some units showed differential activity depending on haptic choice indicated by the cue—vertical or horizontal bars indicating corresponding rod with oriented ridges to pull (Zhou and Fuster, 1997, 2000).

Our findings of increased magnitude near the M50 and M100 SI tactile ER peaks (Fig. 3*B*) with attention are consistent with the theory that attention increases the gain of sensory-evoked responses, and are in line with previous studies that showed increased magnitudes of evoked SI activity in MEG/EEG sensor data at similar time points (Schubert et al., 2008; Dockstader et al., 2010). However, the decreased M50 peak in the attend-in condition contrasts with previous studies showing increases near 50 ms with attention (Iguchi et al., 2002; Schubert et al., 2008; Dockstader et al., 2010). These discrepancies are likely due to differences in experimental design and the fact that the previous studies used stimuli that were perceptually salient (electrical and Braille stimuli), in contrast to our stimulus amplitude that was maintained at a 50% perceptual threshold. The ~50 ms differences in Iguchi et al. (2002) appeared during a two-finger discrimination task, but not during a nondiscrimination task. Schubert et al. (2008) used an oddball detection paradigm, and Dockstader et al. (2010) engaged attention by counting stimuli. Further, the relative magnitude of evoked activity in SI can vary as a function of context, with identical stimuli causing enhanced or suppressed responses dependent on the amplitude of sensory drive (Moore et al., 1999). In our study, greater prestimulus mu activity may similarly prime the enhancement of this early response component under conditions of weak sensory drive.

Biophysical mechanisms of SI attentional modulation: connection to previous computational modeling predictions

SI mu-alpha rhythms

We have developed a model of SI that predicts the origin of the MEG mu rhythm and tactile ERs (Jones et al., 2007, 2009). The model predicts that the mu-alpha component of the mu rhythm is created by a 10 Hz lemniscal thalamic input to granular and infragranular layers, while the mu-beta component is dependent on a second 10 Hz input to the supragranular layers. Given our model, the observed attentional decrease of mu-alpha is predicted to occur through suppression of ongoing 10 Hz lemniscal thalamus activity. This is consistent with the notion proposed by Francis Crick that the inhibitory reticular thalamus controls an attentional "searchlight" in topographic sensory representations (Crick, 1984) and recent recordings by McAlonan et al. (2008) showing that attention modulates sensory-evoked thalamic responses before reaching the neocortex (see also Suffczynski et al., 2001).

SI ERs

Our previous modeling further predicts that the decreased M50 tactile stimulus peak responses with attention may arise, at least in part, from excitatory neurons that are less depolarized during low prestimulus mu and hence have a smaller immediate poststimulus (M50) response. This decreased excitatory response leads to decreased poststimulus inhibition in the network, which enables greater subsequent M70 and M100 responses (see Jones et al., 2009). Recent research suggests that alpha rhythms may be amplified by a recruitment of a class of low-threshold spiking inhibitory neurons (Fanselow et al., 2008; Vierling-Claassen et al., 2010). These predictions provide a direct neural correlate for the theory that mu-alpha exerts inhibitory control in the neocortex (Worden et al., 2000; Klimesch et al., 2007).

Further, the negative polarity of the postcue SI pcM70 suggests it was driven by excitatory input to the supragranular layers, from higher-order neocortical or nonspecific thalamic sources (Jones et al., 2007). A subsequent peak with negative polarity emerges ~100 ms later, reflective of a two-cycle cue-locked ~10 Hz drive, which is stronger with attention. The attentional differences between 500 and 900 ms (pcMLDAP) appear to be tied to the cue-locked slow fluctuation. Slow oscillations are known to modulate higher-frequency rhythms (Schroeder and Lakatos, 2009); however, an investigation of this is beyond the scope of this study.

In summary, our results support the idea that alpha deployment may be a general mechanism of cued attention for active sensory gating. Mu-beta rhythms are impacted less by attentional cuing, but are well correlated with the probability of tactile detection. This dissociation suggests that while both oscillations impact signal processing, mu-alpha deployment may be more readily recruited during attentional allocation. Future research is needed to identify whether attentional mu-alpha modulation is somatotopically precise on finer spatial scales, as has been explored in the visual system.

References

Babiloni C, Capotosto P, Brancucci A, Del Percio C, Petrini L, Buttiglione M, Cibelli G, Romani GL, Rossini PM, Arendt-Nielsen L (2008) Cortical alpha rhythms are related to the anticipation of sensorimotor interaction between painful stimuli and movements: a high-resolution EEG study. J Pain 9:902–911.

Bauer M, Oostenveld R, Peeters M, Fries P (2006) Tactile spatial attention enhances gamma-band activity in somatosensory cortex and reduces low-frequency activity in parieto-occipital areas. J Neurosci 26:490–501.

Crick F (1984) Function of the thalamic reticular complex: the searchlight hypothesis. Proc Natl Acad Sci U S A 81:4586–4590.

Dai H (1995) On measuring psychometric functions: a comparison of the constant-stimulus and adaptive up-down methods. J Acoust Soc Am 98:3135–3139.

Del Percio C, Babiloni C, Bertollo M, Marzano N, Iacoboni M, Infarinato F, Lizio R, Stocchi M, Robazza C, Cibelli G, Comani S, Eusebi F (2009) Visuo-attentional and sensorimotor alpha rhythms are related to visuo-motor performance in athletes. Hum Brain Mapp 30:3527–3540.

Dockstader C, Cheyne D, Tannock R (2010) Cortical dynamics of selective attention to somatosensory events. Neuroimage 49:1777–1785.

Fanselow EE, Richardson KA, Connors BW (2008) Selective, state-dependent activation of somatostatin-expressing inhibitory interneurons in mouse neocortex. J Neurophysiol 100:2640–2652.

Foxe JJ, Simpson GV, Ahlfors SP (1998) Parieto-occipital approximately 10 Hz activity reflects anticipatory state of visual attention mechanisms. Neuroreport 9:3929–3933.

Fu KM, Foxe JJ, Murray MM, Higgins BA, Javitt DC, Schroeder CE (2001) Attention-dependent suppression of distracter visual input can be cross-modally cued as indexed by anticipatory parieto-occipital alpha-band oscillations. Brain Res Cogn Brain Res 12:145–152.

Hämäläinen MS, Sarvas J (1989) Realistic conductivity geometry model of the human head for interpretation of neuromagnetic data. IEEE Trans Biomed Eng 36:165–171.

Hanslmayr S, Aslan A, Staudigl T, Klimesch W, Herrmann CS, Bäuml KH (2007) Prestimulus oscillations predict visual perception performance between and within subjects. Neuroimage 37:1465–1473.

Iguchi Y, Hoshi Y, Tanosaki M, Taira M, Hashimoto I (2002) Selective attention regulates spatial and intensity information processing in the human primary somatosensory cortex. Neuroreport 13:2335–2339.

Jones SR, Pritchett DL, Stufflebeam SM, Hämäläinen M, Moore CI (2007) Neural correlates of tactile detection: a combined MEG and biophysically based computational modeling study. J Neurosci 27:10751–10764.

Jones SR, Pritchett DL, Sikora MA, Stufflebeam SM, Hämäläinen M, Moore CI (2009) Quantitative analysis and biophysically realistic neural modeling of the MEG mu rhythm: rhythmogenesis and modulation of sensory-evoked responses. J Neurophysiol 102:3554–3572.

Kelly SP, Lalor EC, Reilly RB, Foxe JJ (2006) Increases in alpha oscillatory power reflect an active retinotopic mechanism for distracter suppression during sustained visuospatial attention. J Neurophysiol 95:3844–3851.

Kelly SP, Gomez-Ramirez M, Foxe JJ (2009) The strength of anticipatory spatial biasing predicts target discrimination at attended locations: a high-density EEG study. Eur J Neurosci 30:2224–2234.

Klimesch W, Sauseng P, Hanslmayr S (2007) EEG alpha oscillations: the inhibition-timing hypothesis. Brain Res Rev 53:63–88.

Leek MR (2001) Adaptive procedures in psychophysical research. Percept Psychophys 63:1279–1292.

Linkenkaer-Hansen K, Nikulin VV, Palva S, Ilmoniemi RJ, Palva JM (2004) Prestimulus oscillations enhance psychophysical performance in humans. J Neurosci 24:10186–10190.

McAlonan K, Cavanaugh J, Wurtz RH (2008) Guarding the gateway to cortex with attention in visual thalamus. Nature 456:391–394.

Moore CI, Nelson SB, Sur M (1999) Dynamics of neuronal processing in rat somatosensory cortex. Trends Neurosci 22:513–520.

Moore CI, Stern CE, Corkin S, Fischl B, Gray AC, Rosen BR, Dale AM (2000) Segregation of somatosensory activation in the human rolandic cortex using fMRI. J Neurophysiol 84:558–569.

Pfurtscheller G (1992) Event-related synchronization (ERS): an electrophysiological correlate of cortical areas at rest. Electroencephalogr Clin Neurophysiol 83:62–69.

Rajagovindan R, Ding M (2010) From prestimulus alpha oscillation to visual-evoked response: an inverted-U function and its attentional modulation. J Cogn Neurosci. Advance online publication. Retrieved September 24, 2010. doi:10.1162/jocn.2010.21478.

Rougeul A, Bouyer JJ, Dedet L, Debray O (1979) Fast somato-parietal rhythms during combined focal attention and immobility in baboon and squirrel monkey. Electroencephalogr Clin Neurophysiol 46:310–319.

Schroeder CE, Lakatos P (2009) Low-frequency neuronal oscillations as instruments of sensory selection. Trends Neurosci 32:9–18.

Schubert R, Ritter P, Wüstenberg T, Preuschhof C, Curio G, Sommer W, Villringer A (2008) Spatial attention related SEP amplitude modulations covary with BOLD signal in S1—a simultaneous EEG–fMRI study. Cereb Cortex 18:2686–2700.

Schubert R, Haufe S, Blankenburg F, Villringer A, Curio G (2009) Now you'll feel it, now you won't: EEG rhythms predict the effectiveness of perceptual masking. J Cogn Neurosci 21:2407–2419.

Suffczynski P, Kalitzin S, Pfurtscheller G, Lopes da Silva FH (2001) Computational model of thalamo-cortical networks: dynamical control of alpha rhythms in relation to focal attention. Int J Psychophysiol 43:25–40.

Thut G, Nietzel A, Brandt SA, Pascual-Leone A (2006) Alpha-band electroencephalographic activity over occipital cortex indexes visuospatial attention bias and predicts visual target detection. J Neurosci 26:9494–9502.

Tiihonen J, Kajola M, Hari R (1989) Magnetic mu rhythm in man. Neuroscience 32:793–800.

van Dijk H, Schoffelen JM, Oostenveld R, Jensen O (2008) Prestimulus oscillatory activity in the alpha band predicts visual discrimination ability. J Neurosci 28:1816–1823.

Vierling-Claassen D, Cardin J, Moore C, Jones SR (2010) Computational modeling of distinct neocortical oscillations driven by cell-type selective optogenetic drive: separable resonant circuits controlled by low-threshold spiking and fast-spiking interneurons. Paper presented at Neuroscience 2010, Program No. 645.16, San Diego, CA, Nov. 13–17.

Worden MS, Foxe JJ, Wang N, Simpson GV (2000) Anticipatory biasing of visuospatial attention indexed by retinotopically specific alpha-band electroencephalography increases over occipital cortex. J Neurosci 20:RC63.

Zhang Y, Ding M (2010) Detection of a weak somatosensory stimulus: role of the prestimulus mu rhythm and its top-down modulation. J Cogn Neurosci 22:307–322.

Zhou YD, Fuster JM (1997) Neuronal activity of somatosensory cortex in a cross-modal (visuo-haptic) memory task. Exp Brain Res 116:551–555.

Zhou YD, Fuster JM (2000) Visuo-tactile cross-modal associations in cortical somatosensory cells. Proc Natl Acad Sci U S A 97:9777–9782.

Ziegler DA, Pritchett DL, Hosseini-Varnamkhasti P, Corkin S, Hämäläinen M, Moore CI, Jones SR (2010) Transformations in oscillatory activity and evoked responses in primary somatosensory cortex in middle age: a combined computational neural modeling and MEG study. Neuroimage 52:897–912.